Decoding beauty

Doctoral thesis

DECODING BEAUTY

Rare baryonic decays & SciFi detector commissioning

Lex Marinus Greeven

2023

Decoding beauty
Thesis, Maastricht University, Maastricht

Cover artwork by DALL-E2, Lex Greeven
Description: Radiance Within the Fiber Canvas: Envision the inner world of a scintillating fiber detector as a canvas, adorned with luminescent strokes representing particles in motion. Create an image that encapsulates the art of revealing beauty within particle physics, as highlighted in "Decoding Beauty."

Printed by Gildeprint
ISBN 978-94-6496-056-3

This work is part of the research programme of the Netherlands Organisation for Scientific Research (NWO). The work is carried out at the National Institute for Subatomic Physics (Nikhef) in Amsterdam, The Netherlands.

DECODING BEAUTY

Rare baryonic decays & SciFi detector commissioning

Dissertation

to obtain the degree of Doctor at Maastricht University,
on the authority of the Rector Magnificus, Prof. dr. Pamela Habibović
in accordance with the decision of the Board of Deans,
to be defended in public
on Wednesday 3 April 2024, at 13:00 hours.

by

Lex Marinus Greeven

Supervisor:
Prof. dr. M.H.M. Merk

Co-supervisor:
Dr. N. Tuning

Assessment Committee
Prof. dr. ir. C.J.G. Onderwater (chair)
Prof. dr. ir. P.J. de Jong, Universiteit van Amsterdam, Netherlands
Prof. dr. U. Uwer, Universität Heidelberg, Germany
Dr. K.K. Vos
Dr. J.A. de Vries

Contents

1 Introduction

Understanding nature, from the smallest particles to the largest structures in the universe, has been a long-standing goal of scientists. Over the last century, the field of particle physics has made tremendous progress in understanding the fundamental building blocks of matter and the forces that govern them. The Standard Model (SM) was developed to describe nature at the smallest observable scales and the largest collider energies, with great success [1–3]. There are, however, open questions and observations that the SM does not have an answer for. Astronomical observations have shown that the universe is made up of only 5% of the matter and energy that we can observe [4]. The remaining 95% is theorised to be made up of dark matter and dark energy, which are not described by the SM. Furthermore, the SM does not explain why the universe is made up of only matter and not antimatter, even though in laboratory environments matter and antimatter are produced in exactly equal amounts.

To find answers, physicists are testing the SM at high precision and are looking for possible new phenomena beyond the SM. The Large Hadron Collider (LHC) at CERN is the largest particle accelerator in the world and is used to collide protons at the highest energies ever achieved. Using large detector systems, production and decays of particles produced in the collisions are measured. The decays of b-hadrons, particles containing a beauty quark, are of special interest as the b-quark is one of the heaviest fundamental particles in the SM. The decays of b-hadrons can be used to measure matter-antimatter differences, but also to search for so-called "new physics". Specifically of interest are the rare decays of b-hadrons, as these processes have a small probability to occur in the SM, but could have a large relative enhancement in the presence of new physics beyond the SM.

The LHCb experiment is one of the four large experiments at the LHC and is specialised in detecting the decays of b-hadrons, providing a unique opportunity to study these rare decays.

One of the ways to search for physics "beyond the Standard Model" is by testing the so-called principle of lepton universality of the SM. Lepton flavour universality is the property of the SM where the three charged leptons (electrons, muons and taus) have identical interactions with the force mediators of the SM. This property is closely related to the conservation of lepton family, also known as lepton-flavour conservation. Finding experimental evidence for the violation of lepton universality or lepton-flavour conservation would be a clear sign of a new type of interaction. By studying rare decays of b-hadrons, new physics can be probed by testing lepton flavour universality and lepton-flavour conservation. This thesis presents analyses on the resonant control mode $\Lambda_b^0 \to J/\psi\,\Lambda$ and the rare $\Lambda_b^0 \to \Lambda\ell^+\ell^-$ mode to test lepton universality and search for lepton-flavour violation. A theoretical overview is presented in Chap. 2, followed by a description of the LHCb experiment in 3. Subsequently, the analyses and their common methods are described in Chap. 4, 5, and 6.

To keep pushing the boundaries of our knowledge of the universe, the LHC will run at higher energy and luminosity in Run 3. To be able to absorb this increase in event rate, the LHCb experiment has been upgraded during the second long shutdown of the LHC between 2019 and 2021. The main upgrades are the replacement of the entire tracking system, which is used to measure the trajectories of charged particles. In the vertex detector, the silicon strips have been replaced by silicon pixels, and in the downstream tracking stations straws have been replaced by a Scintillating Fiber (SciFi) detector. Before routine detector operation, the SciFi detector was commissioned, which is the topic of Chap. 7. There, the dataflow for the SciFi detector, timing scans of the electronics, and clustering and decoding algorithms are presented. Finally, an outlook on the future of LHCb and rare Λ_b^0 decays is given in Chap. 8.

2 Theoretical overview

Our current understanding of the fundamental constituents of matter and their interactions is described by the Standard Model (SM) of particle physics [1–3]. The SM describes two types of fundamental particles: fermions, which make up matter and bosons, which mediate the interactions between the fermions. The interplay between fermions and bosons allows the formation of more complex particles, such as mesons (consisting of a quark and anti-quark) and baryons (consisting of three quarks). Baryons with a bottom (beauty) quark and their decays are the focus of this thesis.

This chapter provides the theoretical framework for the analyses presented in this dissertation. First, the SM is introduced in Section 2.1. Then, the weak interaction is discussed in Section 2.2. Afterwards, the $b \to s\ell\ell$ transition and $\Lambda_b^0 \to \Lambda\ell^+\ell^-$ decays are described in Sections 2.3 and 2.4, respectively. Finally, the effect of new physics on the C_9 Wilson coefficient is discussed in Section 2.5.

2.1 The Standard Model

Fermions are particles with half-integer spin and are further divided into quarks and leptons, where quarks also interact via the strong interaction whereas leptons do not. The fermions are divided into three generations, each containing two quarks and two leptons, as shown in Fig. 2.1. Every generation contains a charged lepton, a neutral lepton called neutrino, an up-type quark, and a down-type quark. The generations are distinguished by the flavour quantum number. For the rest, the three generations are identical in all aspects except for their mass.

The bosons are particles with integer spin and are further divided into

gauge bosons with spin-1 and the Higgs boson with spin-0. The gauge bosons mediate the interactions between the fermions, where each boson is associated with a fundamental interaction. The photon (γ) mediates the electromagnetic interaction, the gluon (g) mediates the strong interaction, and the $W^{\pm}$ and Z bosons mediate the weak interaction. The interactions are described by the gauge group $\mathrm{SU(3)_C} \otimes \mathrm{SU(2)_L} \otimes \mathrm{U(1)_Y}$, where $\mathrm{SU(3)_C}$ is the gauge group of the strong interaction, and $\mathrm{SU(2)_L} \otimes \mathrm{U(1)_Y}$ of the electroweak interaction. This electroweak gauge symmetry is broken by the Higgs mechanism, which gives mass to the $W^{\pm}$ and Z bosons [5]. In addition, the Higgs field is responsible for the mass of the fermions through the so-called Yukawa coupling.

Even though the three fermion generations have large mass differences in the SM, the coupling of the fermions to the force mediators is the same between different flavours. This property is called lepton flavour universality (LFU) for leptons. Furthermore, the SM also does not allow couplings between leptons of different flavour, meaning that lepton flavour is conserved. This property is called lepton flavour conservation. Any deviation from this behavior would be a manifestation of physics beyond the SM. To look for signs of LFU violation or lepton flavour violation (LFV), weak decays of baryons containing a bottom quark are studied in this thesis. The weak interaction will be further described in the next section.

2.2 Weak Interaction

The weak interaction differs from the other fundamental interactions in the SM in several ways. Firstly, the weak interaction is the only interaction that violates parity (P) and charge-parity (CP) symmetry due its V–A structure: the weak interaction only couples to left-handed fermions. Secondly, it is the only force involving gauge bosons with mass, which is a consequence of the Higgs mechanism. Lastly, in the SM the weak interaction is the only interaction that can change the flavour of a quark. This process is described by the Cabbibo–Kobayashi–Maskawa (CKM) matrix [6,7], which is a unitary matrix that describes the mixing between the quark flavour eigenstates and the weak interaction eigenstates:

$$\begin{pmatrix} d' \\ s' \\ b' \end{pmatrix} = \begin{pmatrix} V_{ud} & V_{us} & V_{ub} \\ V_{cd} & V_{cs} & V_{cb} \\ V_{td} & V_{ts} & V_{tb} \end{pmatrix} \begin{pmatrix} d \\ s \\ b \end{pmatrix}. \tag{2.1}$$

V_{ij} is the matrix element describing the probability of a quark of flavour i to decay into a quark of flavour j. The CKM matrix favours decays between

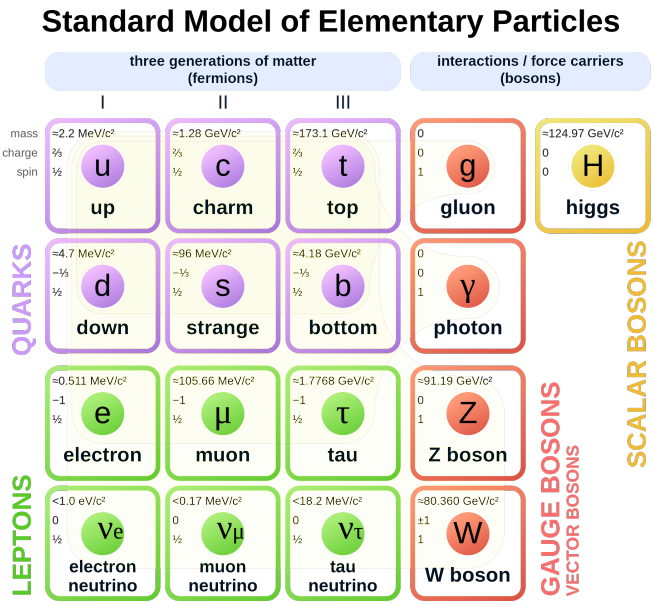

Figure 2.1: Schematic overview of the Standard Model of particle physics showing the quarks in purple, leptons in green, vector gauge bosons in red, and the scalar Higgs boson in yellow.

quarks of the same generation, and suppresses decays between quarks of different generations, a feature called Cabibbo suppression.

The weak interaction occurs in two modes: the charged current and the neutral current. The charged current, mediated by the $W^{\pm}$ boson, is responsible for the decay of a quark into a quark of a different flavour. The neutral current, mediated by the Z boson, is the scattering of a quark into a quark of the same flavour. It is, however, possible for a neutral current interaction to change the flavour of a quark without changing its charge, known as the flavour-changing neutral current (FCNC). The FCNC is forbidden at tree level in the SM, but can occur at loop level, making it suppressed. The $b \to s\ell\ell$ transitions are an example of such a FCNC process, and will be further discussed in the next section.

2.3 $b \to s\ell\ell$ transitions

The $b \to s\ell\ell$ transition is a FCNC decay where a bottom quark decays into a strange quark and a lepton–anti-lepton pair. In this thesis either electrons or muons are studied. This interaction occurs only in higher-order loop level processes, during which virtual particles are temporarily created and annihilated. The Feynman diagrams of the two main contributions to the $b \to s\ell\ell$ transition are shown in Fig. 2.2.

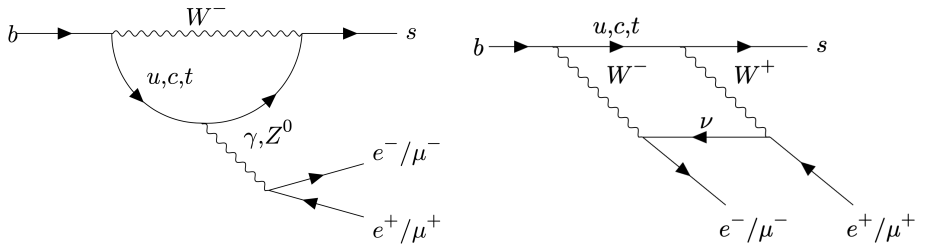

Figure 2.2: Feynman diagrams of the penguin (left) and box (right) diagrams contributing to the $b \to s\ell\ell$ transition.

Due to the higher order of the $b \to s\ell\ell$ transition, the SM prediction of branching fractions of $b \to s\ell\ell$ decays are small. This makes these decays excellent probes to test for the presence of BSM physics, as new physics contributions can here be of the same order of magnitude as the SM contributions. Especially interesting are the baryonic $b \to s\ell\ell$ decays, as they have a comparable branching fraction to their mesonic counterparts [8], but are relatively unexplored. The $\Lambda_b^0 \to \Lambda\ell^+\ell^-$ decays are an example of baryonic $b \to s\ell\ell$ decays, and will be further discussed in Section 2.4.

2.4 $\Lambda_b^0 \to \Lambda\ell^+\ell^-$ decays

The $\Lambda_b^0 \to \Lambda\ell^+\ell^-$ decays are a subset of the $b \to s\ell\ell$ transitions, where the Λ_b^0 baryon decays into a Λ baryon and a dilepton pair. An example SM Feynman diagram of the $\Lambda_b^0 \to \Lambda\ell^+\ell^-$ decay is shown on the left in Fig. 2.3, which also shows the quark content of the particles. The $\Lambda_b^0 \to \Lambda\ell^+\ell^-$ decays are interesting to study, as they are sensitive to possible new physics contributions, such as a leptoquark, as shown on the right in Fig. 2.3. Leptoquarks are hypothetical particles that couple to both leptons and quarks, and can therefore mediate the $b \to s\ell\ell$ transition at tree level [9, 10]. These leptoquarks could potentially have a higher coupling to e.g. muons

than to electrons, which would violate lepton flavour universality. They also could allow for a direct coupling between quarks and leptons, leading to a possible final state with a muon and an electron, which would violate lepton flavour conservation. Calculations have been performed on leptoquark models showing a potential branching fraction of $\mathcal{O}(10^{-9})$ for $\Lambda_b^0 \to \Lambda e^{\pm} \mu^{\mp}$ decays [11].

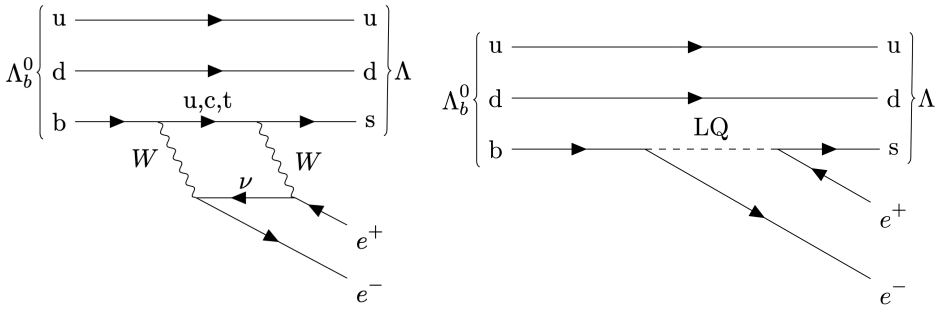

Figure 2.3: Feynman diagrams of the SM (left) and possible new physics leptoquark (right) contributions to the $\Lambda_b^0 \to \Lambda \ell^+ \ell^-$ decay.

The $\Lambda_b^0 \to \Lambda \ell^+ \ell^-$ decays can be described kinematically by the square of the dilepton mass, q^2, and the decay angles [12]:

- θ_ℓ defined as the angle between the direction of the lepton in the dilepton rest frame and the direction of the dilepton-pair in the Λ_b^0 rest frame;
- ϕ_ℓ defined as the azimuthal angle of the lepton in the dilepton rest frame;
- θ_b defined as the angle between the direction of the proton in the Λ rest frame and the direction of the Λ in the Λ_b^0 rest frame;
- ϕ_b defined as the azimuthal angle of the proton in the Λ rest frame;
- $\Delta\phi$ defined as the angle between the decay planes of the dilepton system and the Λ;
- θ polarisation angle, defined as the angle between the normal vector $\hat{n}$ and the Λ direction in the Λ_b^0 rest frame, where $\hat{n} = \frac{\vec{p^{\text{lab}}_{\text{beam}}} \times \vec{p^{\text{lab}}_{\Lambda_b^0}}}{|\vec{p^{\text{lab}}_{\text{beam}}} \times \vec{p^{\text{lab}}_{\Lambda_b^0}}|}$

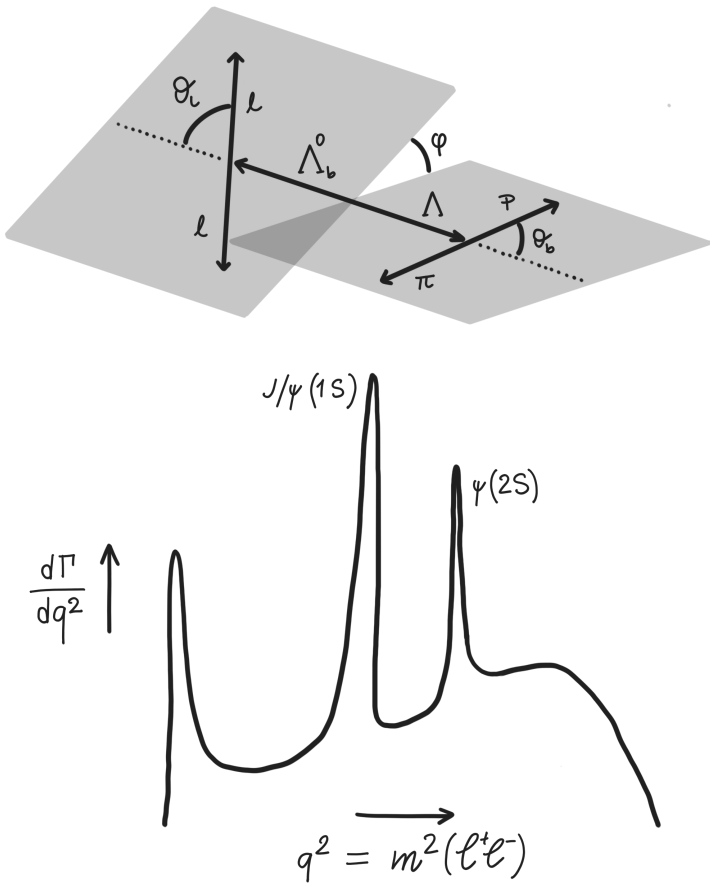

Figure 2.4: Top: schematic diagram of the decay angles in the $\Lambda_b^0 \to \Lambda \ell^+ \ell^-$ decays. Bottom: sketch of the theoretical q^2 distribution [13].

The decay angles and q^2 distribution are visualised in Fig. 2.4. The q^2 spectrum, qualitatively plotted, shows different regions associated with contributions from various decays with the same final state. The non-peaking spectrum originates from the non-resonant $b \to s\ell\ell$ transition $\Lambda_b^0 \to \Lambda \ell^+ \ell^-$ decays and represents the rare mode. Three peaks are visible as well, the resonant modes: the first peak at q^2 close to zero originates from the photon pole, where the dilepton pair is produced from a virtual photon. The two other peaks are coming from the resonant $\Lambda_b^0 \to J/\psi \Lambda$ and $\Lambda_b^0 \to \psi(2S)\Lambda$ decays, where the leptons originate from either the J/ψ or $\psi(2S)$ decay.

These resonant decays are experimentally useful as they are used to validate the analysis procedure, as will be described in Chap. 4. In contrast to mesonic $b \to s\ell\ell$ decays, the $\Lambda_b^0 \to \Lambda\ell^+\ell^-$ decays have a larger decay rate in the high q^2 region compared to the low q^2 region, allowing the search for new physics in a different, unexplored kinematic region. This is caused by the different form factors, the non-perturbative QCD effects that describe the transition between the initial and final state hadrons, of the $\Lambda_b^0 \to \Lambda\ell^+\ell^-$ decays and by the difference in spin structure.

2.5 Towards measuring C_9 and C_{10}

A common way to compute decay amplitudes for $b \to s\ell\ell$ decays is through the effective Hamiltonian formalism, where the heavy degrees of freedom (the W, Z and top quark) are integrated out [14]. The decay is then effectively described by a four-point interaction with a set of so-called Wilson operators $\mathcal{O}_i^{(\prime)}$ and Wilson coefficients $C_i^{(\prime)}$. The decay amplitude, corresponding to the Feynman diagram shown in Fig. 2.2, is then expressed as

$$\mathcal{A} = \langle sll|\mathcal{H}_{\text{eff}}|b\rangle, \tag{2.2}$$

where $\mathcal{H}_{\text{eff}}$ is the effective Hamiltonian and $|b\rangle$ and $\langle sll|$ are the initial and final states, respectively. The effective Hamiltonian can be written as

$$\mathcal{A} = \frac{G_F\alpha}{\sqrt{2}\pi} V_{ts}^* V_{tb} \sum_{i=7,9,10,S,P} C_i^{(\prime)} \mathcal{O}_i^{(\prime)}, \tag{2.3}$$

where G_F is the Fermi constant, α is the fine-structure constant, V_{ts} and V_{tb} are the CKM matrix elements. Only the t-quark exchange is considered, as it is the dominant contribution. The $\mathcal{O}_i^{\prime}$ operators correspond to opposite chirality states as the unprimed $\mathcal{O}_i$, and are negligible in the SM. The Wilson operators contain the long-distance non-perturbative effects, while the Wilson coefficients correspond to the short-distance interactions and can be calculated using perturbation theory. The separation of long- and short distance effects is referred to as factorisation. Contributions from potential new heavy particles in BSM physics are therefore only included in the Wilson coefficients. For a more detailed discussion, see e.g. Ref. [15].

The $b \to s\ell\ell$ decays are mostly sensitive to the Wilson coefficients C_9 and C_{10}, where C_9 quantifies vector couplings and C_{10} axial couplings. These can be measured through the branching fraction ratios and the angular decay rate observables. By measuring different $b \to s\ell\ell$ decays, the Wilson coefficients can be constrained using a global fit.

The top figure in Fig. 2.5 shows the 2D global fit of the C_9 and C_{10} Wilson coefficients, with the contributions from different $b \to s\ell\ell$ decays [16]. The C_{10} Wilson coefficient is constrained by the $B_s^0 \to \mu^+\mu^-$ decay branching fraction measurement, and is in agreement with the SM prediction of 0. The different measurements of C_9, however, show a preference for a non-zero value. Different global fits of the C_9 Wilson coefficient are shown in the bottom plot in Fig. 2.5, differing in their method and their exact experimental and theoretical inputs [17]. Overall, the C_9 fit shows a 4σ pull from the SM prediction, showing a preference for the presence of new physics.

It can also be seen that most of the inputs are from mesonic $b \to s\ell\ell$ decays, showing the need for more baryonic $b \to s\ell\ell$ decays to constrain the Wilson coefficients. It is for example possible that baryonic decays are affected differently by possible BSM physics than mesonic decays. Theoretical calculations for baryonic decays are, however, more complicated than their mesonic counterparts. This is caused by the different form factors, and the different spin structure of the baryons, leading to a potential polarisation in the decays. Experimental input from baryonic decay measurements therefore provides a valuable contribution to the global fits. To measure these baryonic $b \to s\ell\ell$ decays, the LHCb detector is used, which will be the topic of the next chapter.

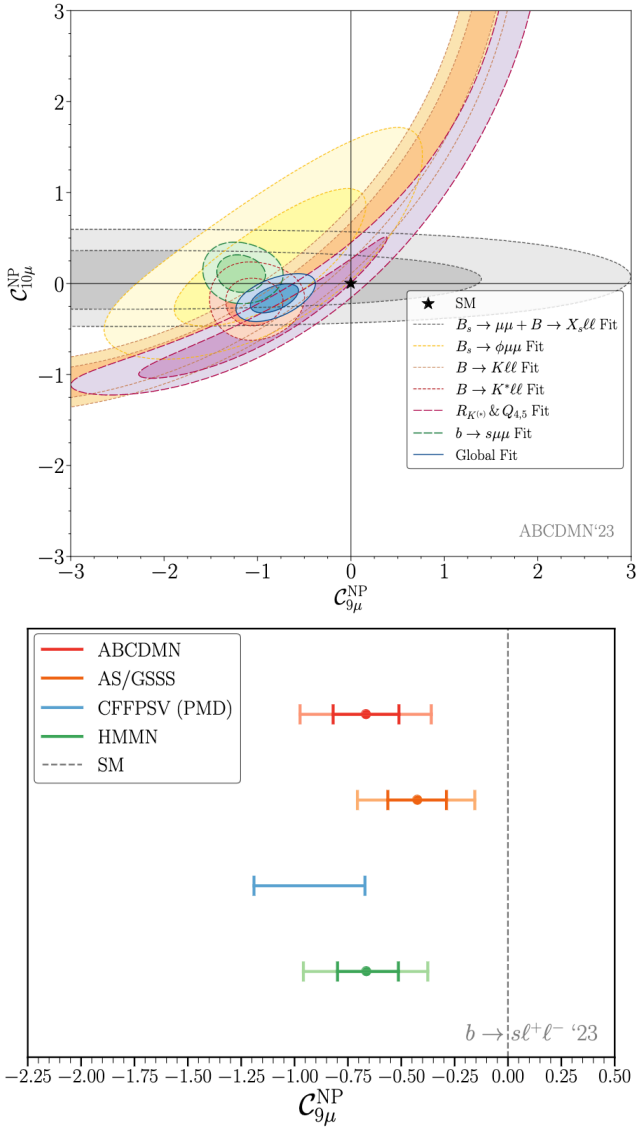

Figure 2.5: Top: 2D global fit of the C_9 and C_{10} Wilson coefficients showing the contributions from different $b \to s\ell\ell$ decays [16]. Bottom: different global fits of the C_9 Wilson coefficient.

3 The LHCb experiment

The analyses described in this thesis use data collected by the Large Hadron Collider beauty (LHCb) experiment at CERN. The LHCb experiment is located at interaction point 8 of the Large Hadron Collider (LHC). The LHC accelerates and collides proton beams (pp collisions) to a maximum of 7.5 TeV. This chapter describes the LHC and the LHCb experiment, the different LHCb subdetectors, the used trigger system, and the use of event simulation within the experiment.

3.1 The Large Hadron Collider

The LHC is currently the world's largest particle accelerator, located at the Franco-Swiss border close to Geneva. It is a circular accelerator with a circumference of 27 km and a designed maximum beam energy of 7 TeV [18]. A schematic drawing of the LHC and the CERN Accelerator Complex is shown in Fig. 3.1. Two proton beams are accelerated in opposite directions and collided at a centre-of-mass energy of 7 TeV in 2011, 8 TeV in 2012, which together form the Run 1 data-taking period of the LHC during which the LHCb experiment recorded a total of $3\,\text{fb}^{-1}$ of data. During Run2, consisting of data-taking between 2015 and 2018, the LHC operated at a centre-of-mass energy of 13 TeV, of which the LHCb experiment recorded $6\,\text{fb}^{-1}$ of data.

The protons that enter the LHC are created by stripping electrons from hydrogen gas, and sending these protons through multiple pre-accelerators. The Linac2 linear accelerator increases the proton energy to 50 MeV, after which they are injected into the Proton Synchrotron Booster (BOOSTER), where they are accelerated up to 1.4 GeV. The protons are then passed on to the Proton Synchrotron (PS) where they reach an energy of 25 GeV, and

are subsequently accelerated to 450 GeV in the Super Proton Synchrotron (SPS) before being injected into the LHC ring.

At the four LHC interaction points, the proton bunches are collided at a rate of 40 MHz. The four interaction points are home to the main LHC experiments: ATLAS (A Toroidal LHC Apparatus), CMS (Compact Muon Solenoid), ALICE (A Large Ion Collider Experiment), and LHCb (Large Hadron Collider beauty). The LHCb experiment is of main interest in this thesis, and will be described in more detail in the following sections. The LHCb experiment underwent an upgrade between the Run 2 and Run 3 data-taking periods, the following sections will describe the detector as it was during Run 1 and Run 2. Chap. 7 provides a description of the upgraded LHCb detector used from Run 3 onwards.

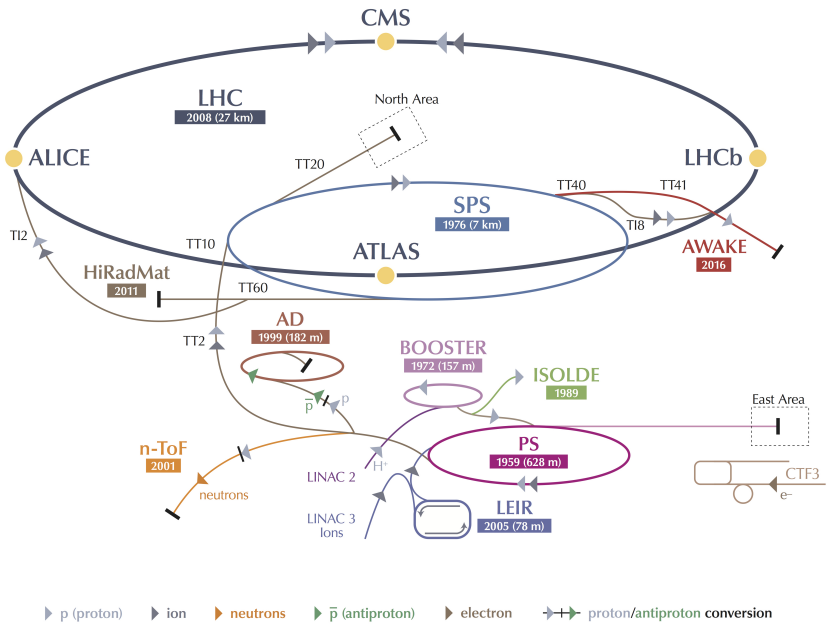

Figure 3.1: Schematic overview of the LHC and the CERN Accelerator Complex [19].

3.2 The LHCb experiment

The LHCb detector is a general-purpose detector in the forward region [20]. The experiment was designed to primarily study the decays of b hadrons for the asymmetry between matter and antimatter. In addition, over its

operating period a broad physics programme extending beyond b-physics has developed in the collaboration. This includes a heavy ion collisions study, W and Z production physics, a study of semileptonic b-decays, searches for new exotic particles consisting of 5 or 4 quarks, whereas b-physics remained the central topic. This thesis presents the study of rare beauty-hadron decays, which is the topic of the R_Λ analysis described in Chap. 6 using the Run 1 and Run 2 data. The decay product of these events are detected with a spectrometer that covers covers the pseudorapidity region of $2 < \eta < 5$, with the pseudorapidity defined as

$$\eta \equiv -\ln \tan(\theta/2) \tag{3.1}$$

where θ is the polar angle relative to the beampipe-direction (the z axis). This relatively limited η range is chosen since the heavy b and $\overline{b}$ hadrons are primarily produced in the forward direction. A schematic drawing of the experiment during the Run 1 and Run 2 data-taking periods is shown in Fig. 3.2.

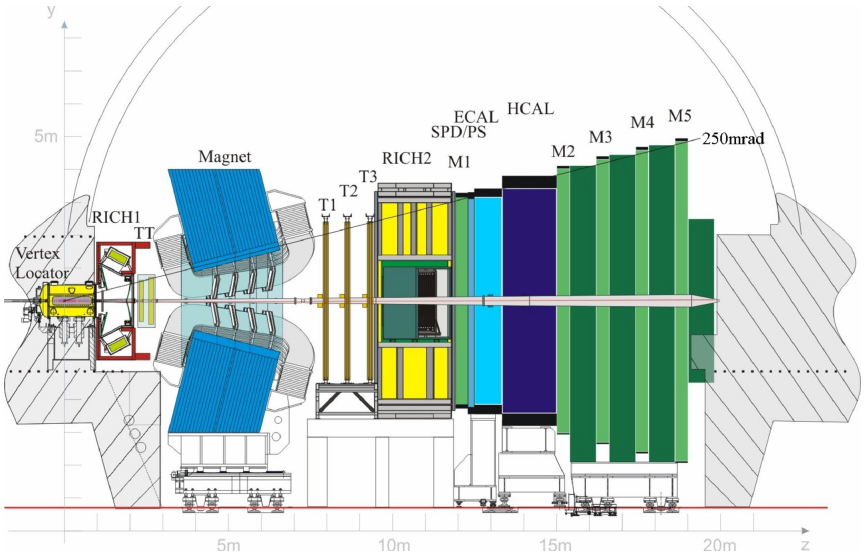

Figure 3.2: Schematic sideview of the LHCb detector and its subdetectors [20]. The coordinate system used in the LHCb experiment is also shown, with the z-axis following the beampipe direction, and the x and y-axes describing the transverse plane.

The LHCb detector consist of different subdetector systems that are needed to reconstruct- and measure the properties of the particles produced

in the proton-proton collisions. The tracking of charged particles and the reconstructing of particle decay vertices is described in Sec. 3.3. The identification of charged particles and the measurement of their energy is described in Sec. 3.4. The trigger system that is used to reduce the amount of data that is recorded from the pp collisions is described in Sec. 3.5. Finally, the simulation used to model detector efficiencies of the LHCb detector is described in Sec. 3.6.

3.3 Particle tracking

To track charged particles, the LHCb detector uses multiple subdetectors, which each fulfill their role in the particle reconstruction process. The Vertex Locator (VELO) silicon strip detector installed around the interaction point is used to track charged particles and reconstruct b-hadron production and decay vertices. A dipole magnet with an integrated field strength of 4 Tm is used to bend the charged-particle trajectories, which in combination with the Tracker Turicensis (TT), the Inner Tracker (IT), and the Outer Tracker (OT) is used to measure particle momenta. The tracking stations behind the magnet are often abbreviated with the term T-stations. The different subdetectors will be described in the following subsections.

Depending on which subdetectors were used to reconstruct particle tracks, a different track type is assigned to the particle. Fig. 3.3 shows the different types used by the LHCb experiment:

- VELO tracks, which are only reconstructed using hits in the VELO and are included in the primary vertex reconstruction.
- Upstream tracks, which have hits in the VELO and the TT station.
- Long tracks, which have hits in the VELO, T stations and also potentially the TT detector.
- Downstream tracks, which only have hits in the TT and T stations.
- T tracks, which are reconstructed using exclusively hits in the T stations.

Long tracks are the most commonly used track types for physics analyses within LHCb, as they traverse the whole spectrometer and therefore have the most optimally measured track quantities. However, the analyses described in this thesis use both the long and downstream tracks, since using downstream tracks significantly increases the amount of reconstructed candidates for long-lived particles such as the Λ baryon.

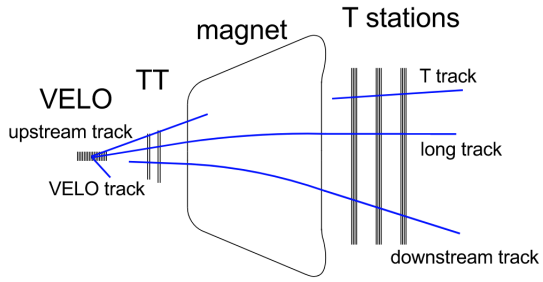

Figure 3.3: Schematic drawing of the different track types used in the LHCb detector, showing the definition of the tracks and the subsystem where the tracks have hits [21].

3.3.1 Vertex Locator

The VELO [22] is used to track charged particles close to the interaction point with a high spatial resolution, allowing for the reconstruction of b-hadron decay vertices. The VELO consists of two halves positioned at 7 mm distance left and right from the LHC beampipe. A photograph of one half of the VELO is shown in Fig. 3.4. Each half consists of 21 half-circle silicon sensor modules displaced along the z direction with a total length of approximately 1 meter. The VELO consists of two different module types, "R" and "Φ", for measuring the polar coordinates r (radial distance) and ϕ (azimuthal angle) respectively. A schematic drawing of the two different VELO types is shown in Fig. 3.4. A unique feature of the VELO is that the detector halves can move, which allows the VELO to be retracted ("opened") from the beampipe while the LHC beam is being injected, preventing unwanted radiation damage from unfocused beams. When the beam is stable, the VELO can be moved towards the beam again ("closed"). In this closed position, the VELO reconstructs primary vertices (PVs) with a resolution of 71 µm along the z-axis and 13 µm in the transverse plane [22]. The high vertex-resolution of the VELO is exploited to obtain precise reconstruction of b-hadron decay vertices such as Λ_b^0 baryons as well as their separation from the primary production vertex.

3.3.2 Tracking stations

To measure the momenta of charged particles, the LHCb detector uses a dipole magnetic field combined with different tracking stations upstream

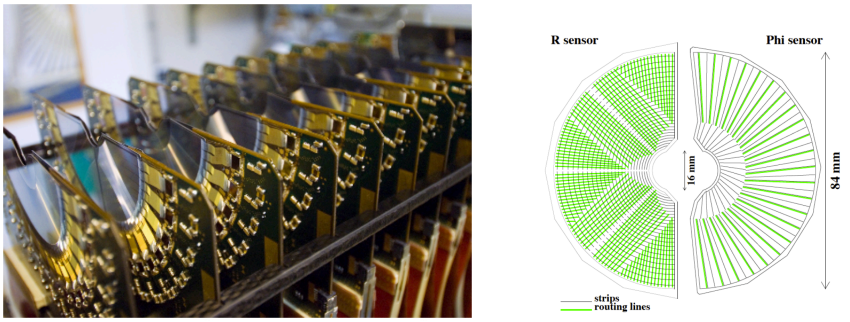

Figure 3.4: Left: photo of the VELO detector half with the sensors and readout hybrids visible [22]. Right: Schematic drawing of the two types of VELO sensors: the R and Φ sensors [23].

and downstream of the magnet. The magnetic field bends the charged-particle trajectories in the horizontal plane, allowing to measure the particle momenta. The polarity of the magnet is monthly reversed to study and understand possible detector asymmetry effects. The polarities of the magnet are referred to as magnet-up ("MU") or magnet-down ("MD").

All the T stations follow a similar design. They consist of four detection layers of tracking sensors placed in a $x - u - v - x$ stereo configuration, where the x layers are arranged to measure the horizontal x-coordinate, while the u and v layers are installed at a stereo angle with respect to the x-planes of $+5°$ and $-5°$ respectively. This allows the reconstruction of the y-coordinate of the particle trajectory, while at the same time resolve random hit combinations.

Downstream of the VELO and before the magnet, the silicon strip TT detector is located. Due to its position upstream of the magnet, the TT tracks charged particles before being bend by the magnetic field, reducing the fraction of fake combinations of VELO track segments and T-station track segments. The TT sensors have a hit resolution of approximately 50 µm. A schematic drawing of the detector with the different stereo layers is shown in Fig. 3.5. The TT is also used to detect charged particles originating from long-lived particles that decay after the VELO, such as K^0_S and Λ hadrons, which is exploited in the analyses described in this thesis. Around two thirds of Λ and K^0_S particles decay outside of the VELO, and are therefore only reconstructed as downstream tracks using their hits in the TT and the T stations.

Downstream of the magnet, the IT and OT together form three T stations. The IT detector consists of a cross-shaped layout of silicon-strip sensors,

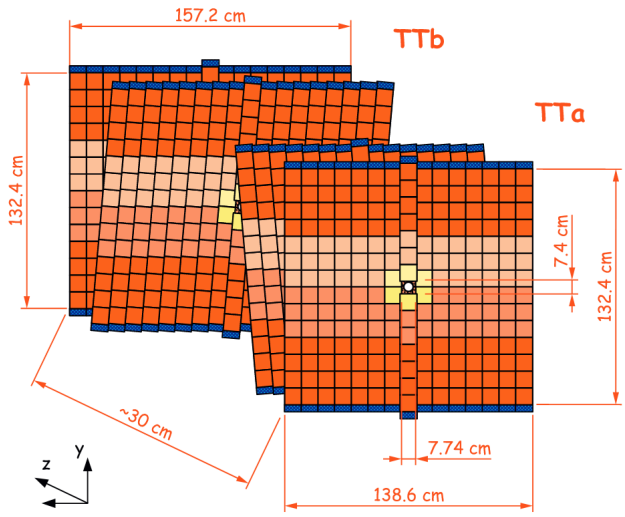

Figure 3.5: Schematic drawing of the TT layout, with the two +5° and −5° rotated layers [24].

located around the beampipe. A schematic layout of a single IT layer is shown in Fig. 3.6. In this very forward, high-density tracking region a large number of particles per surface area are observed, which is the reason that the IT exploits silicon-strip sensors instead of a gaseous drift detector such as the OT. The IT sensors have a hit resolution of around 55 µm, similar to the TT.

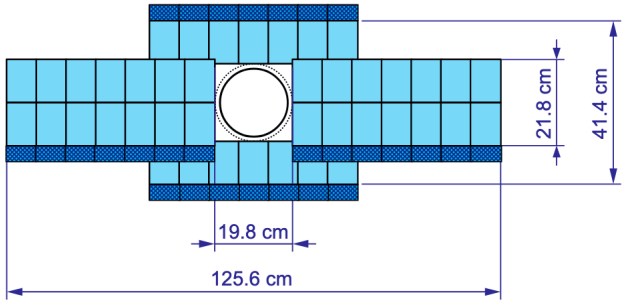

Figure 3.6: Schematic drawing of a IT subdetector layer [24]. The dark blue shows the area of the readout electronics and the cooling, while the light blue indicates the sensor modules.

The region further from the beampipe is covered by the OT. The OT is a gaseous drift detector, which consists of 5 mm straw tubes, containing a gas mixture of 70% argon, 28.5% carbon dioxide, and 1.5% oxygen. A schematic drawing of the OT is shown in Fig. 3.7. The OT covers 98% of the total TT stations, spanning a total area of 595 cm wide and 480 cm high. Charged particles traversing the straw tubes ionise the gas, leading to the creation of electron-ion pairs. Due to the electric field inside the tubes, the electrons drift towards the anode wire. The drift time is used to measure the hit position. The position hit resolution of the OT is around 200 μm.

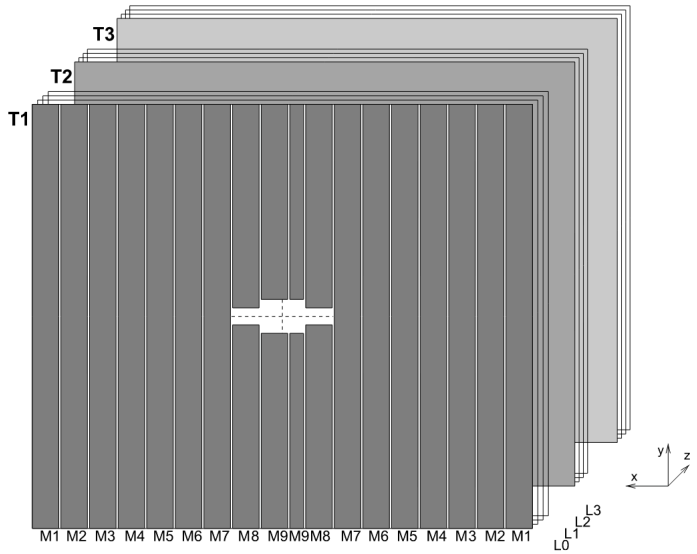

Figure 3.7: Schematic drawing of the OT layout showing the three tracking stations with four layers and 18 modules [25]. The cross-shaped cutout in the middle is the location of the IT detector.

To deal with the increase in event multiplicity for LHC Run 3, in the upgrade of the LHCb detector both the IT and OT have been replaced by the SciFi tracker. Instead of using silicon strips and gas drift tubes, the SciFi tracker uses 250 μm size scintillating fibres to measure the particle trajectories. The SciFi tracker is described in detail in Chap. 7.

Using the LHCb tracking system, the momentum of charged-particle tracks are measured with an efficiency of at least 96% and with a resolution between $0.5 - 1.0\%$ depending on their momentum, [26]. This momentum resolution allows the LHCb experiment to measure the invariant mass of particles such as the Λ and Λ_b^0 baryons with precision corresponding to

10 MeV, which is used for the signal extraction in the physics analyses.

3.4 Particle identification

Reconstruction of particle trajectories is not enough to identify the type of particle traversed the detector. To identify the type of particle, used to separate between signal and background decays, the LHCb detector uses different particle identification (PID) detectors: two Ring-Imaging Cherenkov (RICH) detectors, the electromagnetic calorimeter (ECAL), the hadronic calorimeter (HCAL), and the muon stations. The following subsections describe the main features of the different PID detectors.

3.4.1 RICH detectors

LHCb includes two RICH detectors: RICH1 located before the magnet between the VELO and the TT, and RICH2 located after the magnet and T stations [27]. The detectors exploit the Cherenkov light emitted by a particle traveling faster than the speed of light in the surrounding medium. The radiator mediums used in RICH1 is C_4F_{10} gas for relatively low momentum particles, while RICH2 uses C_2F_4 gas for high momentum particles. Cherenkov radiation is emitted in the form of a cone in angle θ, which is related to the particle's velocity v and the refractive index n of the traversed medium by the following equation:

$$\cos(\theta) = \frac{1}{n\beta}. \tag{3.2}$$

The light emitted by the particle is reflected using a set of mirrors and recorded using hybrid photon detectors. A schematic image of the RICH1 working mechanism is shown in Fig. 3.8 on the left. Combining the velocity measurement of the particle through the RICH with the measured momentum using the tracking system, the mass of the particle can be calculated. The Cherenkov angle measured in RICH1 as function of their momentum for different types of particles is shown in Fig. 3.8 on the right, where a distinction between particle types is visible by bands in the plot.

3.4.2 Calorimeters

After the tracking system and the RICH detectors, particles impinge on the calorimeter system. The calorimeter system is used to measure the energy of neutral particles such as photon and π^0, while also providing information

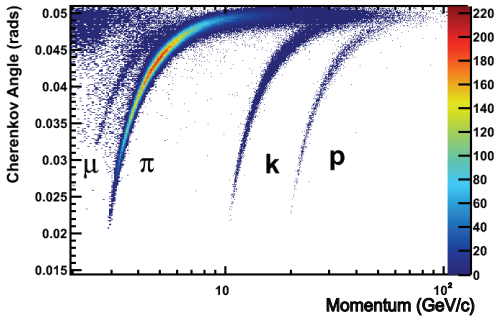

Figure 3.8: Reconstructed Cherenkov angle in RICH1 for different particle types [27].

for particle identification. In addition, the calorimeter system is used to trigger on events with high energy clusters, which will be further described in Sec. 3.5. The calorimeter consists of multiple subsystems. Particles first pass through the scintillating pad detector (SPD), where charged particles generate light but neutral particles do not due to different shower formation. The SPD signal hence gives information whether the cluster measured in the calorimeter originated from a charged particle (e.g. π^+, e^-) or neutral particle (e.g. photon, π^0). Afterwards, a layer of lead and the pre-shower (PS) detector allow for separation between electromagnetic showers of electrons and photons compared to hadrons. Following the PS, the electromangetic calorimeter (ECAL) is used to measure the energy of electromagnetically-interacting particles. The ECAL is made of cells containing alternating layers of scintillating plates and lead, with a total radiation length of $25X_0$, sufficient to contain the electromagnetic shower. The energy deposited by the traversing particles is recorded and read out, and clusters of cells can be formed to reconstruct the energy of the particle. The ECAL is also used in the reconstruction of bremsstrahlung photons, which are photons emitted by electrons while interacting with the detector. If undetected, they will result in a wrong energy measurement of the electron.

The hadronic calorimeter (HCAL) is used to measure the energy of hadrons, and similar to the ECAL, is made of iron and scintillating plates, but has a less granular setup, with a radiation length $5.6\lambda_{\text{int}}$. A schematic drawing of the response of the calorimeter system for different particle types is shown in Fig. 3.9.

For analysis purposes, the information from the different calorimeter systems is combined in terms of likelihood ratios between different particle types or more high-level variables such as neural network responses.

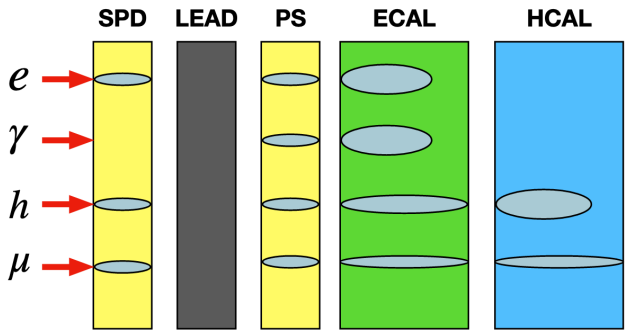

Figure 3.9: Schematic drawing of the calorimeter response for different particle types [28]. e stands for electrons, γ for photons, h for hadrons, and μ for muons. A thin ellipse indicates a small energy deposited, while a thick ellipse indicates the particle loses all of its energy in the system.

3.4.3 Muon stations

The muon stations are located furthest downstream from the interaction point. The first muon station M1 is located between RICH2 and the calorimeters, while M2-M5 are located after the calorimeters. Apart from the rare punch-through hadrons, muons are the only particles that pass through the calorimeter material, allowing to identify that particles that reach the muon stations are actually muons. Hits in the muon station are also used to trigger on events of interest, as will be described in the next section. The muon stations consists of alternating layers of detection planes and iron absorbers, to further reduce the number of hadrons that potentially pass through the HCAL. The muon stations contain two detector types. The outer part consists of multi-wire proportional chambers, while the inner part of M1 has gas electron-multiplier detectors close to the beampipe to operate within the higher particle density. If a track has hits in the muon stations, it is assigned the `isMuon` flag, indicating that the particle was likely a muon. The information of the muon stations is also used for high-level PID variables, similar to the calorimeters.

3.5 Trigger

The LHC collides protons at a rate of around 30 MHz, of which only a fraction is of interest. A rate of 30 MHz would also be unmanageable in terms of offline data storage. Therefore, the event rate is reduced using the

LHCb Trigger system [29,30]. The trigger system reduces the event rate to 5 kHz in Run 1 and 12.5 kHz in Run 2. It consists of two levels: the Level 0 (L0) is a hardware-based trigger, while the second High Level Trigger (HLT) is a software-based trigger. The following subsections provide an overview of the L0 and HLT trigger systems in general as well as the triggers used in the $\mathcal{B}(\Lambda_b^0 \to J/\psi\,\Lambda)$, $\Lambda_b^0 \to \Lambda e^\pm \mu^\mp$, and the R_Λ analyses.

3.5.1 L0 hardware trigger

The L0 hardware trigger is used to reduce the initial LHC collision rate to around 1 MHz. This is done using the calorimeter trigger and the muon trigger. For the R_Λ analysis, the `L0Electron` calorimeter trigger is used to trigger on electrons from $\Lambda_b^0 \to \Lambda e^+ e^-$ and $\Lambda_b^0 \to J/\psi\,(\to e^+e^-)\Lambda$ decays. This trigger finds particles that have a high transverse energy (E_T), by looking at 2x2 cells in the ECAL and finding the cell with the highest E_T. The E_T threshold varies per data-taking year, but is around 2.5 GeV to 3.0 GeV in Run 1 and 1.8 GeV to 2.7 GeV in Run 2. `L0Electron` also requires a minimum of one hit in the SPD and one or two PS hits in order to reject clusters from photons.

For the $\mathcal{B}(\Lambda_b^0 \to J/\psi\,\Lambda)$, $\Lambda_b^0 \to \Lambda e^\pm \mu^\mp$, and R_Λ analyses, the `L0Muon` trigger is used to trigger on the muon from the $\Lambda_b^0 \to \Lambda \mu^+ \mu^-$ and $\Lambda_b^0 \to J/\psi\,(\to \mu^+\mu^-)\Lambda$ decays, and potential $\Lambda_b^0 \to \Lambda e^\pm \mu^\mp$ candidates. The $\mathcal{B}(\Lambda_b^0 \to J/\psi\,\Lambda)$ analysis also triggers on a muon pair using `L0DiMuon`. The two highest transverse momentum (p_T) tracks in each quarter of M1 and M2 are used in the dimuon trigger. For `L0Muon`, the single highest p_T track of the eight selected tracks is used and checked to satisfy the threshold requirements, between 1.5 GeV and 1.8 GeV in Run 1 and 1.4 GeV to 2.9 GeV in Run 2. `L0DiMuon` requires the multiplication of the two highest p_T tracks to be larger than 1.7 GeV^2 to 2.6 GeV^2 in Run 1 and 1.3 GeV^2 to 1.5 GeV^2 in Run 2.

The exact requirements of the L0 trigger selection differ between- and during data taking years. To store the exact requirements, Trigger Configuration Keys (TCKs) are used. For the analyses described in this thesis, the requirements are always set to the highest values that were used in the data-taking period. This process is referred to as TCK alignment. Appendix A shows tables for the `L0Electron`, `L0Muon` and `L0DiMuon` triggers for the different data-taking years. The events passing the requirements of the L0 trigger are passed on to the HLT triggers.

3.5.2 HLT1 and HLT2 software trigger

The HLT1 is the first software-based trigger applied after the L0 trigger, and reduces the event rate to around 40 kHz in Run 1 and 100 kHz in Run 2. It performs a partial event reconstruction, such that charged tracks are reconstructed and the primary vertices are calculated. Basic selections can be made on the tracks. More specifically the HLT1 selects good quality tracks with high (transverse) momentum, as these often originate from b-hadron decays. The $\mathcal{B}(\Lambda_b^0 \to J/\psi\,\Lambda)$, $\Lambda_b^0 \to \Lambda e^{\pm}\mu^{\mp}$, and R_Λ analyses use the following HLT1 lines, where similarly to the L0 trigger the exact requirements are always set to the highest value that were used in the data-taking period.

- Hlt1TrackAllL0: used in Run 1 only. A one-track trigger line that selects displaced tracks from all L0 triggers with requirements on minimum p and p_T.
- Hlt1TrackMVA: used in Run 2 only. A similar trigger line to Hlt1TrackAllL0, but using a 2D selection on p_T and IP significance.

The $\mathcal{B}(\Lambda_b^0 \to J/\psi\,\Lambda)$ and $\Lambda_b^0 \to \Lambda e^{\pm}\mu^{\mp}$ analysis also uses the following, more muon-specific HLT1 lines:

- HLT1TrackMuon: a similar trigger line to Hlt1TrackAllL0, but only looking at `L0Muon` events. It has looser (transverse) momentum requirements.
- Hlt1TrackMuonMVA: a similar trigger line to Hlt1TrackMVA, but used from 2016 onwards.
- Hlt1DiMuonHighMass ($\mathcal{B}(\Lambda_b^0 \to J/\psi\,\Lambda)$ only): a line that selects di-muon candidates with a good vertex and requires a minimum p, p_T, and invariant mass of the muons.

Events passing a HLT1 trigger line are subsequently processed in the HLT2 trigger. This further reduces the rate to 5 kHz in Run 1 and 12.5 kHz in Run 2. The HLT2 trigger implements a full event reconstruction using track fits and vertexing algorithms. In Run 1, this was a simplified version of the offline reconstruction, while in Run 2 the HLT2 reconstruction matches the reconstruction done offline. The analyses in this thesis use the so-called topological HLT2 lines, which are used to select b-hadron candidates compatible with a 2- or 3-body decay. They perform selections on the vertex quality, muon or electron PID, and require separation from the IP. This information is then combined using multi-variate analysis techniques into

a trigger decision. Furthermore a global event cut on the number of hits in the SPD detector is used to reject events with very high occupancy, to mitigate computing resources. In Run 1 this corresponds to the selection `nSPDHits` < 600, while in Run 2 this is `nSPDHits` < 450. The events passing the HLT2 lines are then stored to disk to be further processed during the offline analysis.

3.6 Simulation

Simulation, also often referred to as Monte Carlo (MC), plays an important role in analyses at the LHCb experiment. It is used to obtain reconstruction and selections efficiencies for particle decays, to describe possible background sources, and to find invariant mass parametrizations for signal and background decays. The pp-collisions are simulated using the Pythia software [31,32] using LHCb-specific settings [33]. The generated signal b-hadron is then forced to decay under study through the specified decay using the EvtGen software [34], where the Photos [35] software is used to generate radiative effects. Finally, the generated particles are propagated through the detector using the Geant4 package [36–38], which describes the interaction of particles with the detector and simulates the detector response. After this, the trigger and reconstruction algorithms are performed in the same way as on LHCb data, and the resulting simulated events can be used for offline analysis.

The complete LHCb detector system as described in this chapter can be used to measure decays of Λ_b^0 baryons. The following chapter gives an overview of the $\Lambda_b^0 \to \Lambda \ell^+ \ell^-$ analyses, namely the resonant $\mathcal{B}(\Lambda_b^0 \to J/\psi\, \Lambda)$ measurement, test of lepton flavour universality R_Λ analysis, and the search for the forbidden $\Lambda_b^0 \to \Lambda e^\pm \mu^\mp$ decay.

4 $\Lambda_b^0 \to \Lambda \ell^+ \ell^-$ analyses overview

Different analyses of rare electroweak penguin decays of b-mesons give rise to the so-called flavour anomalies (see Chap. 2). More specifically, the $b \to s\ell\ell$ transition has been of particular interest in the past years, due to its large suppression in the SM, and the resulting sensitivity to signal possible new physics contributions. The LHCb experiment has measured branching fractions of multiple $b \to s\ell\ell$ decays [39, 40], angular distributions [41, 42], and lepton flavour universality ratios [43–45]. The results of some of these measurements are in some tension with the SM predictions, and could hint towards potential beyond the SM physics.

The baryonic decays of b-hadrons through $b \to s\ell\ell$ transitions are, however, largely unexplored, and therefore provide a new avenue to search for new physics. The LHCb experiment has studied decays of b-baryons to test lepton flavour universality [46] with the $\Lambda_b^0 \to pK^-\mu^+\mu^-$ decay, where the proton and the kaon do not originate from a resonant particle. This has the benefit of giving a higher signal yield, but comes with the disadvantage of uncertain theory predictions. LHCb has also measured the $\Lambda_b^0 \to \Lambda\mu^+\mu^-$ decay rate [47]. The measurement was, however, performed using only the Run 1 dataset leading to relatively large statistical uncertainties. Next to this, the $\Lambda_b^0 \to J/\psi\,\Lambda$ decays used as the normalisation channel come with a large uncertainty on its branching fraction, leading to a large uncertainty on the $\Lambda_b^0 \to \Lambda\mu^+\mu^-$ branching fraction itself. This thesis explores the rare $\Lambda_b^0 \to \Lambda\ell^+\ell^-$ decays for Run 1 and Run 2, where the leptons are either electrons or muons, furthering the exploration of the flavour anomalies in the baryonic sector.

This chapter gives an overview of the three related analyses:

- The resonant mode with a measurement of $\mathcal{B}(\Lambda_b^0 \to J/\psi\,\Lambda)$. The

branching fraction of $\Lambda_b^0 \to J/\psi \Lambda$ has not yet been measured by LHCb and is poorly known to date [48]. An accurate value of the branching fraction is crucial to improve the precision on the rare mode branching fraction measurements. The analysis is described in Chap. 5.

- The rare mode with a measurement of the ratio $R_\Lambda = \mathcal{B}(\Lambda_b^0 \to \Lambda \mu^+ \mu^-)/\mathcal{B}(\Lambda_b^0 \to \Lambda e^+ e^-)$. This is the first analysis testing lepton flavour universality (LFU) using baryonic decays with a resonant hadronic final state particle, which can be compared to a preciese theoretical predictions. The R_Λ analysis is the topic of Chap. 6.

- The forbidden mode with the search for the decay $\Lambda_b^0 \to \Lambda e^\pm \mu^\mp$. Any observation of this decay would be a clear sign of new physics, as lepton flavour violation (LFV) is forbidden in the SM. This analysis aims to set a limit on the branching fraction of this decay. The forbidden mode analysis follows the same methods as described in this chapter, but is not the main focus of this thesis. It will therefore be discussed in less detail than the other two analyses. For a full in-depth description and results of this analysis, the reader is referred to Ref. [49].

This chapter also describes the common methods used between the three analyses. The resonant mode and the rare mode are only distinguished by the invariant mass of the lepton pair, q^2. The measured q^2 distribution for the $\Lambda_b^0 \to \Lambda \mu^+ \mu^-$ decay is shown in Fig. 4.1, where the resonant J/ψ and $\psi(2S)$ regions around 10 and 14 GeV^2 are omitted. The decay rate is largest in the high q^2 region, and therefore the R_Λ analysis is dominated by this region.

The branching fraction of the resonant $\Lambda_b^0 \to J/\psi (\to \mu^+ \mu^-) \Lambda$ mode is poorly known and has last been updated over 10 years ago by the D0 collaboration, with a large uncertainty [48]. This uncertainty can be significantly improved by measuring this branching fraction at LHCb. Furthermore, a good experimental understanding of the reconstruction of the resonant decays is important for the rare mode and the forbidden mode analyses. The resonant decays are used as the normalisation channel in the R_Λ and $\Lambda_b^0 \to \Lambda e^\pm \mu^\mp$ analyses. The J/ψ resonance is used as a normalisation mode in the R_Λ analysis, allowing for the cancellation of multiple systematic uncertainties originating from detector effects. In addition, the study of the resonance mode allows to understand the absolute muon and electron selection efficiencies by performing crosschecks on the ratio of the electron and muon modes.

Due to significant overlap between the three analyses, analysis methods

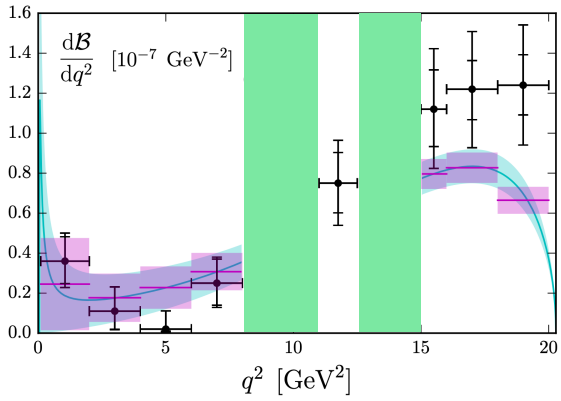

Figure 4.1: The measured lepton pair invariant mass, q^2, distribution for $\Lambda_b^0 \to \Lambda\mu^+\mu^-$ decays with Run 1 data only [47]. The inner error bars represent the statistical and systematic uncertainty, whereas the the outer error bar includes the uncertainty of the normalisation which will be improved with better knowledge of $\mathcal{B}(\Lambda_b^0 \to J/\psi\,\Lambda)$. The different colour bands show the binned (pink) and integrated (blue) theoretical predictions [8], while the green vertical bands indicate the excluded resonant regions.

are shared between them. This chapter provides a description of the analysis strategy, the decay topology and relevant detector effects, and an overview of the common steps involved in the analyses.

4.1 Analysis strategy

The analyses are split into different categories to account of different detector effects in the subsamples. An overview of the different analyses and their categories is shown in Tab. 4.1. Firstly, the analyses are split in data-taking periods. For the R_Λ and $\Lambda_b^0 \to \Lambda e^\pm\mu^\mp$ analyses the data from Run 1, 2015-2016, and 2017-2018 is analysed separately, while for the $\mathcal{B}(\Lambda_b^0 \to J/\psi\,\Lambda)$ analysis the data from 2016-2018 is combined. Secondly, the analyses are split in the track type of the reconstructed Λ decay products, either two long tracks (LL) or two downstream tracks (DD) depending on the decay distance of the Λ. For the $\mathcal{B}(\Lambda_b^0 \to J/\psi\,\Lambda)$ analysis, separate analyses done with downstream and long tracks provide an independent validation of the results. Finally, some parts of the R_Λ analysis use a separation between electrons reconstructed with one or two, or without bremsstrahlung photons. The R_Λ and $\Lambda_b^0 \to \Lambda e^\pm\mu^\mp$ analyses are performed blind, meaning that the

signal mass region is masked until the analysis is ready to be finalised. The following subsections describe the analysis strategy for both analyses.

Table 4.1: Overview table showing the different analyses and their categories. "$\mathcal{B}$" indicates branching fraction, "LFU" is lepton flavour universality, and "LFV" is lepton flavour violation.

Mode	Analysis	Decay	Period	Track	Brem.
Resonant	$\mathcal{B}$	$\Lambda_b^0 \to J/\psi \Lambda$	(16+17+18)	(DD),(LL)	-
Rare	LFU	$\Lambda_b^0 \to \Lambda \ell^+ \ell^-$	(Run 1),(15+16),(17+18)	(DD),(LL)	(0),(1),(2)
Forbidden	LFV	$\Lambda_b^0 \to \Lambda e^\pm \mu^\mp$	(Run 1),(Run 2)	(DD),(LL)	(0),(1)

4.1.1 Datasets

The upgraded LHCb detector installed in 2019-2021 described in the previous chapter has not yet recorded sufficient data to study rare beauty decays. Therefore the analyses make use of the LHCb data recorded during 2011-2012 (Run 1), 2015-2016 (Run 2p1), and 2017-2018 (Run 2p2) with the centre-of-mass energy and luminosity as described in Sec. 3.1, resulting in a total integrated luminosity of $9\,\text{fb}^{-1}$. As the $\mathcal{B}(\Lambda_b^0 \to J/\psi \Lambda)$ analysis is not statistically limited, only the data collected between 2016 and 2018 is used, which is a uniform dataset containing 80% of the total recorded sample of Λ_b^0 decays.

4.1.2 Resonant mode: $\mathcal{B}(\Lambda_b^0 \to J/\psi \Lambda)$ analysis strategy

The branching fraction of the $\Lambda_b^0 \to J/\psi \Lambda$ decay is determined using Λ candidates reconstructed using two downstream or long tracks. The signal branching fraction is normalised using the $B^0 \to J/\psi (\to \mu^+\mu^-) K_S^0$ decay, where the K_S^0 is reconstructed in its decay to the $\pi^+\pi^-$ final state, since its branching fraction is well measured by the B-factories and the decay topology is similar to the Λ_b^0 counterpart. The ratio of observed yields is determined in bins of the transverse momentum and given by

$$\frac{N_{J/\psi \Lambda}(p_\text{T})}{N_{J/\psi K_S^0}(p_\text{T})} = \frac{f_{\Lambda_b^0}}{f_d}(p_\text{T}) \times \frac{\mathcal{B}(\Lambda_b^0 \to J/\psi \Lambda)}{\mathcal{B}(B^0 \to J/\psi K_S^0)} \times \frac{\mathcal{B}(\Lambda \to p\pi^-)}{\mathcal{B}(K_S^0 \to \pi^+\pi^-)} \times \frac{\varepsilon_{J/\psi \Lambda}(p_\text{T})}{\varepsilon_{J/\psi K_S^0}(p_\text{T})}\,, \tag{4.1}$$

where N are the obtained event yields, $f_{\Lambda_b^0}/f_d$ is the ratio of production fractions of Λ_b^0 baryons relative to B^0 mesons, and $\varepsilon_{J/\psi \Lambda}/\varepsilon_{J/\psi K_S^0}$ is the ratio of the efficiencies to reconstruct and select the two decays.

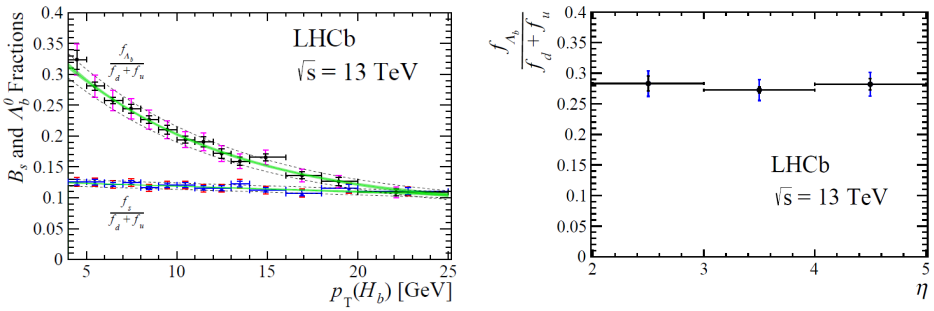

Figure 4.2: Dependence of the production fraction $f_{\Lambda_b^0}/(f_u + f_d)$ on the b-hadron p_T (left) and η (right) [50]. The η dependence is not used here, but given for completeness. The left figure also shows the $f_s/(f_d + f_u)$ production fraction of B_s^0 mesons relative to B^0 and B^+ mesons.

The ratio $f_{\Lambda_b^0}/(f_u + f_d)$ describes the production ratio of Λ_b^0 baryons compared to B^0 and B^+ mesons, and has previously been measured at LHCb with semileptonic decays at $\sqrt{s} = 13\,\text{TeV}$ [50]. As the $f_{\Lambda_b^0}/(f_u + f_d)$ fraction has been measured only within the LHCb acceptance, all the efficiencies for the analysis are calculated relative to generated simulation events within the same acceptance. The measurement of $f_{\Lambda_b^0}/(f_u + f_d)$ shows a strong dependence on the b-hadron p_T, and is shown in Figure 4.2. Assuming isospin symmetry and taking into account the observed p_T dependence, the production fraction ratio $f_{\Lambda_b^0}/f_d$ at $\sqrt{s} = 13\,\text{TeV}$ is parameterised by

$$\frac{f_{\Lambda_b^0}}{f_d} = 2\frac{f_{\Lambda_b^0}}{f_u + f_d}(p_T) = 2 \times A[p_1 + \exp(p_2 + p_3 p_T)] \tag{4.2}$$

with $A = 1.000 \pm 0.061$, $p_1 = (7.93 \pm 1.41) \times 10^{-2}$, $p_2 = -1.022 \pm 0.047$ and $p_3 = -0.107 \pm 0.002\,\text{GeV}^{-1}$.

To account for the p_T dependence of $f_{\Lambda_b^0}/f_d$, the event yields are determined in bins of b–hadron p_T. The following p_T binning from the $f_{\Lambda_b^0}/f_d$ measurement is used: $(4-5,\ 5-6,\ 7-8,\ 8-9,\ 9-10,\ 10-11,\ 11-12,\ 12-13,\ 13-14,\ 14-15,\ 15-16,\ 16-18,\ 18-20)\,\text{GeV}/c$. The branching fraction is then determined by fitting the scale of the ratio of yields $N_{J/\psi\Lambda}/N_{J/\psi K_S^0}$ as a function of p_T, while keeping the p_T dependence fixed withing Gaussian constraints.

4.1.3 Rare mode: R_Λ analysis strategy

The R_Λ analysis measures the ratio of $\Lambda_b^0 \to \Lambda e^+ e^-$ and $\Lambda_b^0 \to \Lambda \mu^+ \mu^-$ branching fractions multiplied by the ratio of the measured branching fractions of the corresponding $\Lambda_b^0 \to J/\psi\, \Lambda$ decays, defined as

$$R_\Lambda = \frac{\mathcal{B}(\Lambda_b^0 \to \Lambda \mu^+ \mu^-)}{\mathcal{B}(\Lambda_b^0 \to \Lambda e^+ e^-)} \times \frac{\mathcal{B}(\Lambda_b^0 \to \Lambda J/\psi(\to e^+ e^-))}{\mathcal{B}(\Lambda_b^0 \to \Lambda J/\psi(\to \mu^+ \mu^-))} \tag{4.3}$$

The detector-related systematic uncertainties on the muon and electron selection efficiencies cancel by using the double ratio. The single ratio of measured $\Lambda_b^0 \to J/\psi(\to e^+ e^-)\Lambda$ and $\Lambda_b^0 \to J/\psi(\to \mu^+ \mu^-)\Lambda$ branching fractions is used to study the absolute muon and electron selection efficiency and has been precisely measured to be consistent with 1 [51]. Any deviation from 1 in the R_Λ ratio thus indicates lepton flavour non-universality in the rare $\Lambda_b^0 \to \Lambda \ell^+ \ell^-$ decays. Experimentally, the R_Λ ratio is measured through the ratio of obtained event yields (N) and the reconstruction efficiencies (ε) as shown below.

$$\begin{aligned} R_\Lambda = & \frac{N_{\Lambda_b^0 \to \Lambda \mu^+ \mu^-}}{N_{\Lambda_b^0 \to \Lambda e^+ e^-}} \times \frac{\varepsilon_{\Lambda_b^0 \to \Lambda e^+ e^-}}{\varepsilon_{\Lambda_b^0 \to \Lambda \mu^+ \mu^-}} \times \\ & \frac{N_{\Lambda_b^0 \to J/\psi(\to e^+ e^-)\Lambda}}{N_{\Lambda_b^0 \to J/\psi(\to \mu^+ \mu^-)\Lambda}} \times \frac{\varepsilon_{\Lambda_b^0 \to J/\psi(\to \mu^+ \mu^-)\Lambda}}{\varepsilon_{\Lambda_b^0 \to J/\psi(\to e^+ e^-)\Lambda}} \end{aligned} \tag{4.4}$$

To ensure that the reconstruction efficiencies are well understood, multiple crosschecks are performed. The single ratio $r_{J/\psi}$,

$$r_{J/\psi} = \frac{N_{\Lambda_b^0 \to J/\psi(\to \mu^+ \mu^-)\Lambda}}{N_{\Lambda_b^0 \to J/\psi(\to e^+ e^-)\Lambda}} \times \frac{\varepsilon_{\Lambda_b^0 \to J/\psi(\to e^+ e^-)\Lambda}}{\varepsilon_{\Lambda_b^0 \to J/\psi(\to \mu^+ \mu^-)\Lambda}}, \tag{4.5}$$

is studied in detail as a function of numerous variables to guarantee that the absolute selection efficiencies for muons and electrons are understood in the full phase space, despite the different kinematic properties of $\Lambda_b^0 \to \Lambda \ell^+ \ell^-$ and $\Lambda_b^0 \to J/\psi\, \Lambda$ decays. The ratio is both measured as a single value, and in bins of different variables to check for possible kinematic dependence. Similarly, as a further crosscheck, the single ratio using the $\psi(2S)$ resonance, $r_{\psi(2S)}$, is measured as

$$r_{\psi(2S)} = \frac{N_{\Lambda_b^0 \to \psi(2S)(\to \mu^+ \mu^-)\Lambda}}{N_{\Lambda_b^0 \to \psi(2S)(\to e^+ e^-)\Lambda}} \times \frac{\varepsilon_{\Lambda_b^0 \to \psi(2S)(\to e^+ e^-)\Lambda}}{\varepsilon_{\Lambda_b^0 \to \psi(2S)(\to \mu^+ \mu^-)\Lambda}}, \tag{4.6}$$

and compared to unity.

A second crosscheck is performed using a double ratio similar to R_Λ with the $\psi(2S)$ resonance, $R_{\psi(2S)}$, to validate the analysis methods in a different lepton invariant-mass region.

$$R_{\psi(2S)} = \frac{N_{\Lambda_b^0\to\psi(2S)(\to\mu^+\mu^-)\Lambda}}{N_{\Lambda_b^0\to\psi(2S)(\to e^+e^-)\Lambda}} \times \frac{\varepsilon_{\Lambda_b^0\to\psi(2S)(\to e^+e^-)\Lambda}}{\varepsilon_{\Lambda_b^0\to\psi(2S)(\to\mu^+\mu^-)\Lambda}} \times \frac{N_{\Lambda_b^0\to J/\psi(\to e^+e^-)\Lambda}}{N_{\Lambda_b^0\to J/\psi(\to\mu^+\mu^-)\Lambda}} \times \frac{\varepsilon_{\Lambda_b^0\to J/\psi(\to\mu^+\mu^-)\Lambda}}{\varepsilon_{\Lambda_b^0\to J/\psi(\to e^+e^-)\Lambda}} \tag{4.7}$$

Note that the branching fractions of the $\psi(2S)$ resonance decaying into two electrons or two muons have been measured to be consistent with eachother [51], and that the double ratio $R_{\psi(2S)}$ is thus expected to be 1. The low branching fraction and reconstruction efficiency of $\Lambda_b^0 \to \psi(2S)(\to e^+e^-)\Lambda$ decays leads to a small dataset, and therefore the ratio is measured as an integrated value and not in bins of kinematic variables. A measurement of $R_{\psi(2S)}$ consistent with unity is a prerequisite for obtaining an unbiased estimate of R_Λ.

4.1.4 Forbidden mode: $\Lambda_b^0 \to \Lambda e^\pm \mu^\mp$ analysis strategy

The decay $\Lambda_b^0 \to \Lambda e^\pm \mu^\mp$ is a lepton-flavour violating decay, and thus no events are expected in the SM. The analysis aims to either find these novel type of decays or set a limit on the branching fraction of the $\Lambda_b^0 \to \Lambda e^\pm \mu^\mp$ decay using the CLs method [52]. To obtain an absolute limit, the result is normalised to the decay $\Lambda_b^0 \to J/\psi(\to \mu^+\mu^-)\Lambda$, using a preliminary measurement of the $\Lambda_b^0 \to J/\psi(\to \mu^+\mu^-)\Lambda$ branching fraction from the analysis described in Sec. 4.1.2. This procedure allows for the cancellation of detector systematics given that the event selections are aligned. The analysis is a search for a decay that is only present in beyond the SM (BSM) models, and therefore an important aspect of the analysis is the estimation of possible SM backgrounds after event selection [53–55]. As mentioned, the analysis results and further analysis details are described in Ref. [49] and will not be discussed in detail in this thesis. The analysis currently sets an expected limit using pseudoexperiments of $\mathcal{B}(\Lambda_b^0 \to \Lambda e^\pm \mu^\mp) < 2.09 \cdot 10^{-7}$ at 95% confidence level, as shown in Fig 4.3.

4.2 Decay topology and detector effects

All three analyses have the same experimental signature, namely two oppositely-charged leptons, and two charged hadrons coming from the decay

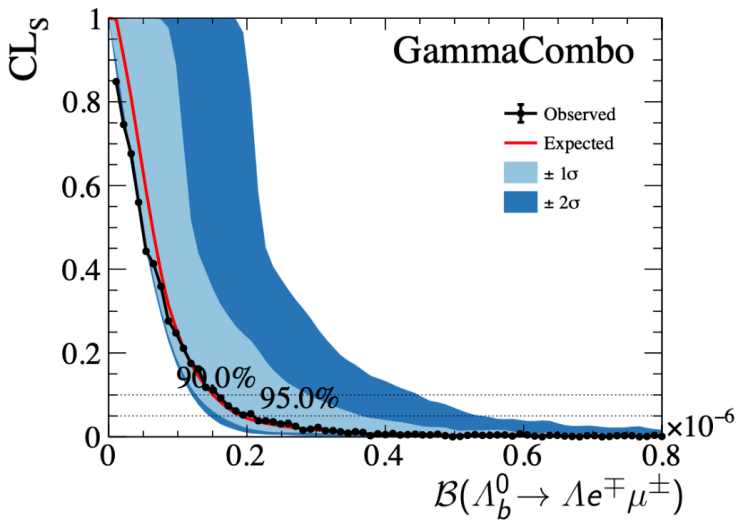

Figure 4.3: The 90% and 95% confidence level upper limits on the branching fraction of the $\Lambda_b^0 \to \Lambda e^{\pm}\mu^{\mp}$ decay obtained through the CLs method using 2000 pseudoexperiments [49]. A 95% confidence level limit of $2.09 \cdot 10^{-7}$ is obtained.

of the long-living Λ or K_S^0 hadron, in the final state. For the rare $\Lambda_b^0 \to \Lambda \ell^+ \ell^-$ decays, the J/ψ resonance is not present and the leptons originate directly from the Λ_b^0 decay. A schematic drawing of the $\Lambda_b^0 \to J/\psi \Lambda$ decay topology is shown in Fig. 4.4.

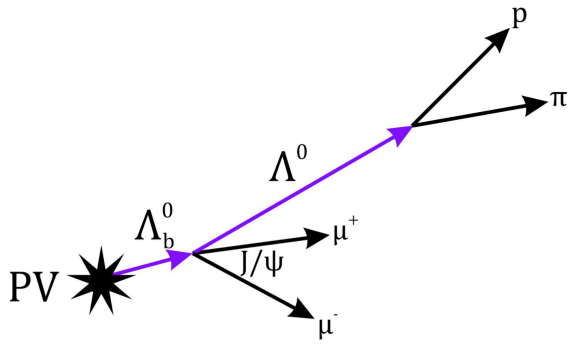

Figure 4.4: Schematic drawing of the decay topology of the $\Lambda_b^0 \to J/\psi \Lambda$ decay. As the J/ψ lifetime is very short, no displaced vertex of the lepton pair is detected. Therefore, the $\Lambda_b^0 \to \Lambda \ell^+ \ell^-$ rare decay where the leptons come directly from the Λ_b^0 has the same topology as the J/ψ resonant mode.

The b-hadron Λ_b^0 (B^0) travels on average 10 mm before it decays into a J/ψ meson (or directly into two leptons for the rare decays) and a Λ (K_S^0) hadron. Lifetime and decay-vertex z position distributions for Λ and K_S^0 hadrons are shown in Fig. 4.5 and Fig. 4.6, respectively. As mentioned in Sec. 3.3.2, due to the long lifetime of the Λ baryon (2.6×10^{-10}s) most of the Λ baryons decay downstream of the VELO. The shorter lifetime of the K_S^0 meson (0.9×10^{-10}s) can clearly be seen by comparing the lifetime distributions of the downstream Λ and K_S^0 candidates. For the hadrons reconstructed with downstream tracks, candidates with a decay-vertex z positions larger than 2250 mm are rejected as they are hadrons that interact with the detector material at the interface of the RICH1. Due to the requirement of three VELO hits for the long tracks, the decay-vertex position is limited by roughly 500 mm, corresponding to the length of the VELO. After 500 mm, the Λ (K_S^0) candidates are reconstructed as downstream candidates, as is visible in the distributions. Adding the long track and downstream track distributions together, the full exponential decay time distribution of the long-lived hadrons becomes visible.

For the R_Λ and $\Lambda_b^0 \to \Lambda e^\pm \mu^\mp$ analyses, electrons have to be reconstructed. As mentioned in Sec. 3.4.2, electrons can interact with the detector material, leading to the emission of bremsstrahlung photons. To correctly measure the energy of the electron, the bremsstrahlung photons have to be reconstructed and their energy added to the electron energy measurement. This process is illustrated in Fig. 4.7. Muons on the other hand traverse the full detector as a minimum ionizing particle, losing little energy along the way. The reconstruction efficiency for muons is therefore higher than for the electrons. The $\Lambda_b^0 \to \Lambda e^+ e^-$ reconstruction efficiency and resolution will be the limiting factor in its precision, due to the lower efficiency leading to fewer events after event selection, and the lower resolution giving a wider invariant mass peak with more possible background sources. As the energy spectrum of electrons without recovered bremsstrahlung photons differs from the spectrum with recovered photons, the categories are treated separately in the analysis. For the $\Lambda_b^0 \to \Lambda e^\pm \mu^\mp$ analysis, the samples are split in events with bremsstrahlung recovery (1γ) and without (0γ). The R_Λ analysis studies $\Lambda_b^0 \to \Lambda e^+ e^-$ decays and therefore also those events are considered where both electrons have bremsstrahlung recovered (2γ).

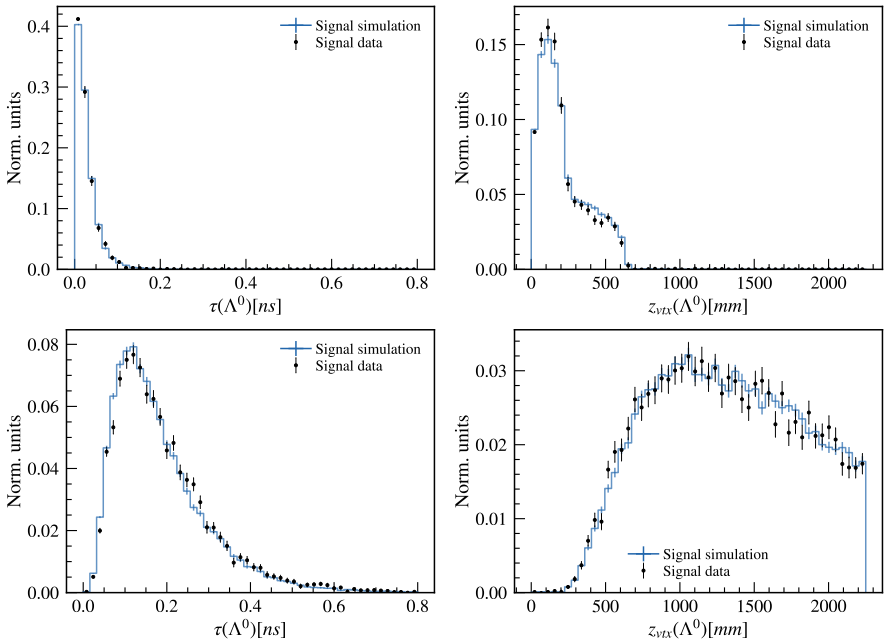

Figure 4.5: Lifetime and decay-vertex z position distributions for baryons reconstructed with long (top) or downstream (bottom) tracks. The Λ baryons originate from $\Lambda_b^0 \to J/\psi(\to \mu^+\mu^-)\Lambda$ decays in 2018 data and simulation. The Λ baryon reconstructed with long tracks decayed inside the VELO, corresponding to lower lifetimes and decay vertex positions.

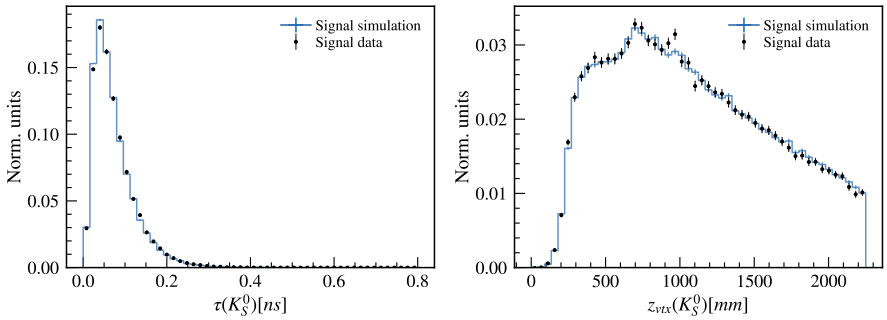

Figure 4.6: Lifetime and decay-vertex z position distributions for K_S^0 mesons reconstructed with downstream tracks, from $B^0 \to J/\psi(\to \mu^+\mu^-)K_S^0$ decays in 2018 data and simulation.

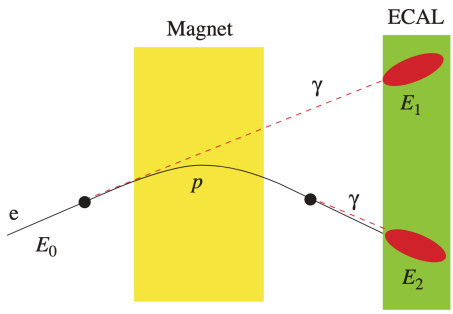

Figure 4.7: Schematic drawing of the bremsstrahlung correction for an electron [56]. The electron can radiate photons when passing through material before or after the magnet, leading to different energy deposits in the detector. To correctly reconstruct the energy of the electron, both the E_1 and E_2 clusters have to be reconstructed and added to the electron momentum measurement.

4.3 Analysis steps

The various Λ_b^0 analyses follow a similar analysis procedure. A schematic flowchart of the different steps involved in the analyses is shown in Fig. 4.8.

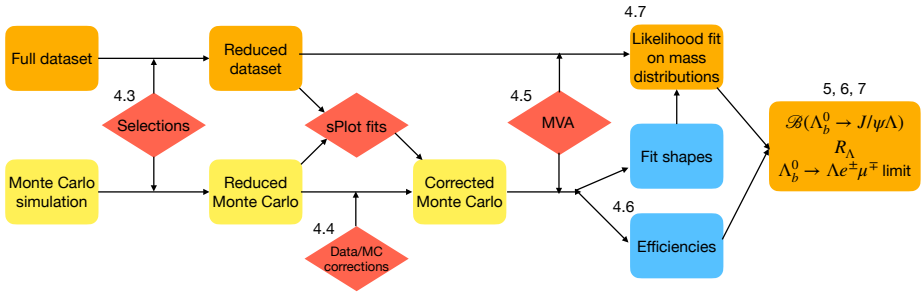

Figure 4.8: Flowchart diagram of the analysis steps and the corresponding thesis sections. Orange boxes indicate data sets, while the yellow boxes indicate MC simulation sets. The blue and red boxes indicate the steps in the analysis.

Firstly, event selections are applied to reject background events. This is shown in Fig. 4.8 as the red 'Selections' box. The selections are always applied on both the data sample, as well as on the MC simulation, to ensure that the simulation is representative of the data. The analyses require fiducial cuts on the Λ and K_S^0 candidates which aim to reduce unphysical signal candidates. Tables with the exact selection criteria applied are listed in Appendix B. The Λ/K_S^0 decay vertex and lifetime requirements are used to minimise the number of fake candidates from material interactions in the detector. Additionally, the Λ and K_S^0 candidates are required to have a small angle between a line drawn from the primary vertex to the decay vertex of the particle on the one hand, and the sum of the 4-momentum of its decay products on the other hand. The flight distance χ^2 significance with respect to the primary vertex is required to be larger than zero in order to ensure they decay downstream with respect to the b-hadron candidates.

After the selections are applied, the MC simulation has to be corrected for potential mismodelling, such that the simulation is representative of the actual data. This corresponds to the yellow 'Data/MC corrections' box in Fig. 4.8. These corrections are needed to obtain matching selection efficiencies and mass distributions. This is achieved by applying weights to the MC simulation, which are either calculated as analytical corrections or obtained from data. The different corrections are discussed in more detail in Sec. 4.4.

Once the simulation is corrected, a Multi Variate Classifier (MVA) is trained using background samples from data and signal samples from MC simulation. This is only applied to the R_Λ and $\Lambda_b^0 \to \Lambda e^\pm \mu^\mp$ analyses where further background suppression is needed to optimize the sensitivity for the small signal. The signal in the $\mathcal{B}(\Lambda_b^0 \to J/\psi\,\Lambda)$ analysis is already well separated from the background after preselections, and therefore does not need a MVA selection. The MVA is used to separate signal from combinatorial background events, and is trained to maximise the signal purity and minimise the background contamination. A selection is then applied on the MVA output, leading to a data set with fewer background events. Sec. 4.5 describes the MVA in more detail.

After the MVA selection, a maximum likelihood fit is performed on the data to extract the signal and normalization yields. The shapes of the invariant mass distribution of the signal and background samples are obtained from MC simulation.

The selection efficiencies are obtained from the MC simulation, which combined with the obtained signal and normalisation yields, allows for the calculation of the final result: either $\mathcal{B}(\Lambda_b^0 \to J/\psi\,\Lambda)$, R_Λ, or a limit on $\mathcal{B}(\Lambda_b^0 \to \Lambda e^\pm \mu^\mp)$. As the three analyses analyse similar final states, and follow a similar procedure, methods are shared between them. This also allows for cross checks between the analyses, and ensures a consistent treatment of the shared results.

4.4 Corrections to simulation

The analyses use MC simulation to obtain the mass shapes of the signal, normalisation, and background samples, train the MVA classifier, and to calculate signal selection efficiencies. To do this, good agreement between the MC and the data is required. Unfortunately the simulation does not perfectly model all detector effects that affect the track reconstruction and particle identification. In addition, the production kinematics of b-hadrons is not correctly modelled. Finally, the $\Lambda_b^0 \to J/\psi\,\Lambda$ samples are generated flat in phase-space, which is known to be incorrect since the angular decay structure, originating from the spin-1 nature of the J/ψ meson, has been measured by LHCb [57].

To improve the agreement between the data and simulated MC, several corrections are applied to the simulated signal and normalisation samples. The weights are derived iteratively, *i.e.* the correction consisting of the N^{th} weight is weighted on top of the product of previous $N-1$ weights.

Weights are determined (and applied) as a function of the following variables:

- Λ_b^0 lifetime
- $\Lambda_b^0 \to J/\psi\,\Lambda$ angular distribution
- Lepton PID efficiency
- Tracking efficiency (for long tracks)
- Trigger efficiency
- Λ_b^0 production kinematics

4.4.1 Λ_b^0 lifetime

Weights are applied to correct the Λ_b^0 lifetime distribution, using the updated lifetime value of 1.470 ps from the PDG [51], compared to the outdated 1.451 ps used in the generation of the MC samples. The weights are calculated analytically as:

$$w(t) = \frac{\tau_{\text{gen}}}{\tau_{wa}} \cdot \exp\left[t \cdot \frac{\tau_{\text{wa}} - \tau_{\text{gen}}}{\tau_{wa}\tau_{gen}}\right], \tag{4.8}$$

where τ_{wa} and τ_{gen} are the world average mean lifetime and the generated one, respectively. Fig. 4.9 shows the distribution of the decay time of the Λ_b^0, $t(\Lambda_b^0)$, on signal data and on simulation before and after the application

of the weights. For completeness, also the effect of the other corrections are shown. Since the simulated lifetime was already close to the PDG value, the weights have a negligible effect on the lifetime distribution.

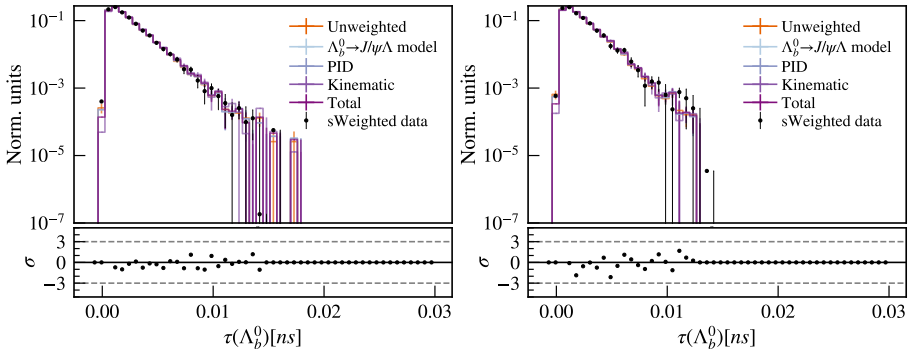

Figure 4.9: Distribution of the lifetime of $\Lambda_b^0 \to J/\psi\,(\to \mu^+\mu^-)\Lambda$ decays for signal data (black points) and simulation before (orange lines) and after (dark purple lines) the re-weighting. The left plot describes samples with the Λ baryon reconstructed with downstream tracks, while the right one describes the samples with long tracks, both using 2018 data.

4.4.2 $\Lambda_b^0 \to J/\psi\,(\to \mu^+\mu^-)\Lambda$ angular distribution

The angular distributions of the $\Lambda_b^0 \to J/\psi\,(\to \mu^+\mu^-)\Lambda$ decay are weighted to match the measurements in Ref. [57], where the 20 angular moments parameterising the decay were measured. No such correction is applied for the non-resonant $\Lambda_b^0 \to \Lambda\ell^+\ell^-$ mode, as the simulation already has the measured angular distribution implemented. The reweighted helicity angles are shown in Fig. 4.10.

4.4.3 Lepton PID efficiency

The efficiency of the particle identification (PID) selection on the leptons is calibrated in bins of the lepton p and p_T using a data-driven method [58], where the PID efficiency is calculated using different calibrated data samples. This is compared to the PID efficiency in simulation, and corrected where needed. For the muon PID calibration, the data sample consists of reconstructed detached $J/\psi \to \mu^+\mu^-$ candidates originating from b-hadron decays. To prevent tracks misidentified as muons to be used in the calibration, a strict muon PID selection is applied to one of the two muons coming from the

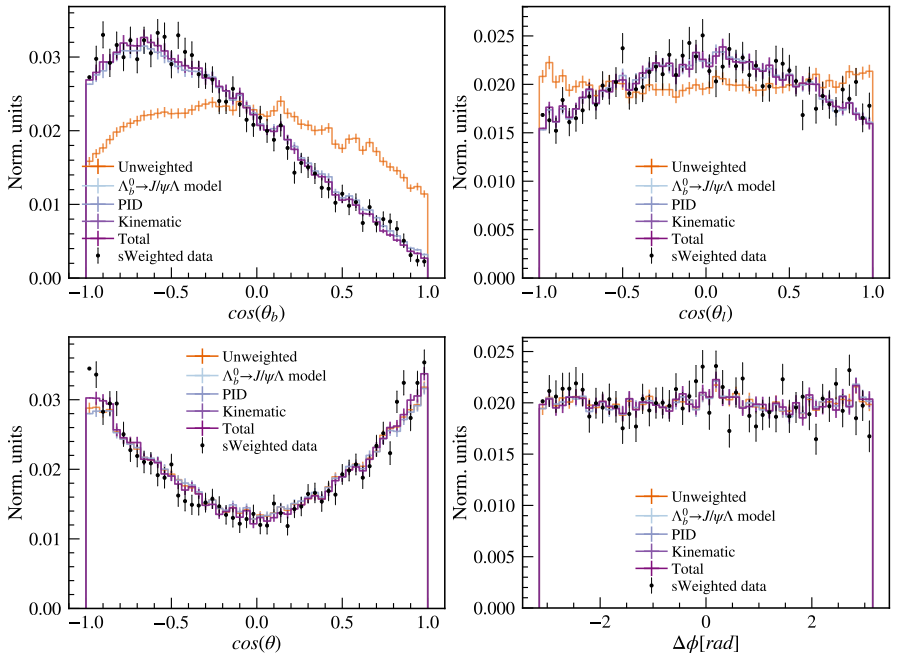

Figure 4.10: Distributions of the four helicity angles of the $\Lambda_b^0 \to J/\psi\,(\to \mu^+\mu^-)\Lambda$ decay, showing 2018 data and reweighted simulated samples. From top left to bottom right: $\cos\theta_b$, $\cos\theta_l$, $\cos\theta$, and $\Delta\phi$.

J/ψ decay. One of the two tracks passes the strict PID selection, while the other track without any PID selection is used to calibrate the PID efficiency. Two-dimensional look-up tables are used to obtain a per-candidate weight for the simulated events, replacing the PID selection. The resulting efficiency maps for the used muon PID selection are illustrated in Fig. 4.11 for the 2018 sample.

The electron PID efficiencies are obtained using the so-called 'Fit and Count' method. $B^+ \to J/\psi\,(\to e^+e^-)K^+$ data samples are used with an identical track selection as for this analysis. The sample is then split in bins of p and p_T, following the binning as described in Ref. [59]. The relevant PID selections are applied, and the sample is split in 'pass' and 'fail', depending on whether the events pass the PID selection. Fits are performed on the pass and fail samples, taking into account a possible background coming from mis-identified pions as kaons. The obtained fit yields can then be used

to calculate the efficiency of the PID selection as described in Equation 4.9.

$$\varepsilon^{e}_{PID} = \frac{N_{\text{Pass}}}{N_{\text{Pass}} + N_{\text{Fail}}} \tag{4.9}$$

Two example fits of the pass and fail samples are shown in Fig. 4.13, and the obtained PID efficiency maps for 2018 data are shown in Fig. 4.12.

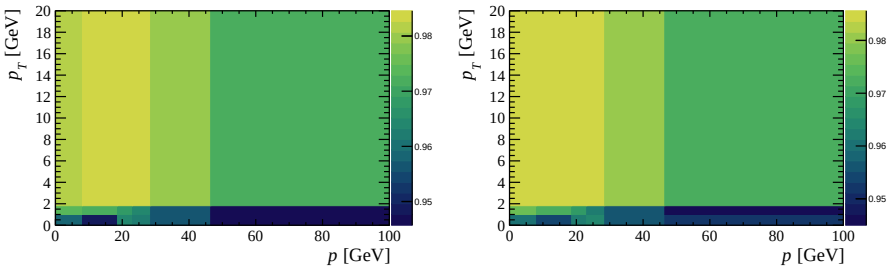

Figure 4.11: PID efficiency maps for muons with `ProbNNMu` > 0.2 for 2018 data for the two different LHCb magnet polarities magnet down (left) and magnet up (right).

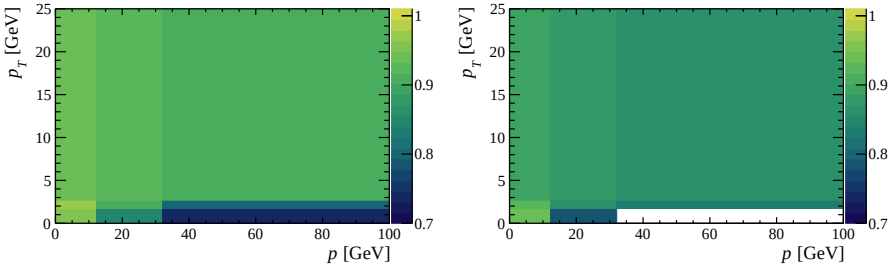

Figure 4.12: PID efficiency maps for electrons with `ProbNNe` > 0.2 for 2018 data for electrons with (left) and without (right) bremsstrahlung photons recovered.

4.4.4 Tracking efficiency

The track reconstruction efficiency is determined from a sample of J/ψ decays that is selected using only a part of the tracking system. The efficiency to reconstruct the full track is then determined using each omitted tracking system in turn. Small differences between the data and MC simulation have been observed in the measured tracking efficiencies. To correct for these differences, correction weights are obtained per long track using the

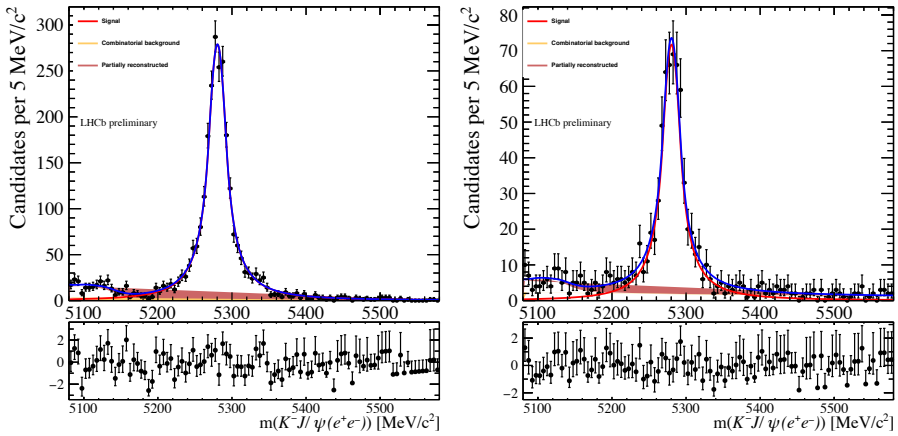

Figure 4.13: $B^+ \to J/\psi(\to e^+e^-)K^+$ invariant mass fits for the pass (left) and fail (right) samples, shown electrons with bremsstrahlung recovery for 2018 Mag Up.

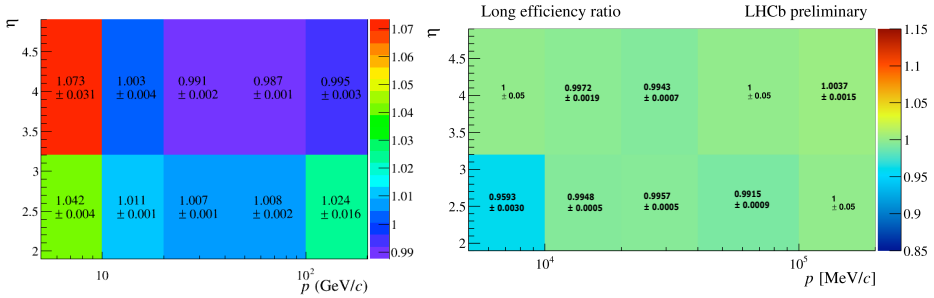

Figure 4.14: Track efficiency correction weights of long tracks, shown for 2012 (left) and 2016 (right) data [60].

`TrackCalib` [60] software. The weights are obtained from two-dimensional look-up tables in track momentum and track pseudo-rapidity. Fig. 4.14 shows two example efficiency maps used. For electrons, the tracking efficiency corrections are obtained from the measured electron tracking efficiencies [61] using three-dimensional maps, binned in the track angles ϕ and η, and transverse momentum of the track.

4.4.5 Trigger efficiency

As explained in Section 3.5, the same trigger thresholds are applied to the simulated sample, as were used in data. To further verify the obtained

trigger efficiencies, the so-called TISTOS method [62] is used on a $B^+ \to J/\psi\,(\to\ \mu^+\mu^-)K^+$ sample. The sample is binned in two dimensions of $\max(p_T^{\ell_1}, p_T^{\ell_2})$ and $p_T^{\ell_1} \times p_T^{\ell_2}$, taken from Ref. [59]. The efficiency is obtained by separately fitting candidates that passed both the signal trigger as well as another trigger selection. The efficiency is calculated using so-called TIS (Trigger Independent of Signal) & TOS (Trigger On Signal) candidates, and candidates that only passed another trigger selection (TIS & not TOS). The resulting efficiency is given by

$$\varepsilon = \frac{N_{TIS\&TOS}}{N_{TIS}} \tag{4.10}$$

The numbers $N_{TIS\&TOS}$ and N_{TIS} are determined in fits, where the shape of the invariant mass distribution of $B^+ \to J/\psi\,(\to \mu^+\mu^-)K^+$ signal candidates is described by a Gaussian function with power-law tails whose parameters are fixed from fits to the simulation. The fits are performed on both the MC simulation and the data, and the ratio of the resulting invariant mass fits is used as the final correction to the simulation. The obtained results are stored in two-dimensional tables from which the efficiency weights are obtained. For a more detailed explanation about the TISTOS method, see Ref. [63]. The TISTOS efficiency maps for 2015 $\Lambda_b^0 \to J/\psi\,(\to \mu^+\mu^-)\Lambda$ data and simulation samples with downstream reconstructed Λ candidates are shown in Fig. 4.15 as an example. The trigger efficiencies are found to be similar in data and simulation, and the resulting correction weights are thus small.

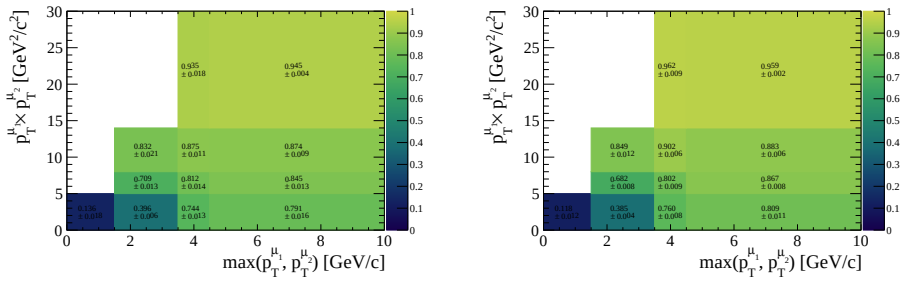

Figure 4.15: TISTOS efficiency maps for the 2015 trigger selection for $\Lambda_b^0 \to J/\psi\,(\to \mu^+\mu^-)\Lambda$ data (left) and simulation (right).

4.4.6 Λ_b^0 production kinematics

A re-weighting procedure is applied to the MC samples in order to correct for the imperfect simulation of the generated b-hadron kinematics. These kinematic weights are extracted with the use of a Gradient Boosted Reweighter (GBR) machine learning algorithm [64]. Gradient boosting is a machine learning technique that builds an ensemble of prediction models (in this case decision trees) in a sequential manner, where each model is trained to minimize the errors of the previous model. The output of all the decision trees is then combined and used for the final output of the model.

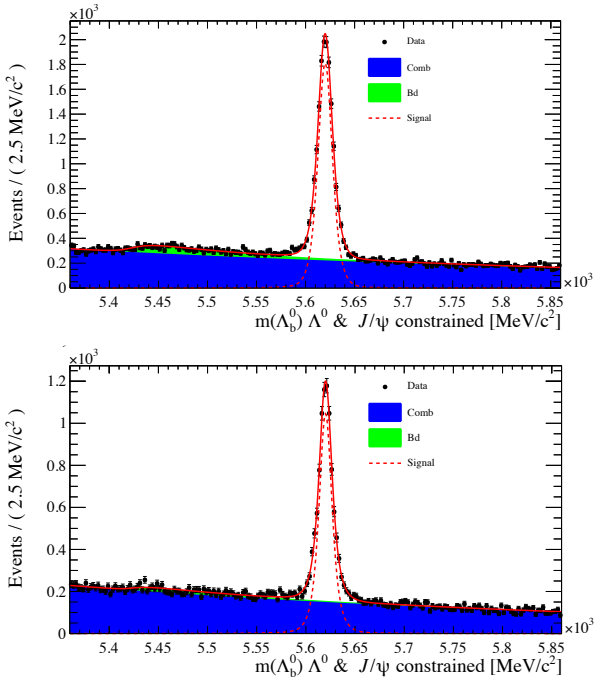

Figure 4.16: Invariant mass sPlot fits of $\Lambda_b^0 \to J/\psi(\to \mu^+\mu^-)\Lambda$ for the 2018 downstream- (top) and long- (bottom) data categories. The fitted Λ_b^0 mass is calculated with the Λ and J/ψ mass constrained to their PDG values. The fitted signal is shown with the red line, the green coloured area shows the fitted $B^0 \to J/\psi(\to \mu^+\mu^-)K_S^0$ background events, and the blue coloured area indicates combinatorial background. The sWeights are extracted and used to reweight the simulation kinematics.

Here, the GBR is trained on so-called 'sWeighted' data obtained through the sPlot method [65] and on simulated $\Lambda_b^0 \to J/\psi(\to \mu^+\mu^-)\Lambda$ events, using the discriminatory variables $p_T(\Lambda_b^0)$ and $\eta(\Lambda_b^0)$. Similarly, the GBR training

is done using $B^+ \to J/\psi(\to \mu^+\mu^-)K^+$ and $B^0 \to J/\psi(\to \mu^+\mu^-)K^0_S$ events, allowing reweighting from an independent data sample and for comparison and systematic checks of the reweighting method. This will be further discussed in Sec. 5.5. The resonant mode analysis uses weights derived from the $B^+ \to J/\psi(\to \mu^+\mu^-)K^+$ sample, while the rare mode and forbidden mode analyses use weights derived from the $\Lambda_b^0 \to J/\psi(\to \mu^+\mu^-)\Lambda$ sample. The sPlot method uses a maximum likelihood fit to determine the signal and background yields in data relative to a discriminating variable, in this case the reconstructed invariant mass $m(\Lambda_b^0)$. Subsequently, a set of sWeights is computed based on the fit results and applied on the data. The sWeights are dependent on $m(\Lambda_b^0)$ and have positive values when the signal contribution is high, and negligible or negative values when the signal contribution is low. Using these sWeights per event, the distributions such as $p_{\mathrm{T}}(\Lambda_b^0)$ and $\eta(\Lambda_b^0)$ are obtained. This procedure statically eliminates the background contributions, making sure that the distributions only reflect the contributions from the signal data.

The sPlot fits follow the same fit strategy as the normalisation channel fits. The fits use a double-sided Crystal Ball shape [66] to model the signal, and includes a Johnson S_U distribution [67] for possible $B^0 \to J/\psi K^0_S$ misidentified background, and an exponential modelling of the combinatorial background. Two example fits to the invariant mass distribution are shown in Fig. 4.16. Figure 4.17 shows the distributions of $p_{\mathrm{T}}(\Lambda_b^0)$, $\eta(\Lambda_b^0)$ and $\chi^2_{VTX}(\Lambda_b^0)$ on sWeighted data and on simulation before and after the application of the weights.

4.4.7 Total correction

To fully correct the simulation to obtain correct efficiencies and mass-fit shapes, all the above-mentioned weights are combined into a single total correction weight. This weight is applied to each simulated event to obtain the final corrected simulation sample. Fig. 4.18 shows the distributions of the total correction weight for the simulated $\Lambda_b^0 \to J/\psi(\to \mu^+\mu^-)\Lambda$ decays for the 2018 samples with the Λ baryon reconstructed with downstream (left) and long (right) tracks. The total correction is comparable for both the downstream and long data category, and peaks around 0.7. Note that the average weight per event is 1.0 by construction to avoid a change in the overall normalisation.

The 2D dependence of the weight on the $p_{\mathrm{T}}(\Lambda_b^0)$ and $\eta(\Lambda_b^0)$ is shown in Fig. 4.19. The distributions show that a high correction is needed for the low (> 1 weights) and high (< 1 weights) p_T regions, which is consistent

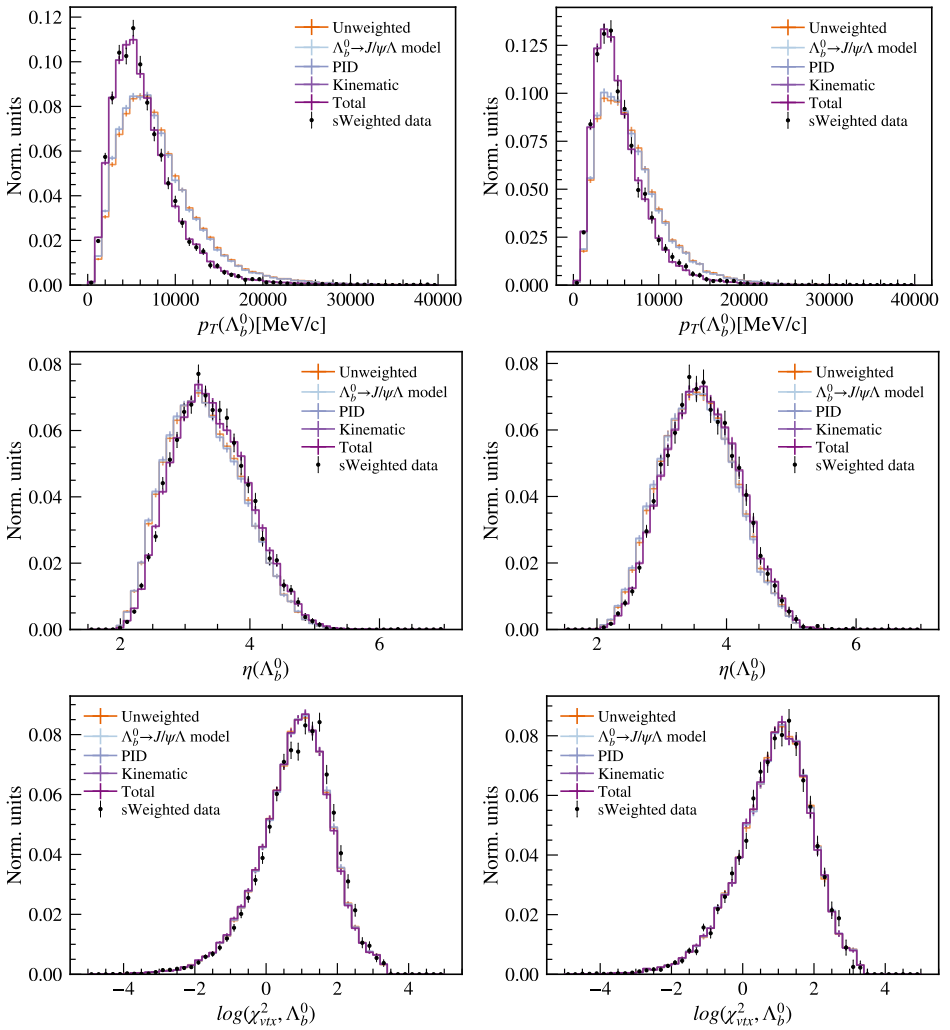

Figure 4.17: $p_{\mathrm{T}}(\Lambda_b^0)$ (top), $\eta(\Lambda_b^0)$ (middle) and $\chi^2_{VTX}(\Lambda_b^0)$ (bottom) distributions for $\Lambda_b^0 \to J/\psi\,(\to \mu^+\mu^-)\Lambda$ decays for sWeighted data (black points) and simulation before (orange lines) and after (dark purple line) the re-weighting. The left graphs show the candidates with the Λ reconstructed using downstream tracks in 2018 data sample, while the right shows the long track sample for 2018 data. The effect of the tracking and trigger weights are included in the "Total", and have a small effect. Therefore, the "Total" and "Kinematic" lines almost completely overlap.

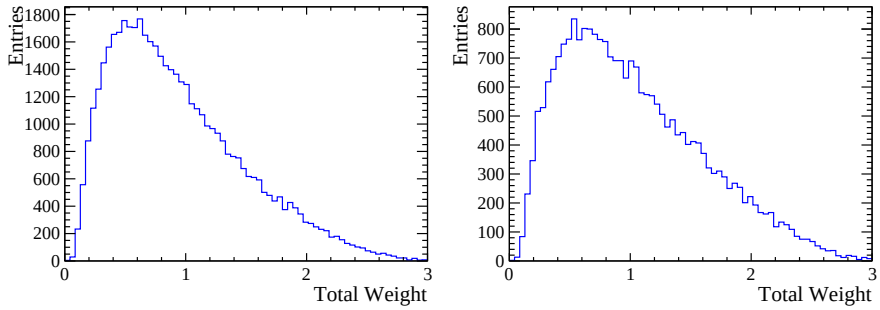

Figure 4.18: Histograms showing the total correction weight for the $\Lambda_b^0 \to J/\psi(\to \mu^+\mu^-)\Lambda$ channel in the 2018 downstream- (left) and long- (right) track reconstructed Λ hadron data categories.

with the behavior seen in Fig. 4.17.

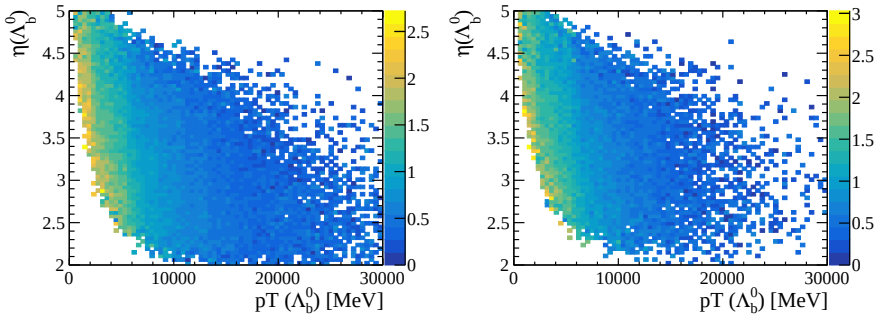

Figure 4.19: 2D distributions in p_T and η of the Λ_b^0 candidate, showing the total correction weight for $\Lambda_b^0 \to J/\psi(\to \mu^+\mu^-)\Lambda$ decays in 2018 simulation using downstream- (left) and long- (right) track reconstructed Λ candidates.

4.5 MVA

The preselections that are applied on the data and MC simulation, as described in Sec. 4.3, reduce the amount of background events significantly. For the $\mathcal{B}(\Lambda_b^0 \to J/\psi\,\Lambda)$ analysis, the selection is sufficient to extract a clean signal yield. However, for the R_Λ and $\Lambda_b^0 \to \Lambda e^\pm \mu^\mp$ analyses, as the signal decays are very rare, further background rejection is needed. Therefore, a multivariate analysis (MVA) technique is used. A MVA is a machine learning technique that uses a set of input variables to classify events into different categories, such as signal and background events. More specifically, here a Boosted Decision Tree (BDT) is used. A BDT is a form of machine learning that combines decision trees and the boosting technique, as mentioned before in Sec 4.4.6, to build a prediction model [68]. The decision trees consist of a series of binary selections, where each node in the tree represents a single variable and selection value, and each branch represents the outcome of the selection. In a BDT, decision trees are used as so-called 'weak learners', which are trained sequentially by boosting to improve their predictive performance. The boosting process iteratively combines the decision trees, giving more weight to data points that were misclassified in previous iterations, to create an ensemble model that improves overall predictive accuracy. The outputs of all the trained decision trees are then combined to into a final output of the BDT, in this case a per-event score between -1 and 1 with the most signal-like events scoring close to 1 and the more background-like events scoring closer to -1.

To achieve further rejection of combinatorial background, BDTs are trained using weighted simulated signal $\Lambda_b^0 \to \Lambda e^\pm \mu^\mp$, $\Lambda_b^0 \to \Lambda e^+ e^-$, or $\Lambda_b^0 \to \Lambda \mu^+ \mu^-$ decays as the signal sample. An overview of the included variables and their relative importance in the BDT training is shown in Fig 4.21. Combinatorial background data obtained from the Λ_b^0 mass sidebands surrounding the expected signal is used as background sample for training. The BDTs are trained using an equal number of signal and background candidates, where the total sample size is determined by the size of the simulated sample. The data background candidates are randomly drawn from the full samples to match the sample size of the simulation. This is done to prevent bias due to either a larger or lower amount of background candidates in the data compared to the simulation. To avoid performance estimation bias and prevent overtraining, the k-folding cross-validation technique is used [70].

The optimal working point of the BDT is determined by maximizing the

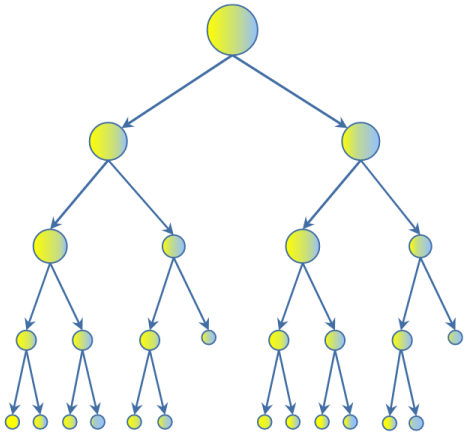

Figure 4.20: Schematic drawing of a decision tree using two colors to represent background and signal categories. The circular nodes in the diagram represent the leaves of the tree, and the arrows represent a selection on one of the input variables. Each layer in the diagram corresponds to a decision layer in the tree. Figure adapted from Ref. [69]

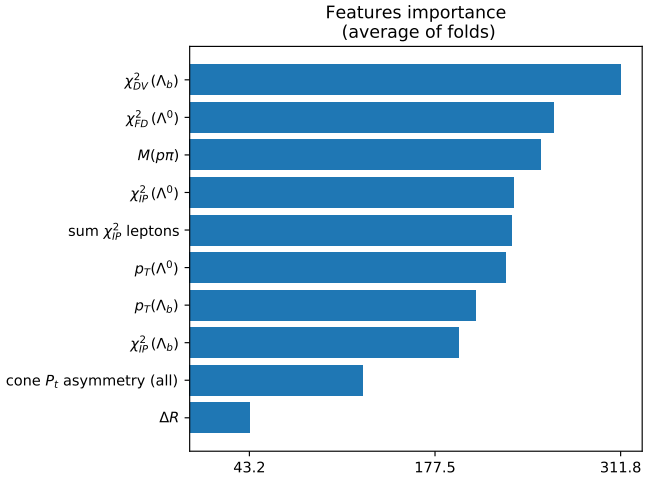

Figure 4.21: Relative importance ranking of the variables used in the $\Lambda_b^0 \to \Lambda e^+ e^-$ BDT training. The included variables describe vertex quality, kinematics, and matching of the interaction point for the different particles.

Figure of Merit (FoM) [71] defined as:

$$\text{FoM} = \frac{\text{S}}{\sqrt{\text{B} + \sigma/2}} \tag{4.11}$$

where S is the signal efficiency taken from MC simulation, and B is the estimated background yield, both after a specific BDT selection respectively, and σ is the number of standard deviations of signal significance the FoM aims for. For both the R_Λ and $\Lambda_b^0 \to \Lambda e^\pm \mu^\mp$ analyses, σ is set to 3. The background estimate B is obtained by fitting the data sideband distribution with an exponential function, and extrapolating the fit to the signal region. To prevent random fluctuations from skewing the optimal working point, the FoM is calculated for the moving average over 5 consecutive BDT selection working points in steps of 0.01.

To evaluate the MVA performance, the Receiver Operating Characteristic (ROC) curve is used. The ROC curve shows the signal efficiency and the background rejection of the BDT as the selection on the BDT output variable is varied. It is used to compare the performance between the different data categories and to optimize the discrimination threshold for a given classifier. Additionally, the area under the ROC curve (AUC) provides a single scalar value that summarizes the overall performance of the MVA, with a value of 1 indicating perfect performance and a value of 0.5 indicating a random classifier. The trained BDT is also checked for overtraining. To check for overtraining, the available data is split into two parts: a training set and a test set. The BDT is trained on the training set and its performance is evaluated on both the training and test set, which should have similar performance. If the performance on the test set is significantly worse than on the training set, the BDT is overtrained on the specific sample used.

Overtraining checks, ROC curves, and BDT optimization distributions for the $\Lambda_b^0 \to \Lambda e^+ e^-$ BDT are shown in Fig. 4.22 and 4.23. Tables 4.2-4.4 show the FoM-optimized working points for all trained BDTs. A combinatorial background rejection over 90% is achieved for all BDTs, while keeping a signal efficiency between $30 - 50\%$.

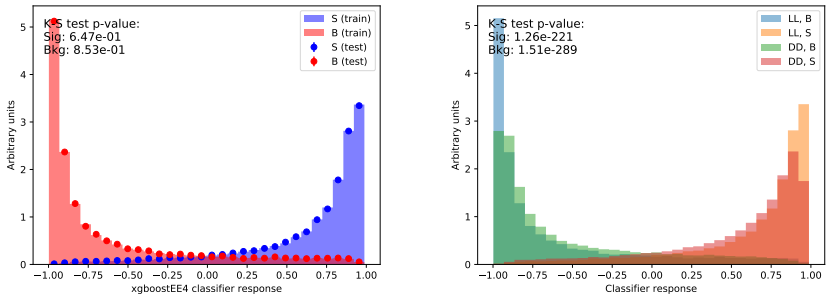

Figure 4.22: Left: overtraining check for the trained $\Lambda_b^0 \to \Lambda e^+ e^-$ BDT using long tracks. Good agreement is visible between the training and testing response, therefore no overtraining is present. Right: response of the $\Lambda_b^0 \to \Lambda e^+ e^-$ BDT compared for the long and downstream track data categories. A better performance is observed for long compared to downstream data, most likely due to the better resolution of the input variables of the long track sample.

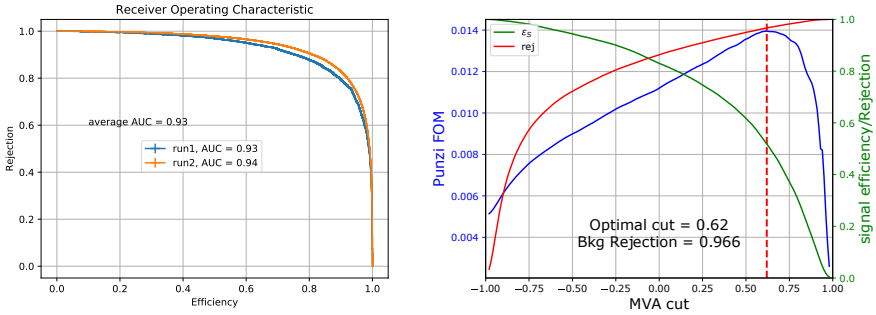

Figure 4.23: Left: ROC curve comparison for the Run 1 and Run 2 data, showing a comparable performance. Right: example FoM scan for the $\Lambda_b^0 \to \Lambda e^+ e^-$ BDT in the Run 2 DD data using downstream reconstructed Λ candidates and the single photon brem. recovery category. An optimal cut value of 0.62 is found for this example.

Table 4.2: Optimised BDT output selection per data category for the $\Lambda_b^0 \to \Lambda e^+ e^-$ BDT. The selection matching Fig. 4.23 is highlighted in bold. 0γ stands for no reconstructed bremsstrahlung photons, 1γ for one reconstructed bremsstrahlung photon, and 2γ for two reconstructed bremsstrahlung photons, respectively.

Category	ϵ_{Signal}	Background rejection	BDT cut value
0γ LL Run 1	0.765	0.916	0.340
0γ LL Run 2	0.675	0.950	0.510
0γ DD Run 1	0.568	0.949	0.470
0γ DD Run 2	0.483	0.973	0.630
1γ LL Run 1	0.726	0.917	0.460
1γ LL Run 2	0.591	0.967	0.670
1γ DD Run 1	0.600	0.948	0.530
1γ DD Run 2	0.519	0.967	**0.620**
2γ LL Run 1	0.781	0.920	0.420
2γ LL Run 2	0.658	0.955	0.620
2γ DD Run 1	0.146	0.998	0.900
2γ DD Run 2	0.464	0.975	0.710

Table 4.3: Optimised BDT output selection per data category for the $\Lambda_b^0 \to \Lambda e^{\pm} \mu^{\mp}$ BDT.

Category	ϵ_{Signal}	Background rejection	BDT cut value
0γ LL Run 1	0.422	0.985	0.740
0γ LL Run 2	0.341	0.995	0.820
0γ DD Run 1	0.366	0.988	0.850
0γ DD Run 2	0.316	0.995	0.870
1γ LL Run 1	0.343	0.993	0.840
1γ LL Run 2	0.453	0.989	0.750
1γ DD Run 1	0.349	0.991	0.880
1γ DD Run 2	0.310	0.995	0.890

Table 4.4: Optimized BDT output selection per data category for the $\Lambda_b^0 \to \Lambda \mu^+ \mu^-$ BDT.

Category	ϵ_{Signal}	Background rejection	BDT cut value
LL Run 1	0.497	0.979	0.880
LL Run 2	0.554	0.989	0.880
DD Run 1	0.522	0.984	0.900
DD Run 2	0.539	0.984	0.900

4.6 Efficiency calculation

An important input for the three analyses is the efficiency of the reconstruction and selection of the signal events. The total efficiency is a product of multiple separate efficiencies:

- ε_{Gen}: the generator level efficiency,
- $\varepsilon_{\text{Strip + rec}}$: the efficiency of the stripping and reconstruction,
- $\varepsilon_{\text{Track}}$: the efficiency of the LHCb tracking,
- ε_{Sel}: the efficiency of the selection. Further split into the pre-selection, q^2 selection, DecayTreeFitter convergence, and the TT sensor veto efficiencies.
- ε_{PID}: the efficiency of the lepton PID selection,
- $\varepsilon_{\text{Trig}}$: the efficiency of the trigger selection. Further split into the L0, HLT1 and HLT2 trigger efficiencies,

The efficiencies are calculated sequentially from corrected simulation samples, per year of data-taking, per magnet polarity, and split in the downstream or long $K^0_S(\Lambda)$ track type.

The generator level efficiency ε_{Gen} is calculated from a sample of simulated events in the full 4π angular space. For the control mode $\mathcal{B}(\Lambda^0_b \to J/\psi\,\Lambda)$ analysis, only the events falling within the LHCb acceptance are considered to pass the generator level selection, as the measurement only cares about the region where $f_{\Lambda^0_b}/f_d$ known. This corresponds to $60-70\%$ of events. However for the rare mode R_Λ and forbidden mode $\Lambda^0_b \to \Lambda e^\pm \mu^\mp$ analyses, the full 4π angular space is considered, leading to a generator level efficiency of around $18-19\%$. Afterwards events are selected that passed the LHCb reconstruction and the loose stripping selections. The efficiency of this selection is denoted as $\varepsilon_{\text{Strip + rec}}$. The efficiency is calculated by comparing the number of events reconstructed in the corrected simulation sample to the number of events in the generator level sample. For the decays of interest, the $\varepsilon_{\text{Strip + rec}}$ is higher for downstream reconstructed K^0_S/Λ hadrons (typically 3% for $\Lambda^0_b \to J/\psi\,\Lambda$) than hadrons reconstructed from long tracks (typically 2% for $\Lambda^0_b \to J/\psi\,\Lambda$). This is due to the fact that the long tracks are required to have at least three hits in the VELO, which due to the long lifetime of the hadrons is not guaranteed.

The tracking efficiency $\varepsilon_{\text{Track}}$, trigger efficiency $\varepsilon_{\text{Trig}}$, and PID efficiency ε_{PID} are calculated using the methods as described in Sec. 4.4. The selection efficiency ε_{Sel} is calculated by using the number of events passing the selections. The exact selection differs per analysis, as mentioned in Sec. 4.3.

Once all the efficiencies are calculated, the total efficiency is obtained by multiplying all the efficiencies together. The total efficiencies per year and polarity are then combined using a weighted average, where the weights correspond the fraction of the total luminosity of the year and polarity. Efficiency tables for the different analysis are shown in the corresponding analysis chapters.

4.7 Maximum-likelihood fits

The signal and normalisation yields are extracted using a maximum-likelihood fit to the invariant mass distribution of the selected candidates. In general, likelihood fits are used to extract model parameters that best describe the data, often called $\hat{\theta}$. This is done by maximizing the likelihood function, which is described by the probability of the data given the model parameters. The likelihood function is defined as:

$$\mathcal{L}(\theta) = \prod_{i=1}^{N} f(x_i|\theta) \ , \tag{4.12}$$

where $f(x_i|\theta)$ is the probability density function (PDF) of the i-th candidate, and θ is the set of parameters of the PDF.

As the number of candidates in the used datasets is large, the expected amount of events is described by a Poisson distribution. To take this into account, the likelihood function is modified to:

$$\mathcal{L}(\theta) = \frac{\mu(\theta)^N e^{-\mu(\theta)}}{N!} \prod_{i=1}^{N} f(x_i|\theta) \ , \tag{4.13}$$

where N is the total number of candidates, and $\mu(\theta)$ is the expected mean number of events given the model parameters. Eq. 4.13 is also called the extended likelihood function. Using an extended likelihood function allows the use of extra information of N in the fit, instead of only x, which can be used to further constrain the model parameter uncertainties.

The model parameters are extracted by maximizing the likelihood function. In practice, this is done by minimizing the negative log-likelihood function, as taking the logarithm of the likelihood function simplifies the

calculations needed for the minimization. Taking the logarithm converts the product of PDFs into a sum of logarithms of the PDFs, defined as:

$$\ln \mathcal{L}(\theta) = \sum_{i=1}^{N} \ln(\mu(\theta) f(x_i|\theta)) - \mu(\theta) \ , \tag{4.14}$$

omitting terms that do not depend on θ. For the analyses described in this thesis, unbinned extended likelihood fits are used to extract the signal and normalisation yields, which will be described in more detail in the corresponding analysis chapters.

5 The resonant mode: $\mathcal{B}(\Lambda_b^0 \to J/\psi\,\Lambda)$ analysis

This chapter describes the analysis to measure the branching fraction of the resonant $\Lambda_b^0 \to J/\psi\,\Lambda$ mode. This measurement was last updated by the D0 collaboration, and has a large uncertainty [48]. As the branching fraction is used as an input for the decay rate measurement of the rare mode $\Lambda_b^0 \to \Lambda\mu^+\mu^-$, as well as for the forbidden mode $\Lambda_b^0 \to \Lambda e^\pm\mu^\mp$ analysis, an improved measurement is desirable. The general method of the $\Lambda_b^0 \to \Lambda\ell^+\ell^-$ analyses was introduced in the previous chapter. Here, the aspects specific to the $\mathcal{B}(\Lambda_b^0 \to J/\psi\,\Lambda)$ analysis are discussed. Firstly, the need for a dedicated detector acceptance criterium is described. Secondly, the efficiencies are presented. Thirdly, the invariant mass fits are described and shown, followed by the branching fraction measurement. Finally, the systematic uncertainties of the measurement are discussed.

5.1 Effect of missing TT sensor

The momenta of the final state particles are measured using the tracking system using the VELO and TT upstream of the magnet, and the T-stations downstream of the magnet. However, the here-studied K_S^0 and Λ hadrons are long living particles, with a $c\tau \approx 1 - 2$m, which means that they often decay outside the VELO detector, leaving no hits in the VELO sensors. In these cases, as mentioned in Sec. 3.3, they are reconstructed as downstream tracks using only hits from the TT and T-stations. Since the TT is located before the magnet, a track momentum estimate can still be made.

To ensure that the MC simulation is a good representation of the data sucht that it can be correctly used to calculate efficiencies, kinematic distributions of the reconstructed particles in data and MC simulation are compared.

Fig. 5.1 shows the pseudorapidity (η) and azimuthal (ϕ) distributions of the K_S^0 hadron in the $B^0 \to J/\psi\,(\to \mu^+\mu^-)K_S^0$ decay in 2016 and 2018 samples for downstream reconstructed K_S^0 candidates. There is a clear discrepancy between data and MC simulation with a lower than expected amount of data in the high η and ϕ region in the 2018 distribution, while this is not present for the 2016 data. The discrepancy is also visible in the distributions of the Λ hadron in the $\Lambda_b^0 \to J/\psi\,(\to \mu^+\mu^-)\Lambda$ decay, as shown in Fig. 5.2. This effect is, however, not present in the samples with the K_S^0 or Λ hadrons reconstructed using long tracks.

To check for any potential issues with the TT detector, the x and y coordinates of the K_S^0 and Λ trajectories at $z = 235\,\text{cm}$ (corresponding to the TT position in the detector) are plotted for the 2016 and 2018 data samples, as shown in Fig. 5.3. The x and y coordinates of the K_S^0 and Λ trajectories are expected to be distributed uniformly, but an underfluctuation is visible in the negative x and positive y region in 2018 data.

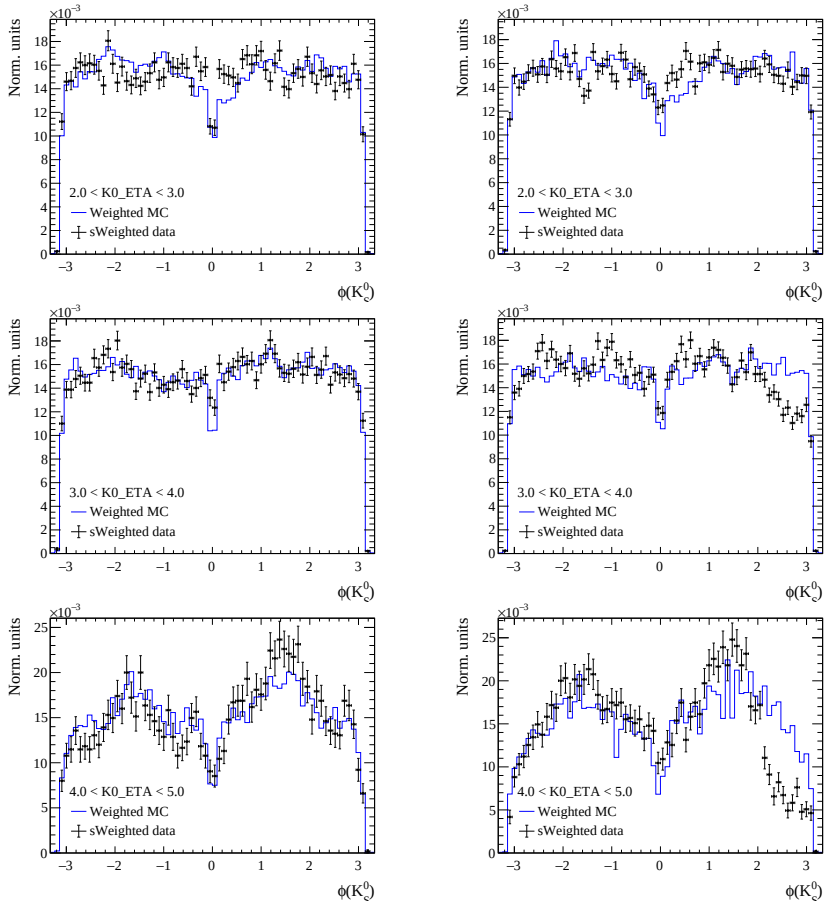

Figure 5.1: sWeighted data and MC simulation $\phi(K^0_S)$ comparison for $B^0 \to J/\psi(\to \mu^+\mu^-)K^0_S$ decays for the 2016 (left) and 2018 (right) samples in different bins of $\eta(K^0_S)$ with the K^0_S reconstructed using downstream tracks. A discrepancy is visible for 2018 in the high η and ϕ region.

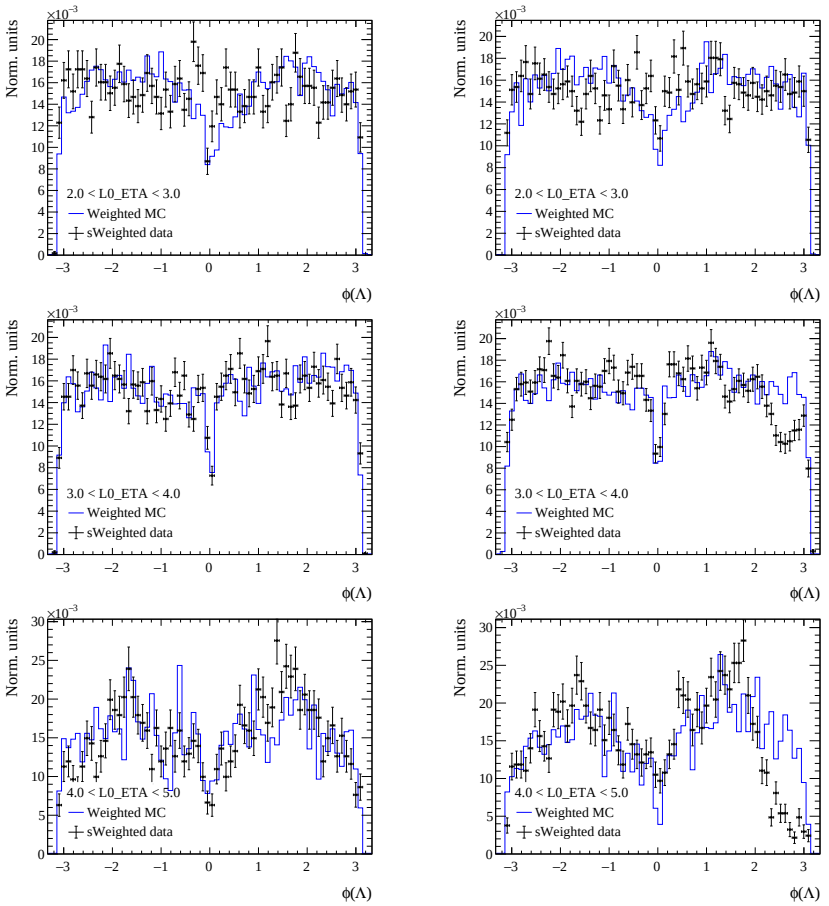

Figure 5.2: sWeighted data and MC simulation $\phi(\Lambda)$ comparison for $\Lambda_b^0 \to J/\psi(\to \mu^+\mu^-)\Lambda$ decays for the 2016 (left) and 2018 (right) samples in different bins of $\eta(\Lambda)$ with the Λ reconstructed using downstream tracks. A discrepancy is visible for 2018 in the high η and ϕ region.

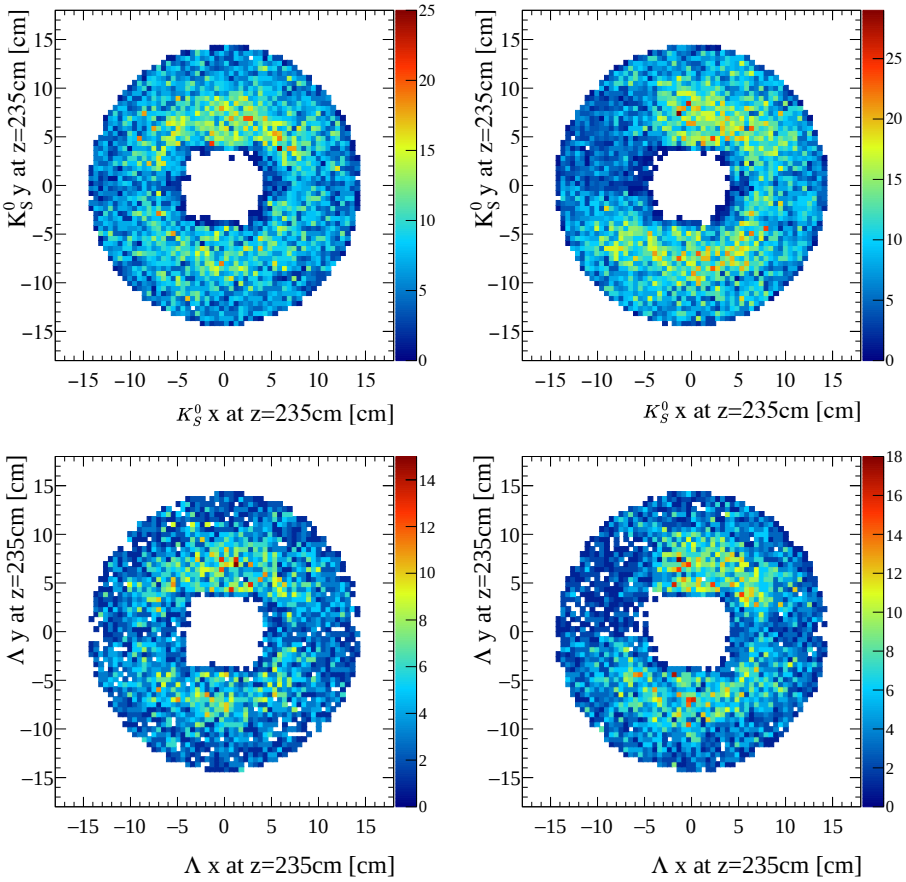

Figure 5.3: Two-dimensional distributions of the x and y coordinate of the K^0_S in $B^0 \to J/\psi K^0_S$ (top) and Λ in $\Lambda^0_b \to J/\psi \Lambda$ decays (bottom) trajectory at $z = 235\,\text{cm}$ corresponding to the u layer of the TT for data in 2016 (left) and 2018 (right). Only the K^0_S and Λ candidates with $\eta > 3.0$ are shown. An underfluctuation in the expected amount of events is visible in the negative x and positive y region in 2018 data. The area in the center without datapoints corresponds to the beampipe position, where the TT has no sensors.

The loss of events in the negative x and positive y region indicates a potential problem with a sensor in the TT during the data taking period in 2017 and 2018. As a downstream track requires hits in 3 of the 4 TT layers, a broken sensor in one of the layers could cause the drop in events. As it turned out, in September 2017 a sensor in the stereo u layer of the TT broke due to a power supply failure [72]. Fig. 5.4 shows the relative occupancy of the TT layers in 2017 data, where the broken sensor is visible as a grey rectangle. The sensor is positioned in the high occupancy region of the u layer, close to the beampipe, with a position of -3.87 to -13.51 cm in x and 0.00 to 9.44 cm in y, corresponding to the region with a lack of events, as seen in Fig. 5.3.

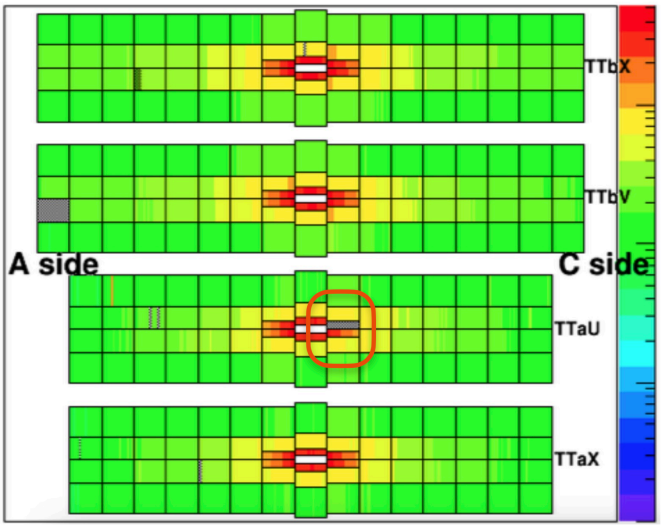

Figure 5.4: Relative occupancy distribution of the TT layers in 2017 data [72]. The red circle at the u layer indicates the broken sensor in the high occupancy region.

The MC simulation does not exclude the sensor, explaining the differences seen between the data and simulation. To correct for this, a veto is applied to remove events in the region where the sensor is broken. When one or both tracks forming the Λ or K_S^0 candidate are reconstructed in the above-mentioned region with the broken sensor, the event is removed. The veto is applied to the 2017 and 2018 data samples, as the sensor only broke in 2017, as well as the corresponding MC simulation samples, removing roughly 5% of all events. Fig. 5.5 shows the η and ϕ distributions of the K_S^0 (Λ) hadron in the $B^0 \to J/\psi(\to \mu^+\mu^-)K_S^0$ ($\Lambda_b^0 \to J/\psi(\to \mu^+\mu^-)\Lambda$) decays in 2018 samples

for downstream reconstructed K_S^0 (Λ) candidates after applying the TT sensor veto. The discrepancy between data and MC simulation is no longer visible, indicating the veto is working as intended. The veto is therefore included in the analysis, and applied during the selection stage.

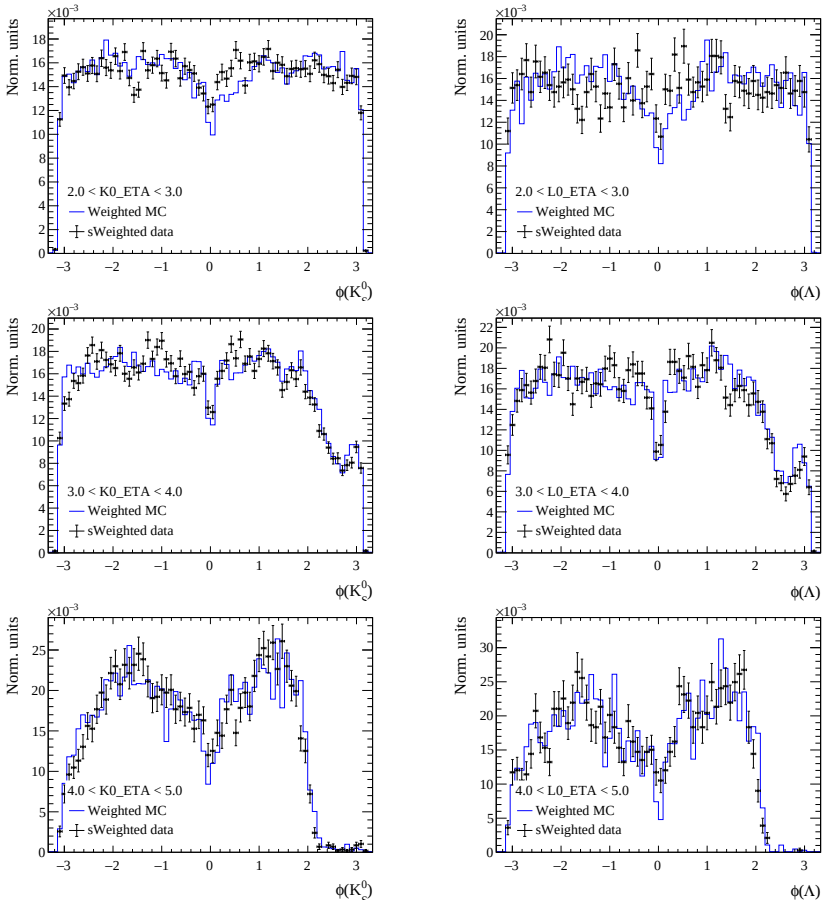

Figure 5.5: sWeighted data and MC simulation comparison for $B^0 \to J/\psi(\to \mu^+\mu^-)K_S^0$ (left) and $\Lambda_b^0 \to J/\psi(\to \mu^+\mu^-)\Lambda$ (right) decays for the 2018 samples with the K_S^0 and Λ hadrons reconstructed using downstream tracks after applying the TT sensor veto. Good agreement between data and MC simulation is visible.

5.2 Efficiencies

The signal selection efficiencies are calculated using corrected MC simulation samples, as described in Sec. 4.6. The efficiencies are calculated for the 2016, 2017, and 2018 data taking periods separately, as well as per magnet polarity and track type category. The tables in App. C show the efficiencies averaged over all b-hadron p_T bins for the $B^0 \to J/\psi(\to \mu^+\mu^-)K^0_S$ and $\Lambda_b^0 \to J/\psi(\to \mu^+\mu^-)\Lambda$ decays, for K^0_S and Λ hadrons reconstructed with downstream and long tracks respectively, for both magnet polarities. As an example here, Tab. C.3 shows the efficiency of the $\Lambda_b^0 \to J/\psi(\to \mu^+\mu^-)\Lambda$ decay in the 2016, 2017, and 2018 data taking periods for the downstream reconstructed Λ hadron.

As the signal extraction is done in bins of b-hadron p_T, the efficiencies are also calculated in bins of p_T. The efficiencies in bins of the p_T are shown in Fig. 5.6, where the 16+17+18 efficiency is the luminosity-scaled combination of the individual data-taking years. The efficiency in the different years is in good agreement, and the efficiency for downstream reconstructed K^0_S (Λ) hadrons is higher than for long tracks as more of the hadrons decay outside of the VELO. A decreasing efficiency at high p_T is visible for long track candidates, most likely due to the long-track requirement of at least three VELO hits. High p_T b-hadrons have a higher boost, and therefore the K^0_S and Λ hadrons are more likely to decay beyond the VELO acceptance. They are therefore less likely to contain three VELO sensor hits, resulting in a lower track finding efficiency.

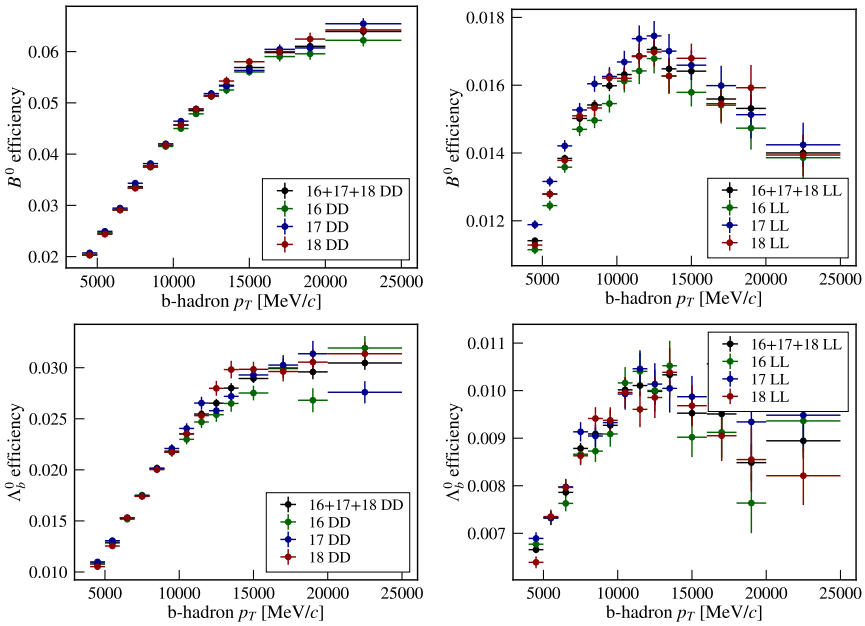

Figure 5.6: Total selection efficiencies in bins of the b-hadron p_T for $B^0 \to J/\psi(\to \mu^+\mu^-)K^0_S$ (top) and $\Lambda^0_b \to J/\psi(\to \mu^+\mu^-)\Lambda$ (bottom) decays, split by the K^0_S (Λ) reconstructed with downstream (left) or long (right) tracks. Note that 25% of all generated events fall in the first bin, and a total of 70% in the first three bins, explaining the lower seeming total integrated efficiency in the tables. The different years are in good agreement.

Table 5.1: Efficiency of $\Lambda^0_b \to J/\psi(\to \mu^+\mu^-)\Lambda^0$ events in downwards magnet polarity MC simulation using Λ reconstructed using downstream tracks.

Categories	Weighted Efficiency (%)		
	2016	2017	2018
Generator	62.79 ± 0.06	62.79 ± 0.06	62.79 ± 0.06
Stripping + rec.	3.972 ± 0.020	3.372 ± 0.016	3.179 ± 0.015
PID	94.95 ± 0.18	94.85 ± 0.17	95.47 ± 0.17
L0 trigger	68.69 ± 0.25	73.70 ± 0.22	71.27 ± 0.23
HLT1 trigger	94.36 ± 0.14	94.34 ± 0.13	94.72 ± 0.13
HLT2 trigger	94.63 ± 0.15	94.50 ± 0.14	95.37 ± 0.13
Pre-Selection	77.21 ± 0.27	78.02 ± 0.25	78.02 ± 0.25
q^2 selection	95.10 ± 0.15	94.84 ± 0.15	94.91 ± 0.15
DTF converged	99.93 ± 0.01	99.92 ± 0.02	99.92 ± 0.02
Faulty TT sensor Veto	N/A	93.70 ± 0.17	94.18 ± 0.17
Total efficiency	1.697 ± 0.012	1.456 ± 0.010	1.362 ± 0.010

5.3 Invariant mass fits

The signal and normalisation yields are extracted from the maximum-likelihood invariant mass fits to the $\Lambda_b^0 \to J/\psi\,(\to \mu^+\mu^-)\Lambda$ and $B^0 \to J/\psi\,(\to \mu^+\mu^-)K_S^0$ decays, as described in Sec 4.7. The invariant mass fits are performed in bins of the b-hadron p_T, corresponding to the binning of the $f_{\Lambda_b^0}/f_d$ measurement, and are done for downstream and long track K_S^0 and Λ candidates separately. The fits consist of different components, where the yield is always free to float:

- **Signal:** The signal component is modelled by a Hypatia function [73]. All shape parameters are fixed from MC simulation, except the mean μ and width σ.
- **Mis-ID:** The mis-identified background component, describing the candidates where a pion from a $B^0 \to J/\psi\,(\to \mu^+\mu^-)K_S^0$ decay is misidentified as a proton. Similarly, the proton from the $\Lambda_b^0 \to J/\psi\,(\to \mu^+\mu^-)\Lambda$ decay can be misidentified as a pion. The background is modelled using a Johnson S_U distribution [67], where all parameters are fixed from MC simulation.
- $\boldsymbol{B_s^0}$**:** This component is only present for the $B^0 \to J/\psi\,(\to \mu^+\mu^-)K_S^0$ invariant mass fits. It represents the background coming from $B_s^0 \to J/\psi\,(\to \mu^+\mu^-)K_S^0$ decays, and is modelled by a copy of the signal shape from MC simulation, with a shifted μ to the PDG B_s^0 mass.
- $\boldsymbol{\Xi_b}$**:** This background is only present for the $\Lambda_b^0 \to J/\psi\,(\to \mu^+\mu^-)\Lambda$ invariant mass fits with downstream reconstructed Λ hadrons. It describes the background coming from $\Xi_b \to J/\psi\,(\to \mu^+\mu^-)\Xi$ decays, where the Ξ decays to a Λ and a pion, where the pion is not reconstructed. The background is modelled with a Johnson S_U distribution with all parameters fixed from MC simulation.
- **Combinatorial background:** The combinatorial background is modelled by a single exponential function. The shape is not taken from MC simulation, but fitted directly on the data.

For a more detailed description of the used mass shapes, see App. D. The invariant mass fits are performed on the combined 2016, 2017 and 2018 data samples, with the efficiency per year scaled by the corresponding luminosity. The resulting fits for all b-hadron p_T bins are shown in App. E. Fig. 5.7 shows the invariant mass fits on MC simulation from which the shape parameters

are obtained for $\Lambda_b^0 \to J/\psi(\to \mu^+\mu^-)\Lambda$ using downstream reconstructed Λ candidates in the $6000 < p_T < 7000\,\text{MeV}$ bin. This process is repeated for all b-hadron p_T bins, and for both track type categories. The obtained shape parameters are then used to fit the invariant mass distributions on the corresponding data sample in all the p_T bins, as shown in Fig. 5.8 with an example fit to events in the $6000 < p_T < 7000\,\text{MeV}$ bin.

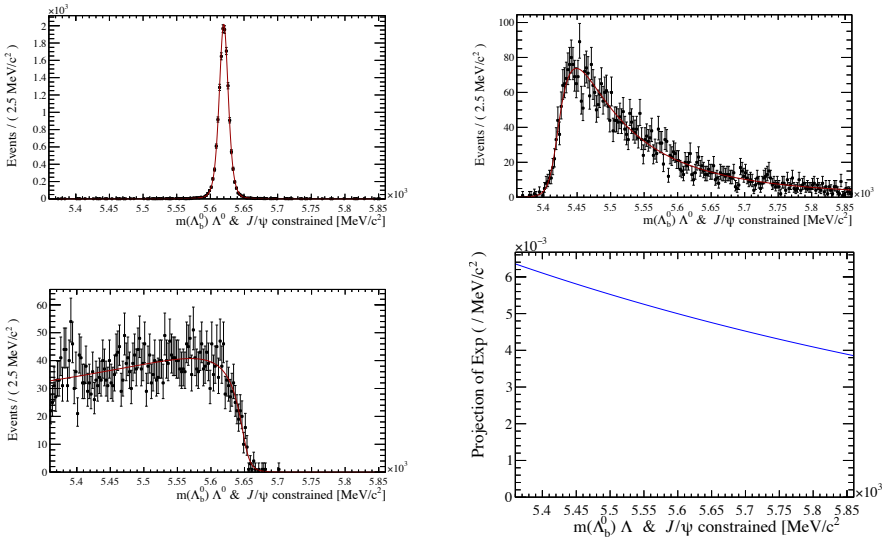

Figure 5.7: Invariant mass likelihood fits on MC simulation for signal (top left), misID (top right), Ξ_b (bottom left) and the combinatorial background shape (bottom right) for the $\Lambda_b^0 \to J/\psi(\to \mu^+\mu^-)\Lambda$ decay in the combined 2016, 2017 and 2018 samples using downstream reconstructed Λ hadrons.

Fig. 5.9 shows the invariant mass fit yields (top) and efficiency-corrected yields (bottom) for the $\Lambda_b^0 \to J/\psi(\to \mu^+\mu^-)\Lambda$ and $B^0 \to J/\psi(\to \mu^+\mu^-)K_S^0$ decays in all bins of the b-hadron p_T. The efficiency corrected yields are calculated by dividing the invariant mass fit yields by the corresponding efficiency in the same bin. The efficiency corrected yields for the downstream- and long-track categories agree within uncertainties, showing that the efficiencies are well understood. The jump in the fitted yield at $p_T = 15000\,\text{MeV}$ is due to the binning in p_T, as the bin size becomes larger at this point.

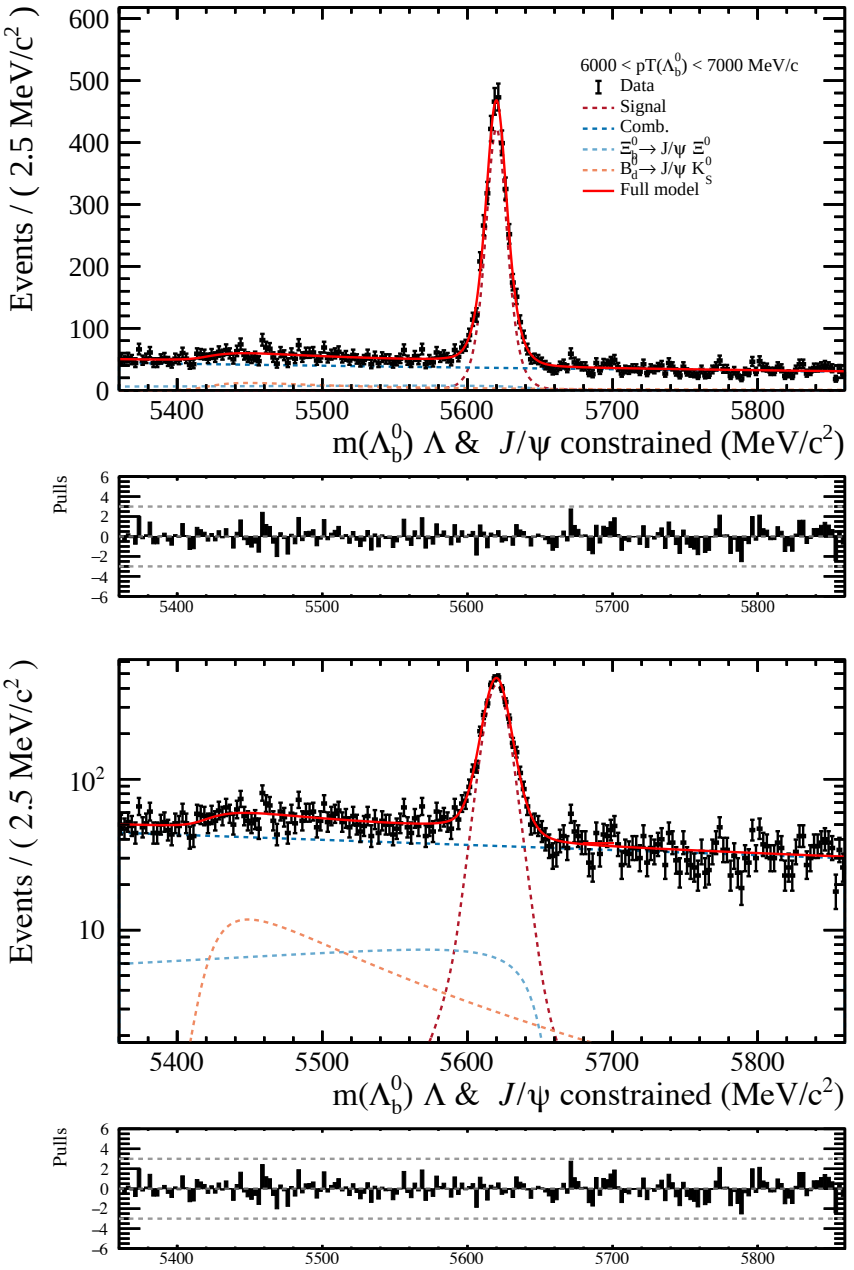

Figure 5.8: Invariant mass fit for the $\Lambda_b^0 \to J/\psi\,(\to \mu^+\mu^-)\Lambda$ decay in the combined 2016, 2017 and 2018 data samples using downstream reconstructed Λ hadrons in the $6000 < p_T < 7000\,\text{MeV}$ bin in linear (top) and log (bottom) scale.

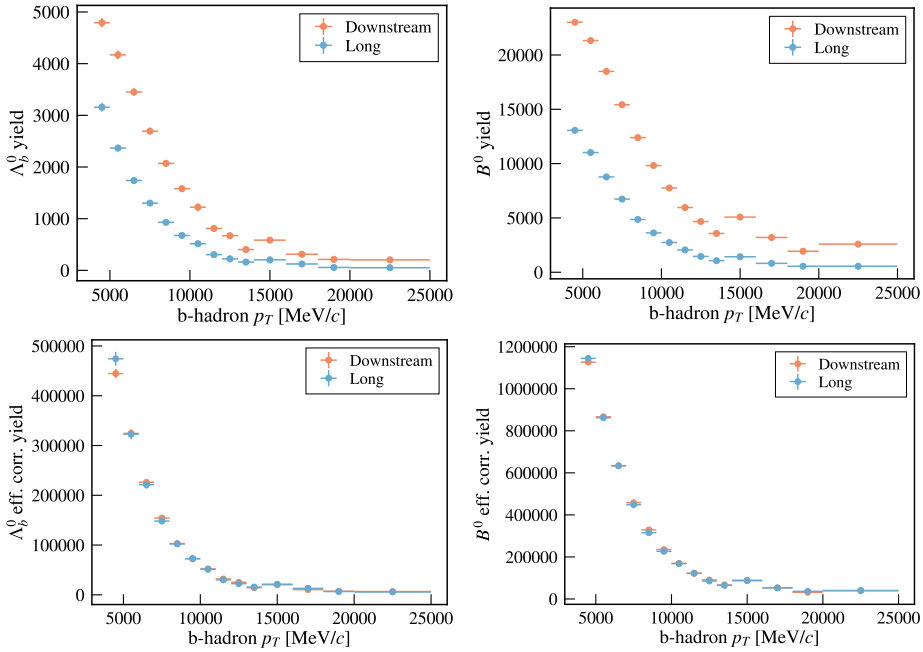

Figure 5.9: Signal invariant mass fit yields (top) and efficiency-corrected yields (bottom) for the $\Lambda_b^0 \to J/\psi(\to \mu^+\mu^-)\Lambda$ (left) and $B^0 \to J/\psi(\to \mu^+\mu^-)K_S^0$ (right) decays in bins of the b-hadron p_T in the combined 2016, 2017 and 2018 data sample for downstream (red) and long (blue) reconstructed K_S^0 and Λ candidates. The efficiency corrected yields for the downstream- and long-track categories agree within uncertainties.

5.4 Results

Using the invariant mass fit yields combined with the selection efficiencies, the $\mathcal{B}(\Lambda_b^0 \to J/\psi\,\Lambda)$ can be calculated using Eq. 5.1:

$$\frac{N_{J/\psi\,\Lambda}(p_{\mathrm{T}})}{N_{J/\psi\,K^0_{\mathrm{S}}}(p_{\mathrm{T}})} = \frac{f_{\Lambda_b^0}}{f_d}(p_{\mathrm{T}}) \times \frac{\mathcal{B}(\Lambda_b^0 \to J/\psi\,\Lambda)}{\mathcal{B}(B^0 \to J/\psi\,K^0_{\mathrm{S}})} \times \frac{\mathcal{B}(\Lambda \to p\pi^-)}{\mathcal{B}(K^0_{\mathrm{S}} \to \pi^+\pi^-)} \times \frac{\varepsilon_{J/\psi\,\Lambda}(p_{\mathrm{T}})}{\varepsilon_{J/\psi\,K^0_{\mathrm{S}}}(p_{\mathrm{T}})}\,, \tag{5.1}$$

Furthermore, the following branching fraction inputs are used from the PDG [51]:

- $\mathcal{B}(B^0 \to J/\psi K^0_S) = (4.45 \pm 0.12) \times 10^{-4}$
- $\mathcal{B}(\Lambda \to p\pi) = (64.1 \pm 0.5)\%$
- $\mathcal{B}(K^0_{\mathrm{S}} \to \pi^+\pi^-) = (69.20 \pm 0.05)\%$

The ratio of efficiency corrected yields is shown in Fig. 5.10 in bins of the b-hadron p_T, showing good agreement between the downstream and long track categories. The $\mathcal{B}(\Lambda_b^0 \to J/\psi\,\Lambda)$ is extracted by simultaneously fitting the downstream and long reconstructed Λ (K^0_{S}) category distributions with the $f_{\Lambda_b^0}/f_d$ function, defined as

$$\frac{f_{\Lambda_b^0}}{f_d} = 2\frac{f_{\Lambda_b^0}}{f_u + f_d}(p_{\mathrm{T}}) = 2 \times A[p_1 + \exp(p_2 + p_3 p_{\mathrm{T}})] \tag{5.2}$$

with $A = 1.000 \pm 0.061$, $p_1 = (7.93 \pm 1.41) \times 10^{-2}$, $p_2 = -1.022 \pm 0.047$ and $p_3 = -0.107 \pm 0.002\,\mathrm{GeV}^{-1}$, shown as the red dashed line in Fig. 5.10, using a Gaussian constraint on the $f_{\Lambda_b^0}/f_d$ shape and normalisation parameters, and only floating the branching fraction scale parameter. The resulting branching fraction is found to be

$$\mathcal{B}(\Lambda_b^0 \to J/\psi\,\Lambda) = (3.08 \pm 0.26) \cdot 10^{-4} \tag{5.3}$$

where the uncertainty is statistical, from the uncertainties in the input branching fractions and from the uncertainty on the $f_{\Lambda_b^0}/f_d$ shape and normalisation. Table 5.2 shows the obtained $\mathcal{B}(\Lambda_b^0 \to J/\psi\,\Lambda)$ values for the different years and Λ or K^0_{S} track categories, with the corresponding signal extraction fits shown in App. E. The results are in good agreement between the different years and track categories. The combined track category results are found to be lower than the individual track category results, which is

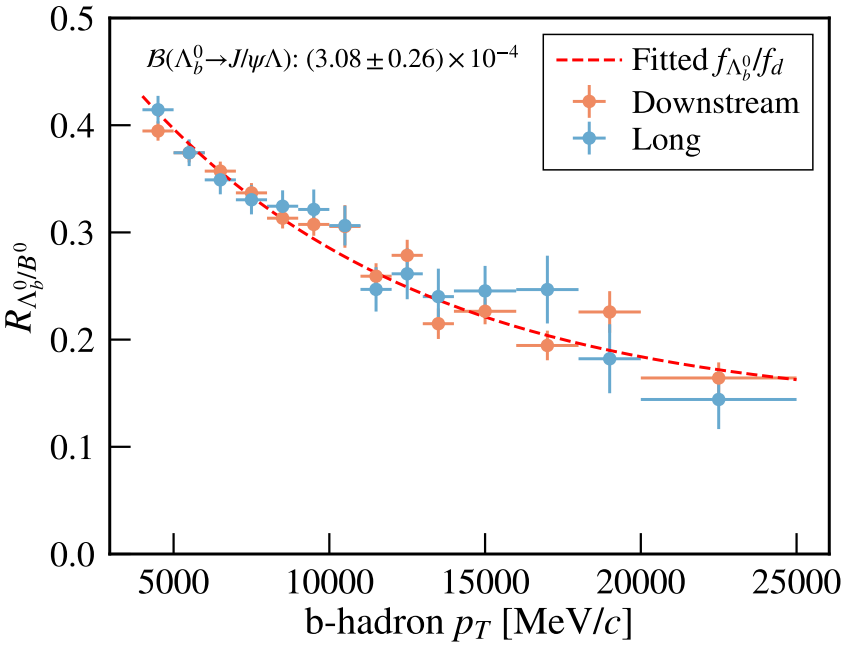

Figure 5.10: The measured $\Lambda_b^0 \to J/\psi(\to \mu^+\mu^-)\Lambda$/ $B^0 \to J/\psi(\to \mu^+\mu^-)K_S^0$ efficiency corrected yield ratio in bins of b-hadron p_T for the combined 2016, 2017 and 2018 dataset using downstream (red) and long (blue) reconstructed K_S^0 and Λ candidates.

caused by the fact that the extracted branching fraction not only depends on the normalisation but also on the shape of the fitted $f_{\Lambda_b^0}/f_d$. It is therefore not necessarily expected that the combined result is equal to the average of the individual results. It can also be seen that the measurement is dominated by the downstream track category, due to the larger number of candidates in this category.

Table 5.2: Obtained $\mathcal{B}(\Lambda_b^0 \to J/\psi\Lambda)$ values ($\times 10^{-4}$) for the different years and Λ or K_S^0 track categories.

Year	Combined	Downstream	Long
16	(3.08 ± 0.27)	(3.12 ± 0.28)	(3.17 ± 0.30)
17	(3.17 ± 0.28)	(3.17 ± 0.28)	(3.28 ± 0.32)
18	(3.28 ± 0.29)	(3.31 ± 0.30)	(3.32 ± 0.31)
16+17+18	(3.08 ± 0.26)	(3.09 ± 0.26)	(3.20 ± 0.29)

As the branching fraction extraction depends on the measured value of $f_{\Lambda_b^0}/f_d$, the uncertainty on this value is propagated to the final result. $f_{\Lambda_b^0}/f_d$ is known with a 7% precision [50], which is taken as the systematic uncertainty on the branching fraction. This is expected to be the largest systematic uncertainty on the final result. The other systematic uncertainties are discussed in the following section.

5.5 Systematic uncertainties

The systematic uncertainties are calculated by varying the different ingredients to the analysis and calculating the effect on the final result. These uncertainties are then added in quadrature to obtain the total systematic uncertainty. The size of the uncertainties is estimated by rerunning the fit for the branching fraction varying either the yields or the efficiency ratio for both the signal and normalisation mode, because some systematic effects cancel in the ratio.

5.5.1 Averaging of $f_{\Lambda_b^0}/f_d$

The value of $f_{\Lambda_b^0}/f_d$ is evaluated at the centre of each of the sub-bins. In reality, the weighted average position in p_T will be different from the centre. To estimate a systematic uncertainty due to this effect, the branching fraction is determined using $f_{\Lambda_b^0}/f_d$ evaluated at points in p_{T} that are off-center, at 1/3 and 2/3 relative to the bin width, and yields an uncertainty of 2%.

5.5.2 Likelihood mass fit shapes

A systematic uncertainty on the knowledge of the signal invariant mass fit shapes is estimated by replacing the Hypatia shape by a double-sided Crystal Ball function [66], consisting of a Gaussian core with two power law tails. For downstream-reconstructed signal candidates, the mis-ID background shape is changed from a Johnson shape to a double-sided Crystal Ball. A sub-1% effect on the result is assigned for the sum of these two systematic changes.

5.5.3 Statistical uncertainty on the simulated samples

The statistical uncertainty on the simulated MC samples is evaluated by varying the selection efficiency ratios within their uncertainties and re-evaluating the branching fraction calculation. This procedure is then repeated

100 times and the resulting RMS of the distribution of branching fractions is assigned as the systematic uncertainty. An effect of the order of 1-2% is assigned.

5.5.4 Downstream tracking efficiency

Unlike for long tracks, no tracking efficiency correction maps are available for downstream tracks. The tracking efficiency for long lived particles with downstream tracks has, however, been measured [74]. An overestimation of 1.4% was found for the tracking efficiency of downstream tracks using uncorrected simulation. This is therefore taken as an estimate for the systematic uncertainty on the downstream tracking efficiency.

5.5.5 Simulation correction

The effect of choice of the kinematic Gradient Boosting Reweighter simulation corrections is assessed by extracting an alternative set of kinematic corrections derived from the samples themselves. The total efficiency ratio is recomputed in bins of p_{T}, using the alternative kinematic weights. Its comparison with the efficiency obtained using the nominal weights is shown in Fig 5.11. The effect on the efficiency ratio is found to be small, with a maximum effect of 2.5% and an average of around 1%. Therefore, a 1% systematic uncertainty is assigned for the kinematic correction.

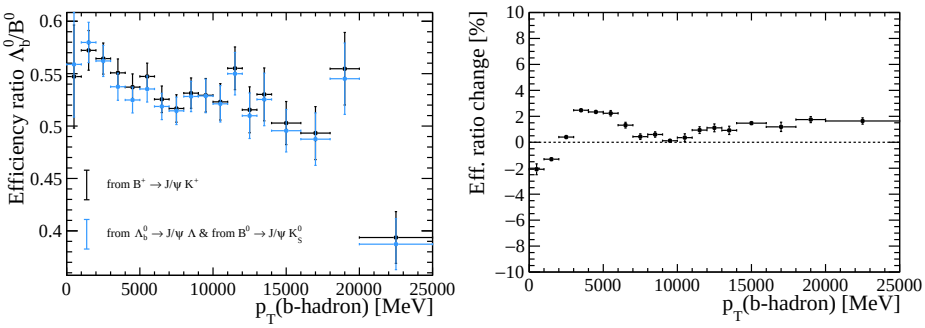

Figure 5.11: Left: efficiency ratio distribution in bins of b-hadron p_T for downstream reconstructed Λ (K_S^0) hadrons shown for 2017 simulation samples, using kinematic correction weights obtained from $B^+ \to J/\psi\,(\to \mu^+\mu^-)K^+$ decays (black) or directly from the signal and normalisation decays (blue). Right: relative change in efficiency ratio using the two different kinematic correction methods. A maximum effect of 2.5% can be seen, with an average of around 1%.

The uncertainty on the other simulation corrections (decay angles, PID, tracking) is estimated by varying the correction factors within their uncertainties and re-evaluating the efficiency ratio. This process is repeated 100 times and the resulting RMS of the distribution of efficiency ratios is assigned as the systematic uncertainty. The effect of the variations is shown in Fig. 5.12. The effect of the angular corrections is around 1%, the effect of the PID corrections is negligible, and the effect of the tracking correction factors is around 0.5%. A total systematic uncertainty of 1.5% is assigned for the simulation corrections.

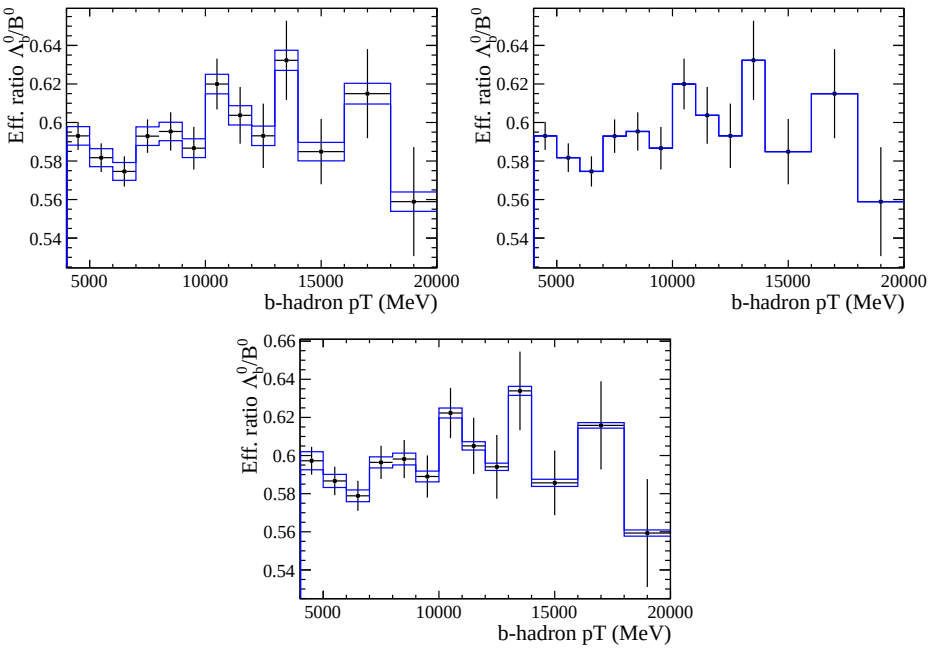

Figure 5.12: The nominal (black) and $\pm 1\sigma$ variation bands (blue) of the efficiency ratio distribution in bins of b-hadron p_T for long reconstructed Λ (K_S^0) hadrons, using the combined 2016, 2017 and 2018 data sample. The top left plot shows the effect of varying the angular corrections, the top right plot the effect of varying the PID corrections, and the bottom plot shows the effect of varying the tracking correction factors. The effect of the angular corrections is around 1%, the effect of the PID corrections is negligible, and the effect of the tracking corrections is around 0.5%.

5.5.6 Material interaction

An important systematic uncertainty on the efficiency is how well material interactions of Λ and K^0_S hadrons are modeled in the simulation. This modelling includes the distribution and amount of material as well as which cross-sections of Λ and K^0_S hadrons with material (mostly Al, Si and Be) are used. Any material interactions occurring beyond the requirement on the $z-$position of the end vertex will not affect the estimated rate; therefore, the long track data category depends on the material interactions in the VELO and the downstream data category on the material interactions in the RICH1 detector as well. To determine a systematic uncertainty on the description of material interactions, the uncertainty on the amount of detector material and the uncertainty on K^0_S and Λ cross-sections is taken into account.

Approximately 3% of Λ and K^0_S interact in the detector material before $z = 400\,\text{mm}$, as determined from simulation. These interactions take place in the VELO RF foil and in the VELO modules (see Fig. 5.13). A detailed model of these structures is present in the simulation, and the amount and position of the material is known to be a good approximation of the real detector [75]. The amount of material traversed by particles in the VELO is thought to be known with an uncertainty around 6% on X_0 [22]. For the downstream data category, in the simulation around 8.6% of Λ and 5.4% of K^0_S are found to interact before $z = 2250\,\text{mm}$. The interactions primarily happen in the VELO, RICH 1 and the interface between the VELO and RICH 1. The estimated uncertainty on the material budget for downstream reconstructed Λ and K^0_S used is around 10% to be conservative.

The effect of a difference in the Λ and K^0_S cross sections is most pronounced for the Λ, as the Λ interaction probability is found to differ between two `GEANT 4` versions by around 0.2% for the long track Λ candidates and 0.5% for downstream Λ candidates [37]. As such, the effect from material interactions is estimated to be 0.3% for the long tracks and 0.6% for the downstream tracks. This systematic is assigned as a uniform systematic uncertainty on the estimated branching fraction.

5.5.7 Total uncertainty

Table 5.3 summarises all the uncertainties on the $\mathcal{B}(\Lambda_b^0 \to J/\psi\,\Lambda)$ measurement. The total uncertainty is estimated to be 10%, with the largest contribution coming from the systematic uncertainty on the $f_{\Lambda_b^0}/f_d$ shape and normalisation. The measurement is therefore systematically limited, and not by the available data sample size.

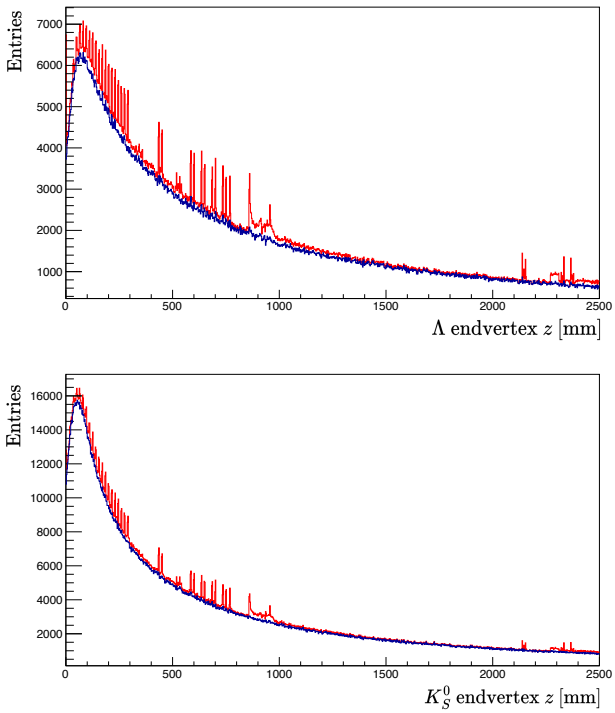

Figure 5.13: The endvertex z location (in mm) for Λ from $\Lambda_b^0 \to J/\psi\,\Lambda$ (top) and K_S^0 from $B^0 \to J/\psi(\to \mu^+\mu^-)K_S^0$ (bottom) in 2016 simulation samples. The red distribution shows all candidates, while the blue shows those that decayed. The red spikes correspond to hadronic interactions in detector material. For example, the red spikes between 0 and 300mm correspond to the VELO modules.

5.6 Discussion and Outlook

This chapter presented the measurement of the $\Lambda_b^0 \to J/\psi\,\Lambda$ branching fraction, using the combined 2016, 2017 and 2018 data. The branching fraction is measured to be

$$\mathcal{B}(\Lambda_b^0 \to J/\psi\,\Lambda) = (3.08 \pm 0.26 \pm 0.12) \cdot 10^{-4}, \tag{5.4}$$

with the first comes from the uncertainty from available statistics, from the input branching fractions and the $f_{\Lambda_b^0}/f_d$ shape and normalisation, and the second from the remaining systematic uncertainties. The main systematic uncertainty is expected to be the uncertainty on $f_{\Lambda_b^0}/f_d$, which is currently 7%, and already included in the presented measurement.

Table 5.3: Summary of uncertainties on the $\mathcal{B}(\Lambda_b^0 \to J/\psi\,\Lambda)$ measurement.

Source	Uncertainty
Fit	
Statistical	4%
$f_{\Lambda_b^0}/f_d$ shape & norm.	7%
Input branching fractions	3%
Systematics	
Averaging of $f_{\Lambda_b^0}/f_d$	2%
Fit mass shapes	1%
Statistical uncertainty on MC	2%
Downstream tracking efficiency	1.4%
Kinematic correction	1%
Simulation corrections	1.5%
Material interaction	0.6%
Total	10%

The measured value is in agreement with multiple theoretical predictions [76–78] and also with the previous D0 measurement $\mathcal{B}(\Lambda_b^0 \to J/\psi\Lambda) = (3.7 \pm 1.0) \cdot 10^{-4}$ [48]. This new measurement is the world's most accurate measurement of $\mathcal{B}(\Lambda_b^0 \to J/\psi\,\Lambda)$ with a factor of three better precision than the previous measurement and the current world average [51]. The improved precision on the branching ratio is important for the rare mode branching ratio measurement, as it is used as a normalisation channel. As shown in the measured q^2 distribution in Fig. 4.1, over half of the uncertainty, shown as the outer error bars, originates from the uncertainty on the $\Lambda_b^0 \to J/\psi\,\Lambda$ branching fraction. With this new, improved measurement, this uncertainty will largely disappear, and the precision on the rare mode branching ratio is expected to improve significantly.

As the measurement is limited by systematic uncertainties (mostly coming from the knowledge of $f_{\Lambda_b^0}/f_d$), the precision of the $f_{\Lambda_b^0}/f_d$ measurement will need to be improved to further improve the precision on $\mathcal{B}(\Lambda_b^0 \to J/\psi\,\Lambda)$. Repeating this measurement with more data, for example using the expected LHCb Run 3 data, will therefore not improve its precision significantly. The result does allow LHCb to measure different b-baryon decays, e.g. rare Ξ_b and Ω_b^- decays, using $\Lambda_b^0 \to J/\psi\,\Lambda$ as a normalisation channel. With the expected increase in data size in Run 3, more rare bottom-baryon decays will be accessible, allowing the further exploration of the flavour anomalies in the baryonic sector.

The analysis also provides a valuable experimental crosscheck by measuring the branching fraction both using K_S^0 and Λ hadrons reconstructed with downstream and long tracks. Both data categories agree with each other, indicating a good understanding of the detector and the selection efficiencies. This is important to know for the rare mode analysis, as it shows that the reconstruction of the long-lived hadrons is well understood. The rare mode R_Λ analysis is the topic of the next chapter.

6 The rare mode: towards a measurement of R_Λ

This chapter describes results towards the measurement of R_Λ, which tests lepton-flavour universality using $\Lambda_b^0 \to \Lambda \ell^+ \ell^-$ decays, with $\ell = e^\pm$ or $\mu^\pm$. The analysis is performed on the full LHCb dataset, which aims to be the first measurement of R_Λ as well as the first observation of the $\Lambda_b^0 \to \Lambda e^+ e^-$ decay process. The measurement provides an additional investigation into the flavour anomalies, and allows to test lepton flavour universality using baryonic decays instead of the more commonly studied mesonic modes. Compared to the previously studied baryonic decay $\Lambda_b^0 \to p K^- \ell^+ \ell^-$, the $\Lambda_b^0 \to \Lambda \ell^+ \ell^-$ decay has an accurate theoretical prediction on the LFU ratio due to the presence of the Λ resonance in the decay, which allows for a comparison of experimental results with theory. Firstly, the efficiencies are shown and discussed. Then, the invariant mass fits are presented. Subsequently, the results of the $\Lambda_b^0 \to J/\psi \Lambda$ and $\Lambda_b^0 \to \psi(2S)\Lambda$ normalisation mode crosschecks are shown and discussed. Finally, an outlook is given with (blinded) mass spectrum for the rare modes.

6.1 Efficiencies

The selection efficiencies for the $\Lambda_b^0 \to J/\psi \Lambda$ and $\Lambda_b^0 \to \psi(2S)\Lambda$ decays are calculated using the corrected MC simulation samples, as described in Sec. 4.6. The applied selection is similar to the selection in the resonant mode analysis, with the addition of the MVA requirement. The efficiencies are calculated for each data taking year per track type (long or downstream) and magnet polarity, and afterwards combined into a single efficiency per analysis category using weights corresponding to the relative data sample size. This results in an efficiency for Run 1, 2015+2016, and 2017+2018,

an example of which is shown in Tab. 6.1 and Tab. 6.2 for downstream reconstructed Λ candidates, all other tables are shown in App. C.2.

From the tables it can be seen that the efficiency for the electron mode decays is lower than for the muon mode decays. This is due to both a lower reconstruction efficiency for individual electron tracks compared to muons due to bremsstrahlung, as well as a lower trigger efficiency for electrons due to stricter p_T requirements. The efficiency for $\Lambda_b^0 \to \psi(2S)\Lambda$ decays is higher than for $\Lambda_b^0 \to J/\psi\,\Lambda$ decays, mostly due to the higher trigger efficiency. This can be explained by the fact that the $\Lambda_b^0 \to \psi(2S)\Lambda$ decays have a higher di-lepton invariant mass q^2, which results in a higher momentum of the resulting leptons, and are therefore more likely to pass the requirement on transverse momentum.

The Run 1 trigger efficiency is lower than the 2015+2016 and 2017+2018 trigger efficiency. This is caused by the lower beam energy in Run 1 ($3.5 - 4.0\,\text{TeV}$) compared to 2015+2016 and 2017+2018 ($6.5\,\text{TeV}$), which results in a lower momentum of the leptons and therefore a lower trigger efficiency. It can be observed that the stripping and reconstruction efficiency is the lowest out of all efficiencies. This is due to the acceptance of the hadron tracks, the reconstruction efficiency of the tracks and the selections applied during the stripping, as shown in App. B. Next to this, particles are lost due to interaction with detector material and can therefore not be reconstructed.

Table 6.1: Table showing the selection efficiencies for $\Lambda_b^0 \to J/\psi\,(\to e^+e^-)\Lambda$ decays in the J/ψ q^2 bin using downstream reconstructed Λ candidates for combined magnet polarity.

Categories	Weighted Efficiency (%)		
	Run 1	2015+2016	2017+2018
Generator	18.435 ± 0.038	19.748 ± 0.051	19.703 ± 0.052
Stripping + rec.	2.335 ± 0.017	2.051 ± 0.014	2.097 ± 0.012
Tracking corr.	95.922 ± 0.020	97.292 ± 0.020	98.210 ± 0.020
Pre-Selection	57.191 ± 0.402	63.940 ± 0.370	64.357 ± 0.307
Trigger	8.995 ± 0.261	23.467 ± 0.362	20.491 ± 0.289
PID	93.089 ± 0.020	82.086 ± 0.020	79.651 ± 0.020
MVA	48.720 ± 1.474	42.664 ± 0.873	42.184 ± 0.741
q^2 selection	98.165 ± 0.469	97.946 ± 0.325	97.843 ± 0.292
Total efficiency	0.00949 ± 0.00041	0.02017 ± 0.00053	0.01760 ± 0.00041

Table 6.2: Table showing the selection efficiencies for $\Lambda_b^0 \to J/\psi\,(\to \mu^+\mu^-)\Lambda$ decays in the J/ψ q^2 bin using downstream reconstructed Λ candidates for combined magnet polarity. Note that the efficiencies are similar to the efficiencies obtained in the $\mathcal{B}(\Lambda_b^0 \to J/\psi\,\Lambda)$ analysis, apart from the added MVA requirement.

Categories	Weighted Efficiency (%)		
	Run 1	2015+2016	2017+2018
Generator	18.576 ± 0.039	19.839 ± 0.052	19.780 ± 0.052
Stripping + rec.	3.904 ± 0.022	3.604 ± 0.018	3.698 ± 0.015
Tracking corr.	100.963 ± 0.020	97.973 ± 0.020	98.662 ± 0.020
Pre-Selection	65.632 ± 0.301	65.309 ± 0.277	66.203 ± 0.228
Trigger	36.629 ± 0.365	49.930 ± 0.349	56.914 ± 0.296
PID	95.288 ± 0.020	94.040 ± 0.020	94.767 ± 0.020
MVA	44.421 ± 0.601	47.216 ± 0.496	44.056 ± 0.367
q^2 selection	96.551 ± 0.312	96.168 ± 0.261	96.080 ± 0.204
Total efficiency	0.07154 ± 0.00137	0.09678 ± 0.00142	0.10907 ± 0.00133

6.2 Control mode mass fits

The control mode yields are extracted from the maximum-likelihood invariant fits to the invariant mass distributions of the $\Lambda_b^0 \to J/\psi\,\Lambda$ and $\Lambda_b^0 \to \psi(2S)\Lambda$ decays, as described in Sec 4.7. The fits consist of different components, similar to the fits performed for the resonant mode analysis (see Chap. 5) but with small differences. The following fit components are included with floating fit yields:

- **Signal:** The signal component is modelled by a double-sided Crystal Ball function [66]. All parameters are fixed from MC simulation, except the mean μ and width σ. For the electron mode, the signal shape is obtained separately for the number of recovered bremsstrahlung photons: 0, 1, or 2. The total shape on data is then combined by fixing the expected fractions of the number of recovered bremsstrahlung photons obtained from data.

- **Mis-ID:** The mis-identified background component, describing the candidates where a pion from a $B^0 \to J/\psi\,K^0_S$ or $B^0 \to \psi(2S)K^0_S$ decay is misidentified as a proton. The background is modelled using a Johnson S_U distribution [67], where all parameters are fixed from MC simulation.

- **Λ(1520)**: The partially reconstructed background component, coming from $\Lambda_b^0 \to J/\psi\,\Lambda(1520)$ or $\Lambda_b^0 \to \psi(2S)\Lambda(1520)$ decays, where the $\Lambda(1520)$ decays to a Λ and a pion. The pion has a low momentum and is not reconstructed, leading to the same final state as the decays of interest. The background is modelled with a Gaussian kernel density estimation [79] with the shape fixed from simulation.

- **Combinatorial background:** The combinatorial background is modelled by an exponential function. The shape is not taken from MC simulation, but fitted directly on the data.

The partially reconstructed $\Xi_b \to J/\psi\,\Xi$, where $\Xi \to \Lambda\pi$ where the pion is not reconstructed, component used in the resonant mode analysis is not included for the fits in the downstream reconstructed Λ hadron data category. However the expected contribution is small, as for the resonant mode analysis the obtained signal yield with and without the $\Xi_b \to J/\psi\,\Xi$ component changed less than 1%, and therefore has a negligible impact on the signal yields. The fits are performed on the Run 1, 2015+2016, and 2017+2018 data samples. Fig. 6.1 until 6.4 show the invariant mass fits on

MC simulation for the $\Lambda_b^0 \to \psi(2S)\Lambda$ and $\Lambda_b^0 \to J/\psi\,\Lambda$ decays, respectively, using the 2017+2018 sample with downstream reconstructed Λ candidates. The obtained shape parameters are then used to fit the invariant mass distributions on the corresponding data samples. Note the different fit ranges used for the electron and muon modes.

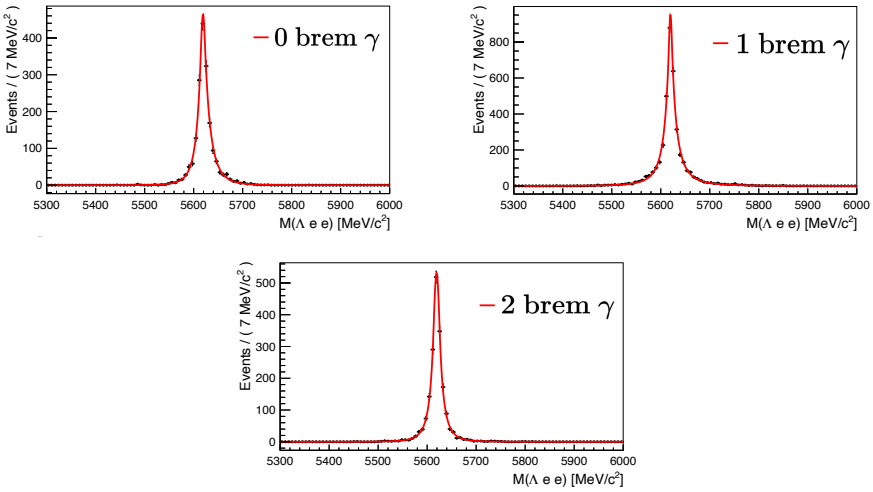

Figure 6.1: Invariant mass likelihood fits on MC simulation for signal without bremsstrahlung recovery (top left), with one bremsstrahlung recovered electron (top right), both bremsstrahlung recovered electrons (bottom) for the $\Lambda_b^0 \to \psi(2S)(\to e^+e^-)\Lambda$ decay in the combined 2017 and 2018 samples using downstream reconstructed Λ hadrons.

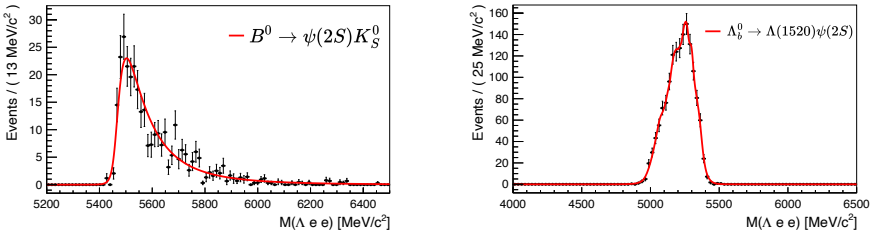

Figure 6.2: Invariant mass likelihood fits on MC simulation for the misidentified $B^0 \to \psi(2S)K^0_S$ decays and partially reconstructed $\Lambda_b^0 \to \psi(2S)\Lambda(1520)$ background (right) for the $\Lambda_b^0 \to \psi(2S)(\to e^+e^-)\Lambda$ decay in the combined 2017 and 2018 samples using downstream reconstructed Λ hadrons.

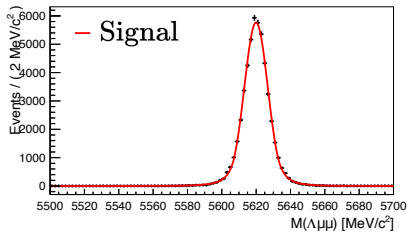

Figure 6.3: Invariant mass likelihood fits on MC simulation for signal for the $\Lambda_b^0 \to J/\psi(\to \mu^+\mu^-)\Lambda$ decay in the combined 2017 and 2018 samples using downstream reconstructed Λ hadrons.

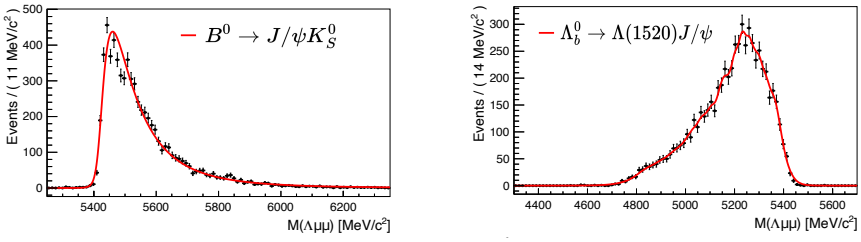

Figure 6.4: Invariant mass likelihood fits on MC simulation for the misidentified $B^0 \to J/\psi K_S^0$ decays (left) and partially reconstructed $\Lambda_b^0 \to J/\psi\,\Lambda(1520)$ background (right) for the $\Lambda_b^0 \to J/\psi(\to \mu^+\mu^-)\Lambda$ decay in the combined 2017 and 2018 samples using downstream reconstructed Λ hadrons.

The invariant mass fit on the 2017+2018 data sample for the $\Lambda_b^0 \to J/\psi\,\Lambda$ and $\Lambda_b^0 \to \psi(2S)\Lambda$ decays are shown in Fig. 6.5 and 6.6, respectively, using downstream reconstructed Λ candidates. Tables with the obtained yields are shown in Tab. 6.3 and 6.4 for the $\Lambda_b^0 \to J/\psi\,\Lambda$ and $\Lambda_b^0 \to \psi(2S)\Lambda$ decays, respectively. All fit plots for the different data taking years and track types are shown in App. E.2. The electron modes have about 7 times lower event yields, due to the lower trigger and selection efficiency and therefore the dominating uncertainty comes from the electron modes. These results are the first observations of the $\Lambda_b^0 \to J/\psi(\to e^+e^-)\Lambda$ and $\Lambda_b^0 \to \psi(2S)(\to e^+e^-)\Lambda$ decays, with a significance combined from the different data categories of about 49σ and 15σ respectively. The yields are sufficient to perform a measurement of $r_{J/\psi}$, $r_{\psi(2S)}$ and $R_{\psi(2S)}$, as will be shown in the next section.

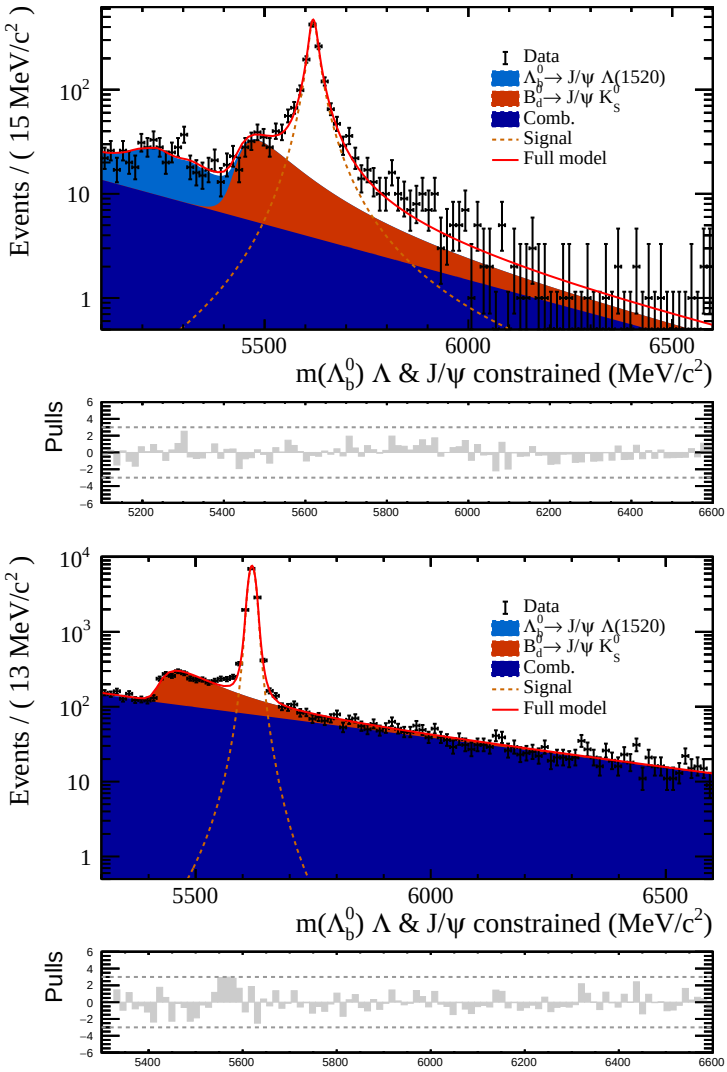

Figure 6.5: Maximum likelihood invariant mass fits for the $\Lambda_b^0 \to J/\psi(\to e^+e^-)\Lambda$ (top) and $\Lambda_b^0 \to J/\psi(\to \mu^+\mu^-)\Lambda$ (bottom) candidates using downstream reconstructed Λ candidates using the 2017+2018 data sample. The red line shows the total fit model, the orange dotted line the fitted signal, the dark blue filled area the combinatorial background, the red filled area the mis-identified background, and the light blue filled area the partially reconstructed background.

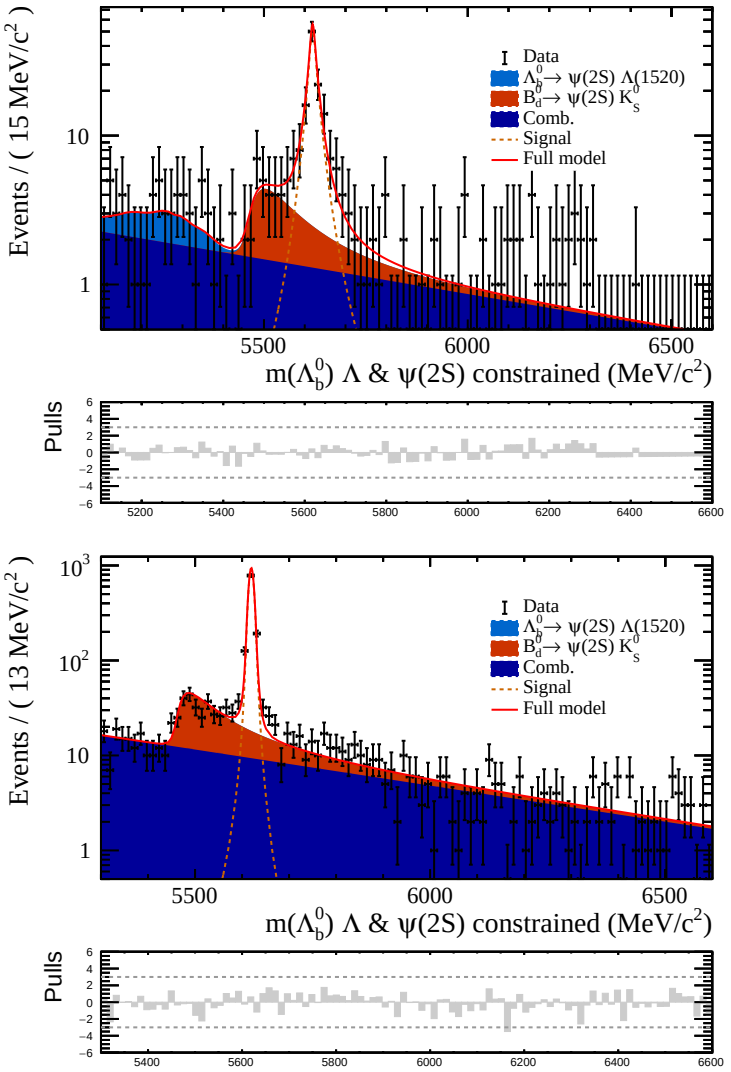

Figure 6.6: Maximum likelihood invariant mass fits for the $\Lambda_b^0 \to \psi(2S)(\to e^+e^-)\Lambda$ (top) and $\Lambda_b^0 \to \psi(2S)(\to \mu^+\mu^-)\Lambda$ (bottom) candidates using downstream reconstructed Λ candidates using the 2017+2018 data sample. The red line shows the total fit model, the orange dotted line the fitted signal, the dark blue filled area the combinatorial background, the red filled area the mis-identified background, and the light blue filled area the partially reconstructed background.

Table 6.3: Signal yields for $\Lambda_b^0 \to J/\psi(\to e^+e^-)\Lambda$ and $\Lambda_b^0 \to J/\psi(\to \mu^+\mu^-)\Lambda$ invariant mass fits, where DD and LL stand for the downstream- and long track reconstructed Λ and K_S^0 hadron data categories.

Period	$\Lambda_b^0 \to J/\psi(\to e^+e^-)\Lambda$		$\Lambda_b^0 \to J/\psi(\to \mu^+\mu^-)\Lambda$	
	DD	LL	DD	LL
Run 1	278 ± 21	269 ± 21	2481 ± 51	1775 ± 43
15+16	704 ± 33	488 ± 28	3883 ± 64	2345 ± 50
17+18	1350 ± 43	786 ± 36	8554 ± 95	4223 ± 67

Table 6.4: Signal yields for $\Lambda_b^0 \to \psi(2S)(\to e^+e^-)\Lambda$ and $\Lambda_b^0 \to \psi(2S)(\to \mu^+\mu^-)\Lambda$ invariant mass fits, where DD and LL stand for the downstream- and long track reconstructed Λ and K_S^0 hadron data categories.

Period	$\Lambda_b^0 \to \psi(2S)(\to e^+e^-)\Lambda$		$\Lambda_b^0 \to \psi(2S)(\to \mu^+\mu^-)\Lambda$	
	DD	LL	DD	LL
Run 1	20 ± 5	21 ± 6	270 ± 17	183 ± 14
15+16	48 ± 9	38 ± 7	331 ± 19	245 ± 16
17+18	118 ± 12	76 ± 11	795 ± 29	484 ± 22

6.3 $r_{J/\psi}$, $r_{\psi(2S)}$ and $R_{\psi(2S)}$

The ratios $r_{J/\psi}$, $r_{\psi(2S)}$ and $R_{\psi(2S)}$ are defined for the resonant mode $\Lambda_b^0 \to J/\psi\,\Lambda$ and $\Lambda_b^0 \to \psi(2S)\Lambda$ decays, as

$$r_{J/\psi} = \frac{N_{\Lambda_b^0 \to J/\psi\,(\to\mu^+\mu^-)\Lambda}}{N_{\Lambda_b^0 \to J/\psi\,(\to e^+e^-)\Lambda}} \times \frac{\varepsilon_{\Lambda_b^0 \to J/\psi\,(\to e^+e^-)\Lambda}}{\varepsilon_{\Lambda_b^0 \to J/\psi\,(\to\mu^+\mu^-)\Lambda}}, \tag{6.1}$$

$$r_{\psi(2S)} = \frac{N_{\Lambda_b^0 \to \psi(2S)(\to\mu^+\mu^-)\Lambda}}{N_{\Lambda_b^0 \to \psi(2S)(\to e^+e^-)\Lambda}} \times \frac{\varepsilon_{\Lambda_b^0 \to \psi(2S)(\to e^+e^-)\Lambda}}{\varepsilon_{\Lambda_b^0 \to \psi(2S)(\to\mu^+\mu^-)\Lambda}}, \tag{6.2}$$

and

$$\begin{aligned} R_{\psi(2S)} = & \frac{N_{\Lambda_b^0 \to \psi(2S)(\to\mu^+\mu^-)\Lambda}}{N_{\Lambda_b^0 \to \psi(2S)(\to e^+e^-)\Lambda}} \times \frac{\varepsilon_{\Lambda_b^0 \to \psi(2S)(\to e^+e^-)\Lambda}}{\varepsilon_{\Lambda_b^0 \to \psi(2S)(\to\mu^+\mu^-)\Lambda}} \times \\ & \frac{N_{\Lambda_b^0 \to J/\psi\,(\to e^+e^-)\Lambda}}{N_{\Lambda_b^0 \to J/\psi\,(\to\mu^+\mu^-)\Lambda}} \times \frac{\varepsilon_{\Lambda_b^0 \to J/\psi\,(\to\mu^+\mu^-)\Lambda}}{\varepsilon_{\Lambda_b^0 \to J/\psi\,(\to e^+e^-)\Lambda}} \end{aligned} \tag{6.3}$$

respectively. These modes serve as a calibration for the LFU ratio R_Λ of the rare modes. The double ratio $R_{\psi(2S)}$ allows for the cancellation of systematic uncertainties, while this is not the case for the single ratios $r_{J/\psi}$ and $r_{\psi(2S)}$. Together, these ratios provide a powerful crosscheck of the analysis. If the single ratios agree with their Standard Model prediction of 1, it shows that the absolute efficiencies from the corrected MC are well understood and applicable to data. The double ratio $R_{\psi(2S)}$ provides an extra crosscheck by validating that the relative selection efficiencies are correct at a higher q^2 value. This is important as most signal events are expected in the high q^2 region. It is beneficial to measure the inverse ratios, $r^{-1}_{J/\psi}$, $r^{-1}_{\psi(2S)}$ and $R^{-1}_{\psi(2S)}$, as their uncertainty represents a Gaussian distribution due to the low yield of the electron decay modes in the numerator.

The ratios are measured per data period in the downstream and long track categories separately. The single ratios $r^{-1}_{J/\psi}$ and $r^{-1}_{\psi(2S)}$ are measured as a single integrated value. Fig. 6.7 shows the measured ratios for the different data taking periods and track types. Both the $r^{-1}_{J/\psi}$ and $r^{-1}_{\psi(2S)}$ single ratios are below the expected value of 1, except in the combined 2017 and 2018 downstream category. The double ratio $R^{-1}_{\psi(2S)}$, however, agrees within uncertainty with the expected value in all categories, showing the power of the double ratio method. The uncertainties on the ratios are large, caused by the low signal yields of the electron modes, especially for the $\Lambda_b^0 \to \psi(2S)(\to e^+e^-)\Lambda$ decays.

The ratios seem to be consistently below 1, indicating either an underestimation of the efficiency-corrected electron yield, or an overestimation of the efficiency-corrected muon yield. The latter is unlikely, as the muon reconstruction is carefully studied with large samples of prompt J/ψ candidates, and do not suffer from energy loss through bremsstrahlung. The most likely explanation is that the efficiencies for the electron modes are not well understood. To verify this, the ratios can be measured in bins of kinematic variables to verify that the discrepancy is uniform in the phase space. This is, however, not possible right now due to the low signal yield of the electron modes, as binning the sample would further reduce the number of events per invariant mass fit.

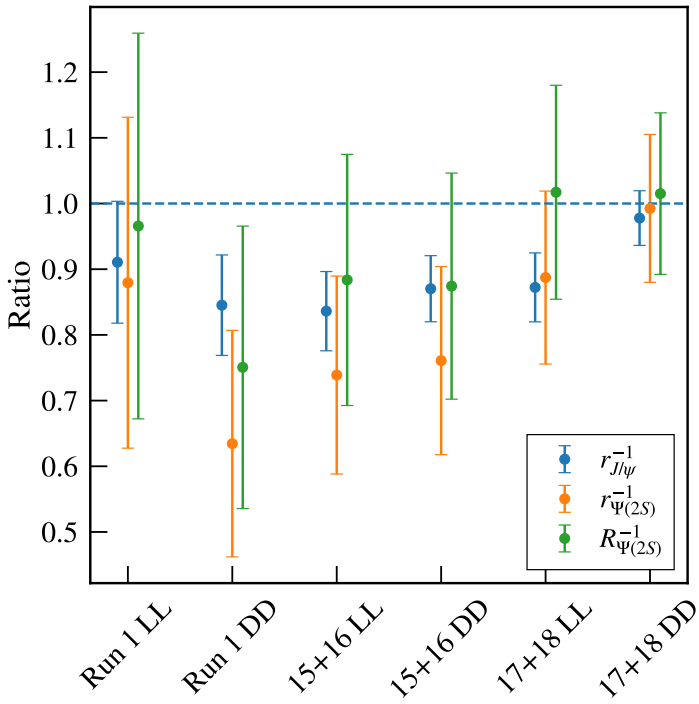

Figure 6.7: The inverse $r_{J/\psi}$, $r_{\psi(2S)}$ and $R_{\psi(2S)}$ ratios for the different data categories. The single ratios are below the expected value, while the double ratio agrees with 1.

6.4 Towards the rare modes

The measurement of the rare mode yields is challenging, especially for the $\Lambda_b^0 \to \Lambda e^+ e^-$ decay. Assuming similar reconstruction efficiencies, the yield of the $\Lambda_b^0 \to \Lambda e^+ e^-$ decay is estimated using the obtained $\Lambda_b^0 \to \psi(2S)(\to e^+e^-)\Lambda$ yields. The measured branching ratio of the $\Lambda_b^0 \to \Lambda \mu^+ \mu^-$ decay, which assuming lepton flavour universality is the same as the $\Lambda_b^0 \to \Lambda e^+ e^-$ branching ratio, is about a factor 10 lower than the combined $\Lambda_b^0 \to \psi(2S)\Lambda$ and $\psi(2S)(\to e^+e^-)$ decay rate [51]. Scaling the $\Lambda_b^0 \to \psi(2S)(\to e^+e^-)\Lambda$ yield by a factor 10 results in a total combined yield in all analysis categories of about 20 events. In the individual categories, the expected yield is as low as 2 events. The data categories should thus be combined into a single (or simultaneous) invariant mass fit, which will improve the sensitivity and stability of the likelihood fit.

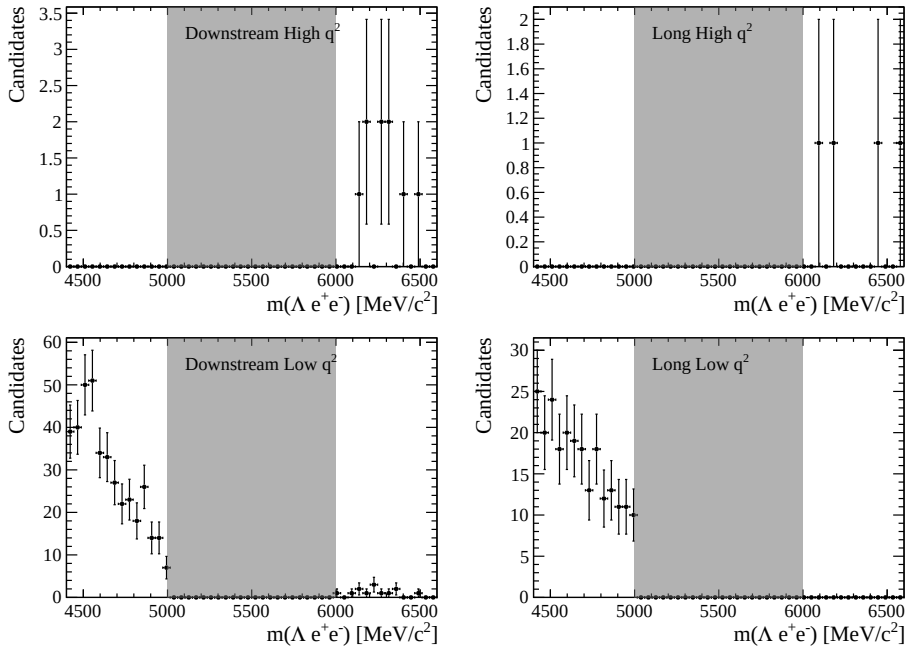

Figure 6.8: Invariant mass distributions for the rare $\Lambda_b^0 \to \Lambda e^+ e^-$ decays using the full Run 2 dataset, with a blinding region of $5000 - 6000\,\mathrm{MeV}/c^2$ shown in grey, in the high (top) and low (bottom) q^2 regions using downstream (left) and long-track (right) reconstructed Λ candidates.

A first look at the (blinded) rare mode invariant mass distributions after

the full event selection using the full Run 2 dataset is shown in Fig. 6.8 and 6.9. The figures show the invariant mass distributions for the rare $\Lambda_b^0 \to \Lambda e^+ e^-$ and $\Lambda_b^0 \to \Lambda \mu^+ \mu^-$ decays in the high $q^2 > 15\,\mathrm{GeV}^2/c^4$ region and the low $0.1 < q^2 < 6.0\,\mathrm{GeV}^2/c^4$ q^2 regions, where the $\Lambda_b^0 \to \Lambda e^+ e^-$ distributions are blinded in the signal mass region of $5000 - 6000\,\mathrm{MeV}/c^2$. Most of the signal is expected in the high q^2 region, which is visible in the $\Lambda_b^0 \to \Lambda \mu^+ \mu^-$ distributions for low q^2, see Fig 6.9. The blinded $\Lambda_b^0 \to \Lambda e^+ e^-$ distributions also confirm the low expected yield calculated before, as almost no background events are visible in the downstream data category. This could mean that the MVA is currently optimised with a too strict selection, removing almost all background and signal events. The $\Lambda_b^0 \to \Lambda \mu^+ \mu^-$ distributions show a clear signal peak.

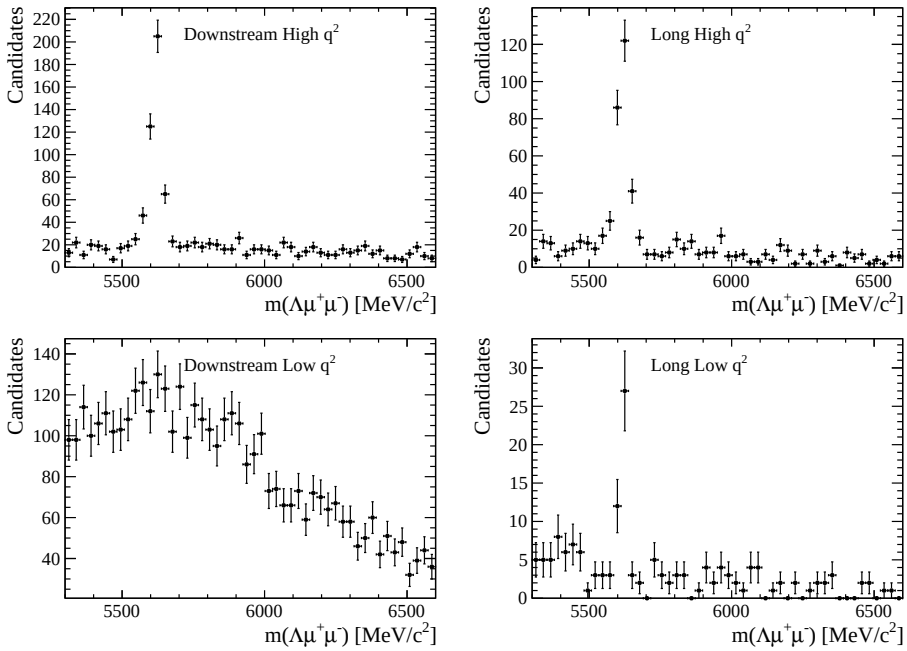

Figure 6.9: Invariant mass distributions for the rare $\Lambda_b^0 \to \Lambda \mu^+ \mu^-$ decays using the full Run 2 dataset in the high (top) and low (bottom) q^2 regions using downstream (left) and long-track (right) reconstructed Λ candidates.

Furthermore, as described in the previous section, the disagreement of the single ratios $r_{J/\psi}^{-1}$ and $r_{\psi(2S)}^{-1}$ seems too large to be contributed to statistical fluctuations. The downwards shift seen in the ratios most likely originates from incorrect electron mode selection efficiencies. This could be done by

measuring the ratios at different selection steps or in steps of the simulation correction procedure. When more data becomes available in Run 3, the ratios could also be measured in bins of kinematic variables.

The systematic uncertainties are expected to be similar to the resonant mode analysis, as the analysis strategy is very similar. The systematic uncertainties are expected to be negligible compared to the statistical uncertainties. In addition, this measurement is not affected by the uncertainties on $f_{\Lambda_b^0}/f_d$.

The results presented in this chapter show that the analysis is promising and likely leads to the first observation of the $\Lambda_b^0 \to \Lambda e^+ e^-$ decay and the first measurement of R_Λ.

7 The SciFi Tracker: a new tracking detector for LHCb

As the previous analyses chapters indicated, more data is needed to further study the flavour anomalies in the baryonic sector. During the long-shutdown of the LHC in 2018-2022, the LHCb detector underwent a major upgrade to increase the data collection rate and the detector performance. The Run 3 upgrade of the LHCb detector is the main topic of this chapter, and more specifically the SciFi tracker which replaced the IT and OT detector systems.

7.1 LHCb Upgrade

The LHCb detector has in recent years undergone an upgrade [80], such that data can be recorded without a hardware trigger and with an instantaneous luminosity approximately ten times higher than the luminosity the original LHCb detector was designed for. To handle the increase in data collection rate and the higher event multiplicities coming from the increase in instantaneous luminosity, several of the subdetectors and all the readout electronics have been replaced in the shutdown 2018-2022. The combination of the detector upgrades and increase in luminosity will allow LHCb to increase its precision on physics observables. The full tracking system, including the VELO, TT, and the T-station tracking stations, have all been replaced. A schematic drawing of the LHCb Upgrade detector is shown in Fig. 7.1. Although the schematic looks similar to Fig. 3.2, major changes have occurred.

These replacements include changes in technology used for: the VELO silicon strip detector are replaced by a silicon pixel detector, for the TT the replacement of the TT tracking station with the silicon-strip Upstream Tracker (UT), and for the Inner Tracker (IT) and the Outer Tracker (OT)

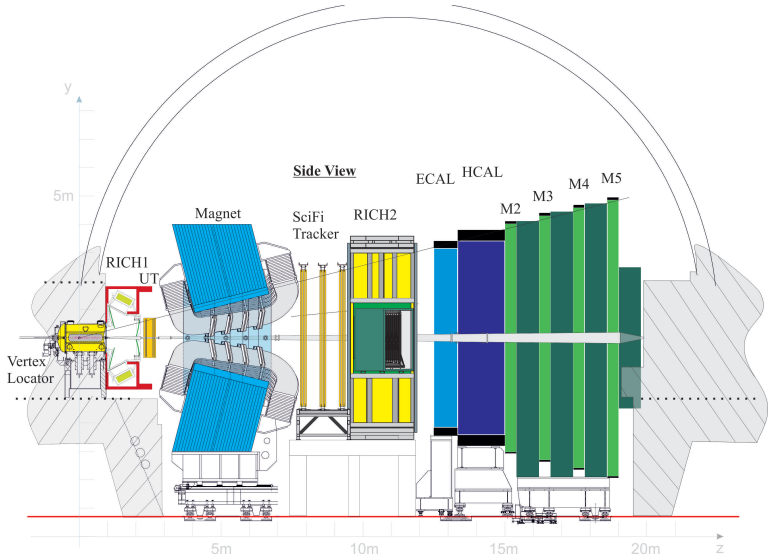

Figure 7.1: Schematic drawing of the LHCb Upgrade side view, showing the new subdetector systems [80].

with the Scintillating Fibre tracker (SciFi).

The SciFi tracker is the main topic of this chapter and will be described in more detail in the next section. The ECAL, HCAL, and Muon stations have undergone upgrades of their readout electronics, while the detectors mostly remained unchanged. The photodetectors and the mirrors of the RICH systems have also been replaced. The hardware L0 trigger has been removed, and replaced with a full online event reconstruction done at 40 MHz rate, implemented on a combination of a GPU and CPU farm.

7.2 SciFi Tracker

The SciFi Tracker has replaced the IT and OT tracking stations T1-T3 during the LHCb upgrade. The OT consisted of straw tubes with 5 mm diameters, whereas the SciFi has a higher channel granularity of 250 µm channel widths, to cope with the higher particle multiplicities. The SciFi tracker follows a similar design as the previous IT and OT trackers, and consists of three stations labeled, consistently with the previous trackers, T1-T3, each consisting of four detection layers [81]. The layers again follow the x-u-v-x geometry along the beam axis, with the two middle layers of fibres being angled at an $+5°$ and $-5°$ angle with respect to the vertical

$y-$axis. A schematic view of a SciFi station is shown in Fig. 7.2.

Each of the detector modules consist of eight fibre mats, which are read out using silicon photomultipliers (SiPMs) located on the bottom and top of the detector in so-called readout boxes (ROBs), where each SiPM has 128 channels. Each ROB in turn consists of two independent, identical, halves called half-ROBs, which will be further explained in Sec. 7.3. SciFi detector element locations are named from largest to the smallest element [82], following the LHCb coordinate system [83]. This naming scheme is used for the detector geometry and detector readout, and will be used throughout this thesis. A schematic figure of the SciFi naming scheme is shown in Fig. 7.3.

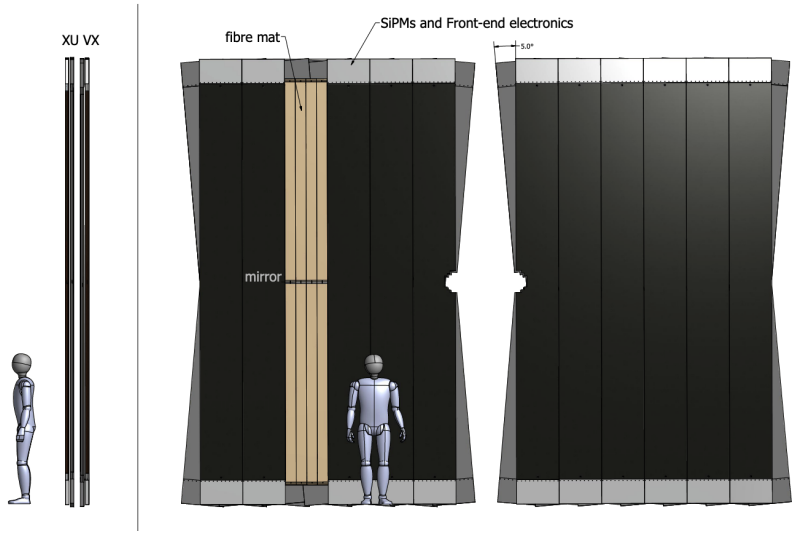

Figure 7.2: Illustration of the SciFi tracker T3 station with side (left) and front (right) view using a 1.86m tall dummy for scale [81].

- **Stations:** T1-T3. Station numbering starts at 1 due to historical reasons.
- **Layers:** L0-L3. Increasing numbering following the z axis.
- **Quarter:** Q0-Q3. Quarter numbering starts at negative x and y, first increasing in x and then in y.
- **Modules:** M0-M5. M0 is the closest module to the beam pipe, increasing from there. T1 only goes up to M4.

- **Mats:** Mat0-Mat3. The mats within a ROB are numbered left to right for the ROB on top of the module.
- **SiPM:** S0-S3. The SiPM numbering follows the same direction as the mats.
- **Channels:** C0-C127. The numbering for the SiPM channels follows the same direction as for the SiPMs themselves.

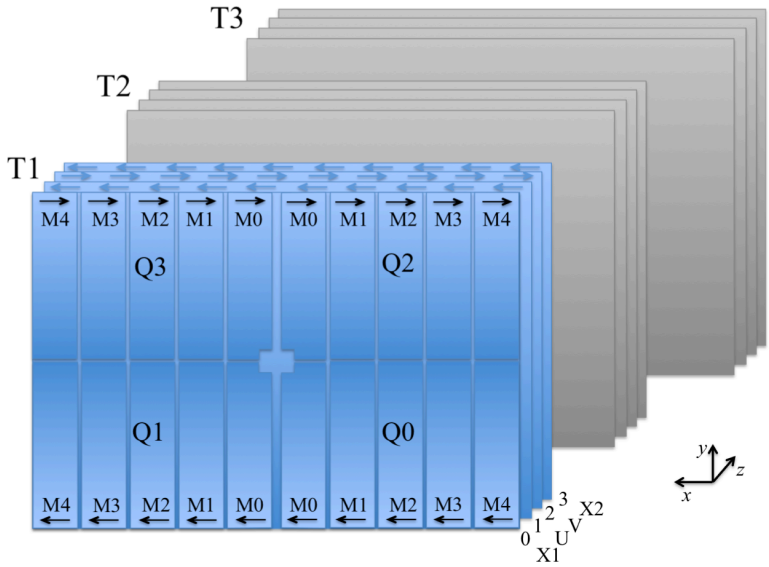

Figure 7.3: Schematic drawing of the SciFi naming scheme [82]. The arrows indicate the direction of the SiPM and channel numbering within a readout box.

When charged particles traverse the SciFi detector, they ionise and excite atoms in the scintillating fibres. Following a complex mechanism, the energy loss of the traversing particle is transformed into photons produced in the scintillating material. The photons then travel through the fibres to the SiPMs, where they are converted into an electrical signal. Therefore, the amplitude of the recorded electrical signal corresponds directly to the number of photons generated inside the detector, and thus to the amount of energy deposited by the traversing charged particle. A schematic drawing of this process is shown in Fig. 7.4.

To suppress hits from noise, thresholds are set on the number of photons measured in a SiPM channel. These thresholds are called t_1, t_2, t_3, and

currently correspond to 1.5, 2.5, and 4.5 photoelectrons [84]. t_1 is used to suppress hits from noise, while t_2 and t_3 are used in the clustering algorithm as will be explained in Sec. 7.5. From these SiPM signals, clusters are formed. A detailed description of the clustering algorithm is provided in Sec. 7.5. The measured clusters are subsequently combined to form tracks within the SciFi tracker, and combined with further tracking information from the VELO and UT subdetectors into long and downstream tracks.

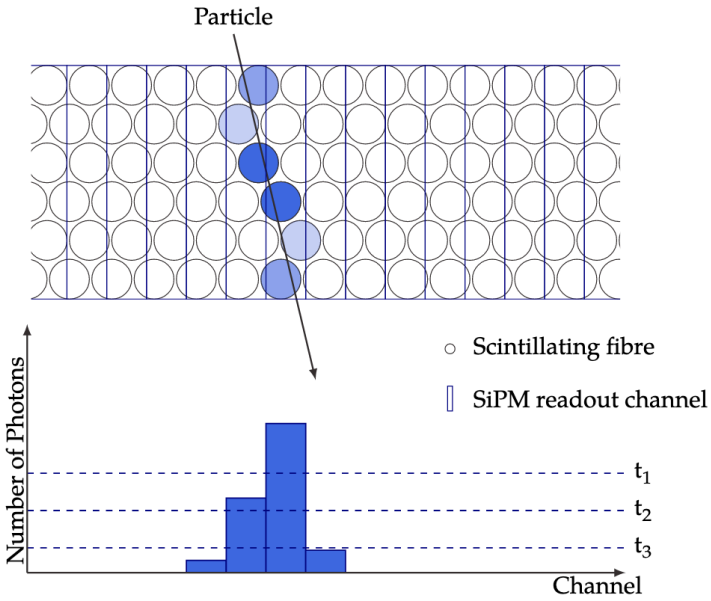

Figure 7.4: Schematic drawing of a charged particle traversing the SciFi detector and generating light in the fibres [85]. Using three thresholds, t_1, t_2, t_3, noise is reduced and clusters are created. In the figure, the reached thresholds are indicated by the lighter or darker blue colour of the fibre.

7.3 Dataflow and DAQ

Sec. 7.5 further describes the SciFi clustering and decoding algorithms, however firstly it is important to understand the dataflow and the readout electronics of the SciFi detector. The electrical signals from the SiPMs are read out by the Front-End (FE) electronics, forming the interface between the detector and the experiment data-acquisition (DAQ) system, also known as the Back-End (BE) electronics. The following sections will give a brief

overview and description of the electronics involved to read out the detector signal.

7.3.1 Front-End electronics

The Front-End electronics process the raw signal originating from the SiPMs, and pass it to the Back-End DAQ system. The FE electronics are located in the half-ROBs located on the bottom (Q0 and Q1) and top (Q2 and Q3) of the SciFi modules. Each half-ROB consists of one Master Board, four Cluster Boards, and four PACIFIC boards, as shown in the block diagram in Fig. 7.5. The PACIFIC boards are connected to the SiPMs, and each contain four Application Specific Integrated Circuits (ASICs), which amplify, shape, and digitize the analogue SiPM signal. The resulting signal is then passed to the Cluster Boards, consisting of two Field Programmable Gate Arrays (FPGAs) that run the clustering algorithm on the digital signal. The clustered data from the FPGAs is subsequently sent to the Master Board, which sends the data to the BE DAQ system located at 200 m distance in the data center on the surface. The Master Board is also used for control of the underlying electronics, and setting the required readout clock values. The data is sent out through eight GigaBit Transceiver (GBTX) serialisers [86], which combine the parallel data streams from the FPGAs into a serial stream, and send it via four Versatile Twin Transmitter (VTTx) modules [87]. The data from each SiPM is transmitted through a single optical fibre, and thus one BE link corresponds to one SiPM. Due to the limited bandwidth rate, by default the FE electronics only send the FPGA-clustered data to the BE in the form of 9-bit clusters. This is also called zero-suppressed (ZS) data, meaning when no light is recorded, no data is transmitted. It is, however, possible to run in a special mode where in addition to the cluster data, also the raw 2-bit SiPM threshold values are transmitted. This is called non-zero-suppressed (NZS) data, and can be used e.g. to perform clustering crosschecks offline or to identify malfunctioning, individual SiPM channels.

7.3.2 Back-End electronics

The BE electronics process the incoming data stream from the FE electronics, and merge the data belonging to the same bunch crossing. This is done using PCI express (PCIe40) cards containing a FPGA, specially designed to handle the readout of LHCb at 40 MHz [90]. Depending on the firmware installed on the FPGA on the PCIe40 card, it can fulfill a different role in the data acquisition. So-called TELL40 cards are used to read the data

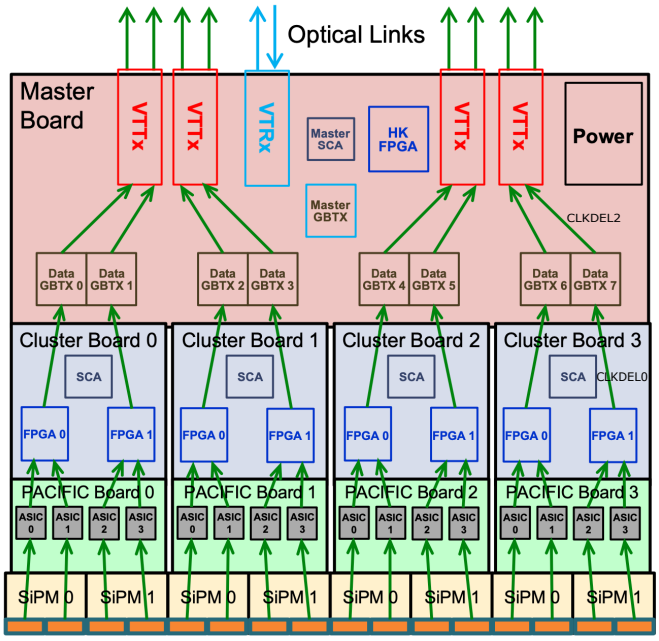

Figure 7.5: Block diagram of a SciFi FE half Read Out Box (ROB), showing the main components on each board [88, 89]. The green arrows denote the data stream, while the blue arrows show the bi-directional control links.

coming from the FE electronics, whereas SOL40 cards are used to control the FE boards, and the SODIN board is used to distribute the LHC clock to all the involved boards [91].

In the context of this thesis, the TELL40 type boards are of most interest, as they are responsible for processing the incoming cluster data from the FE electronics. The TELL40 boards receive the data from up to 48 incoming FE data links, split in two separate data streams of a maximum of 24 input links each. Within the SciFi tracker, two types of TELL40s are used. In the high occupancy region, where many detector hits are expected (i.e. the M0 modules close to the beampipe), a single 16-link high-occupancy TELL40 is used per quarter [92]. The rest of the detector (M1-M5) is read out using two 40-link low-occupancy TELL40s per quarter with 8 spare link connections. A schematic drawing of the connection between the FE electronics and the TELL40s is shown in Fig. 7.6. The high- and low-occupancy TELL40s differ in the amount of cluster objects that can be transmitted per bunch crossing. As more clusters are expected close to the beampipe, the high-occupancy

TELL40s use a different data format which can transmit up to 16 clusters, while in the low-occupancy region only up to 10 clusters can be sent, given that fewer clusters are expected, but more links are connected to the low occupancy TELL40. For a further details see Ref. [92]. The TELL40s combine the incoming data from the SiPMs into one data stream of so-called raw banks, add the corresponding bunch-crossing ID number, and send the raw banks to the LHCb high-level trigger system to be further processed, which is described in Sec. 7.5.

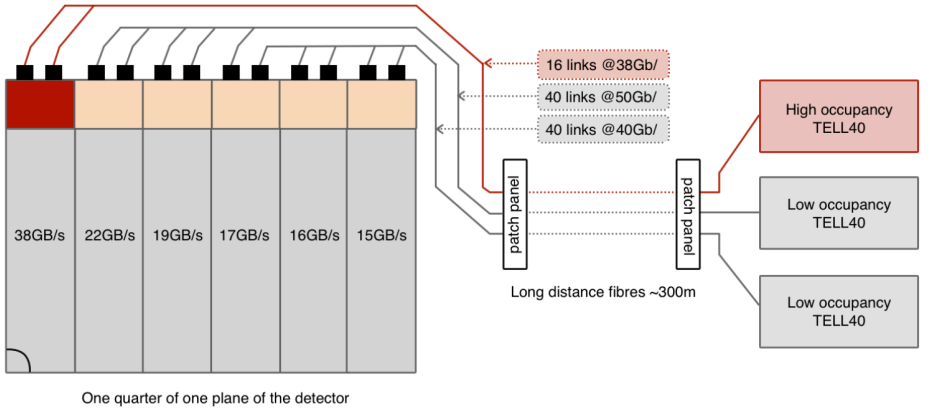

Figure 7.6: The TELL40 configuration for a single a SciFi detector quarter with estimated data bandwidth rate. Adapted from [92].

The TELL40 data is sent in 256-bit frames, starting with a 32-bit local header containing a 12-bit bunch-crossing ID. For increased processing performance, the TELL40 expands the 9-bit clusters originating from the FE boards into 16-bit cluster objects, where the 7 extra bits are filled with information containing the cluster's SiPM link position within its detector quarter [91]. The resulting 16-bit clusters are concatenated in ascending order of FE link number and if needed padded with zeroes to fill the last 256-bit frame. A schematic drawing of the TELL40 cluster data fragments is shown in Fig. 7.7.

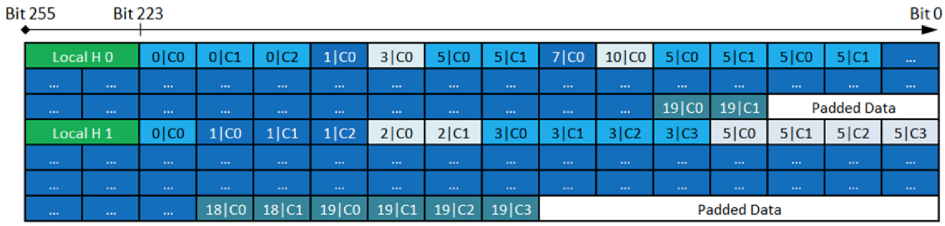

Figure 7.7: Schematic drawing of the cluster type data fragment, where 1|C0 signifies cluster 0 in link 1 [92]. The fragment consists of 16-bit clusters, preceded by a 32-bit Local Header containing the bunch-crossing ID and information about the data length. The variations in color identify the data belonging to individual links.

7.4 Timing Scans

To ensure stable data transmission within the SciFi front-end electronics, different clock settings in the electronics have to be synchronised. A schematic overview of the data flow and the different clocks in the front-end electronics is shown in Fig. 7.8. To ensure a stable data flow, so-called timing scans are performed. A timing scan consists of a large number of steps where each step corresponds to clock delays, with the different clocks and their names shown in Tab. 7.1. Per step the Bit Error Rate (BER) is recorded, and afterwards the error-free region is defined using analysis software, which is then used to determine the optimal clock settings.

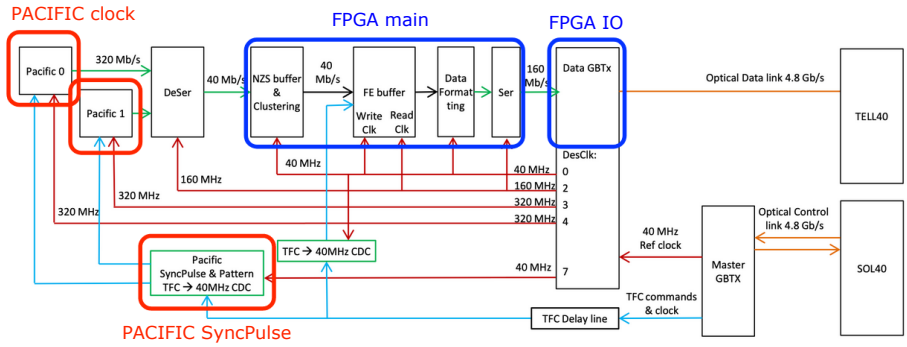

Figure 7.8: Sketch of the FE electronics and the relevant clock delays for a single data link are numbered in the Data GBTx block [93]. The blue coloured boxes indicate the FPGA clock delays, while the red coloured boxes show the PACIFIC clock delays.

The clock settings are set in DAC units, where 1 DAC corresponds to the LHC clock/512 $\approx$ 48.8 ps. The best timing settings that result from the timing scan analysis are also exported as DAC values. The aim of the timing scans is to find a single timing setting for the whole detector. As the timing scans are performed per TELL40, separate software is used to find the overall best timing setting, and where possible outliers are flagged.

7.4.1 Bit Error Rate tests

To test whether the data transmission performs as expected, Bit Error Rates (BER) are measured. The BER is defined as the number of bit errors relative to the total number of bits transmitted. The BER is saved as an 8-bit counter, corresponding to a maximum of 255. A link is considered

Table 7.1: The clocks in the SciFi front-end electronics.

Clock setting	Clock name	Clock function
CLKDEL0	FPGA main clock	Clustering board clock
CLKDEL1	Charge injection	*Not used in timing scans*
CLKDEL2	FPGA I/O clock	FPGA Sampling clock
CLKDEL3	PACIFIC 0/2	PACIFIC ASICs 0 and 2 clock
CLKDEL4	PACIFIC 1/3	PACIFIC ASICs 1 and 3 clock
CLKDEL5	LIS Start	*Not used in timing scans*
CLKDEL6	LIS Stop	*Not used in timing scans*
CLKDEL7	PACIFIC SyncPulse	Sync PACIFIC with LHC clock

"error-free" if the BER is 0. For the SciFi detector, different test patterns are used at different points in the data flow to perform BER tests within the front-end electronics. The following sections provide a short introduction to the different patterns and their purpose.

FPGA/GBTX PRBS

To test the transmission between the clustering FPGA and the Data GBTX (the FPGA main clock, with setting CLKDEL0), and the transmission between the Data GBTX and the back-end (FPGA IO clock, with setting CLKDEL2), a pseudorandom binary sequence (PRBS) BER test is used. The PRBS consists of a 7-bit word, copied 16 times to fill the 112 bits of a GBT frame. As the pattern is pseudorandom, the back-end TELL40 can predict the data bits it should have received based on this pattern, and compare it to the actual received data. The TELL40 will count the BER and output this data as an 8-bit counter word. One BER is saved per step, corresponding to a pair of delay settings, per PRBS word for every data link, leading to 16 BER counters per TELL40 per step.

The output of the scans is saved as a csv file per TELL40 in the LHCb online system. The csv file contains columns with the step number, link number inside the TELL40, step duration in seconds and the BER counter value for the 16 words. An example of the csv structure is shown in Fig. 7.9.

The FPGA scan is performed in two parts. During the first part of the scan, the FPGA PRBS is used to scan the clock between the FPGA and the Data GBTX by scanning both the FPGA Main clock and the FPGA IO clock while keeping the phase between them constant. The optimal value for the FPGA IO clock is found, and during the second part of the scan it is

```
2,0,8,255,255,255,255,255,255,255,255,255,255,255,255,255,255,255,255,255
2,1,8,255,255,255,255,255,255,255,255,255,255,255,0,255,255,255,255
2,2,8,255,255,255,255,255,255,255,255,255,255,255,255,255,255,255,255,255
2,3,8,255,255,255,255,255,255,255,255,255,255,255,255,255,255,255,255,255
2,4,8,255,255,255,255,255,255,255,255,255,255,255,255,255,255,255,255,255
2,5,8,255,255,255,255,255,255,255,255,255,255,255,255,0,255,255,255,255
2,6,8,255,255,255,255,255,255,255,255,255,255,255,255,255,255,255,255,255
2,7,8,255,255,255,255,255,255,255,255,255,255,255,255,255,255,255,255,255
2,8,8,0,0,0,0,0,0,0,0,0,0,0,0,0,0,0,0,0
2,9,8,0,0,0,0,0,0,0,0,0,0,0,0,0,0,0,0,0
2,10,0,0,0,0,0,0,0,0,0,0,0,0,0,0,0,0,0,0
2,11,0,0,0,0,0,0,0,0,0,0,0,0,0,0,0,0,0,0
```

Figure 7.9: Example snippet from a FPGA PRBS csv output file, with the columns f.l.t.r.: `Stepnumber, Datalink, Time, Word0_Errors, (...), Word15_Errors.`

fixed to the obtained value, while the FPGA Main clock is scanned. The resulting best settings are then saved as the scan result.

PACIFIC SyncPattern

The PACIFIC SyncPattern can be used to check the clock settings of the PACIFIC boards. Each half-ROB has two PACIFIC ASIC chips, whose clocks are scanned simultaneously with the same setting (CLKDEL3 and CLKDEL4). The third clock that is scanned is the SyncPulse (CLKDEL7), which aligns the 320 MHz clock of the PACIFIC board to the 40 MHz LHC clock.

The PACIFIC SyncPattern is generated by the PACIFIC ASICs, and consists of 2 bits per PACIFIC channel, leading to 4 bits per PACIFIC output line. The SyncPattern output, however, is a 8-bit word consisting of two times the 4-bit SyncPattern, combined with itself in reverse order (see Fig. 7.10). This inversion is done to make phase shifts of 12.5 ns phase shifts detectable [88]. The back-end TELL40s know what output to expect based on the set input pattern, and count the BER in a 8-bit counter per 2-bit PACIFIC channel. If the clock settings are too far from the optimal settings during the timing scan, the TELL40 risks to not recognise the GBT frame header and therefore not perform the BER test. This is called ”Loss of frame-lock”, and has to be prevented to ensure stable data transmission. A channel is only working correctly if the BER value is 0, the channel is ”locked” and the channel remains ”locked” throughout the scan.

The PACIFIC SyncPattern is passed through the normal data flow,

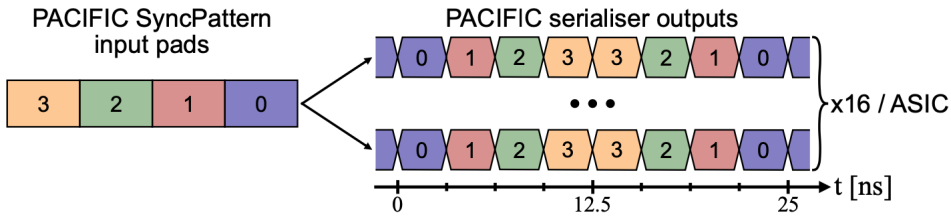

Figure 7.10: Schematic drawing of the PACIFIC SyncPattern, showing that the 4 bits are combined with the same, inverted 4 bits, such that 12.5 ns phase shifts can be detected.

processed by the clustering FPGA. No clustering is performed and the data is simply passed through. The FPGA, however, is limited in bandwidth and can therefore not process the SyncPatterns for all 128 PACIFIC channels simultaneously. The maximum amount of channels that can be tested at the same time is 32, and as a result the BER test has to be repeated four times to cover all 128 PACIFIC channels. The group of channels that is scanned in the step is set by the FPGA "data out" mode setting on the FPGA board, as shown in Tab. 7.2.

Table 7.2: PACIFIC SyncPulse FPGA "data out" mode settings table showing the correspondence to the scanned channels.

FPGA "data out" mode	**SiPM channels scanned**
8	0 - 31
9	32 - 63
10	64 - 95
11	96 - 127

7.4.2 Analysis methods

The output data of the timing scans is in the csv format, while the filename contains the TELL40 identifier. To map the TELL40 to a geographical detector location the `FibreDB` table is used [94]. This table contains an up-to-date database of, amongst others, the SciFi TELL40 cabling, matching a TELL40 name and link number to a geographical detector location and FE link number. [1]

[1] As an example, the TELL40 `SCPRBS151` corresponds to `T1L0Q0D0` in the detector.

The goal of the timing scans is to find the error-free region of clock delay settings. When the BER is 0 for a specific step, it means that the clock settings corresponding to the step are a suitable setting for the link under inspection. To do this analysis[1], all consecutive steps with a BER counter of 0 are recorded per link per word. In the case of multiple "error-free" regions, the largest step-region is kept. Afterwards, the common error-free interval is found for all the words inside a link, and for all words and links inside the TELL40. The central step value of this region is calculated, and the corresponding clock DAC settings are exported to a XML file, which can be used to update the settings on the FE electronics. This process is performed separately for both parts of the scan with a resolution of 1 DAC per step. In the monitoring programme, the analysis results are displayed with histograms, which are made both using the scan step number, as well as the corresponding clock settings. The following histograms are produced and shown in the coming results section:

- 1D BER histogram per link per word/channel or averaged over all words per link/channel
- 2D BER histogram per TELL40
- 2D plot showing the error-free region per link (in steps and time)
- 2D plot showing the error-free region per TELL40 (in steps and time)
- Error-free region center and width overview histograms
- Overview 2D plots per detector layer showing the error-free region per link

After the analysis is run, all the obtained error-free intervals are compared and the best setting for the whole SciFi detector is found by comparing the obtained settings for all links and checking if there is a common delay setting that covers the whole detector. A common delay setting for the whole detector is beneficial but necessary, however it comes with pragmatic advantages e.g. simplifying the beam timing scan. If no common clock setting can be found, the best setting per link is used, and the clock settings are updated for all links in the detector.

[1] The analysis of the timing scans is performed in `python`, using the `pandas`, `matplotlib`, and `snakemake` packages. The code can be found on the GitLab page [95].

7.4.3 Results

This section contains the results obtained from the timing scans. Firstly, the best setting is chosen for the FPGA IO clock, which is then fixed to this best setting during the FPGA main clock scan. Subsequently, the PACIFIC clock is scanned, while fixing the two FPGA clocks to their best values. Finally, the PACIFIC SyncPulse is scanned by fixing the FPGA clocks and PACIFIC clock to their best values. The final results are then exported for use in the SciFi detector hardware.

FPGA IO clock scan

Inspecting the 1D BER histogram in Fig. 7.11, a clear error-free region can be seen centered around step 73, with a rising edge on both sides. [1] The 2D overview graph in Fig. 7.11 shows all resulting error-free timing intervals for the third TELL40 of an arbitrary quarter, T1L1Q0D3, with the BER best value varying for individual words and links. The white gaps between the light-green regions correspond to data links that are not connected to a SiPM, and therefore are also not scanned. Fig. 7.12 shows the center and width of the error-free region for all TELL40s in the detector, split per T station and detector side. The median value of all words for the whole detector is found to be 135 ± 4 DAC, corresponding to 6588 ± 195 ps, which falls within the error-free region of all links.

[1] This behaviour is also known as a "bathtub plot", due to it's bathtub-like shape.

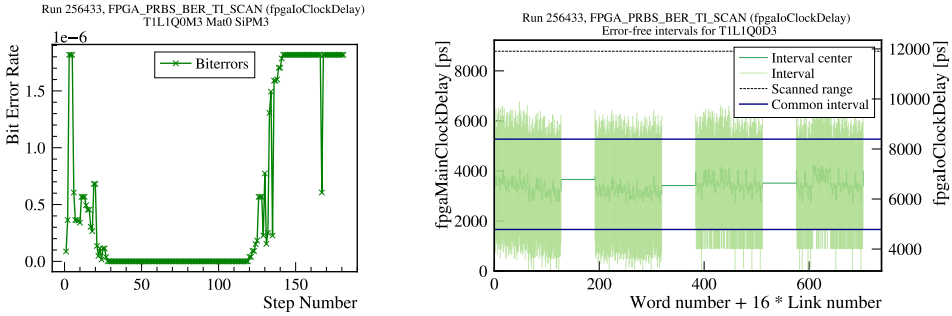

Figure 7.11: 1D histogram of the averaged BER over all words for a given single link (left) and 2D BER overview plot for all links in a single TELL40 (right) for the FPGA IO clock scan. The dark green line shows the error-free interval center, while the light green bars indicate the full error-free region per word. The blue lines indicate the common error-free region for the whole TELL40. Note that the step number on the vertical axis corresponds to a pair of settings for both the FPGA IO and FPGA main clock delays, as shown by the double y-axis in the right plot.

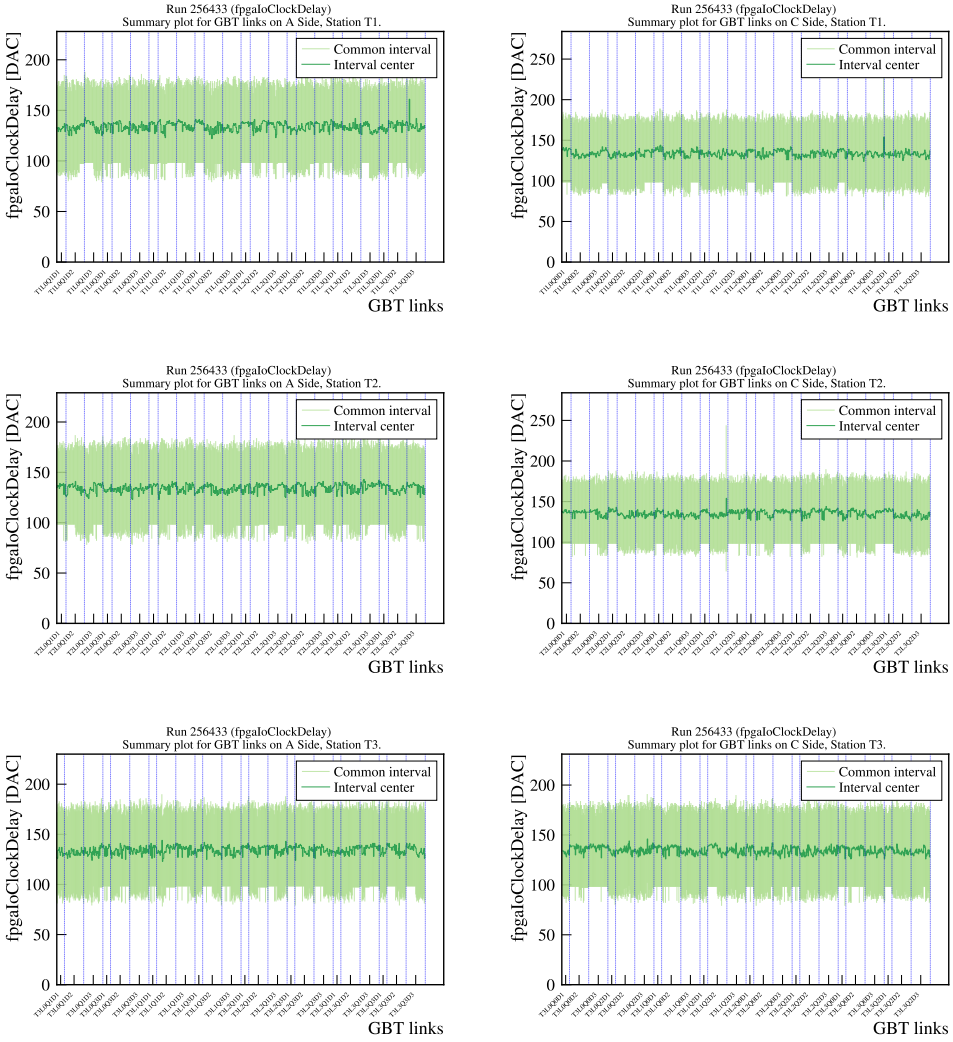

Figure 7.12: 2D overview histograms for the full SciFi detector showing the error-free region in DAC values per link for the FPGA IO clock scan. Each plot shows the result for a given station (top to bottom) and detector side (left and right). The dotted blue lines indicate the TELL40 boundaries. The mean and width of the error-free region is similar throughout the whole detector.

FPGA main clock scan

Fixing the FPGA IO clock to the best value, the FPGA main clock is scanned. Example results for a single link and single TELL40 are shown in Fig. 7.13. Overview plots for the full detector, split by T station and side, are shown in Fig. 7.14. The graphs show a stable region across the full detector, allowing for a single setting for the whole detector. The optimal setting for the FPGA main clock is found to be 61 ± 2 DAC, corresponding to 2977 ± 98 ps. To check for the stability of the scan method, the scan is repeated and the resulting best error-free intervals and centers are compared. This is shown in Fig. 7.15. The error-free intervals are found to be stable, although two links have a significantly different best value at A side T1 and C side T2. A clear reason for this is currently not known, and further studies are necessary to understand the cause. This is, however, not expected to be a problem for the detector operation, as the error-free intervals are still overlapping.

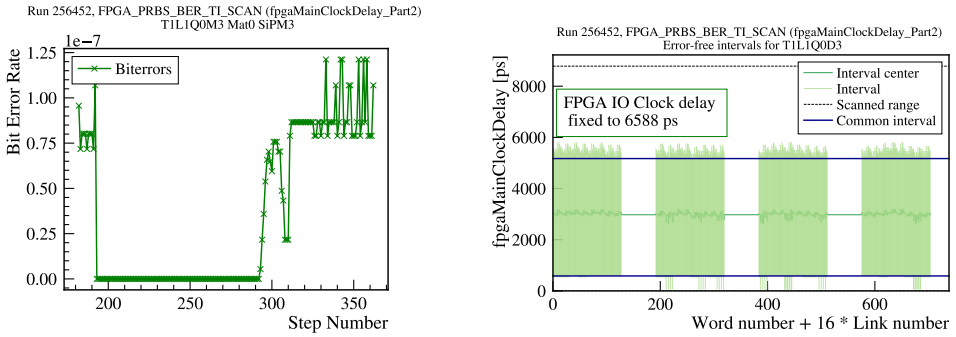

Figure 7.13: 1D histogram of the averaged BER over all words for a single link (left) and 2D BER overview plot for a single TELL40 (right) for the FPGA Main clock scan. The dark green line shows the error-free interval center, while the light green bars indicate the full error-free region per word. The blue lines indicate the common error-free region for the whole TELL40.

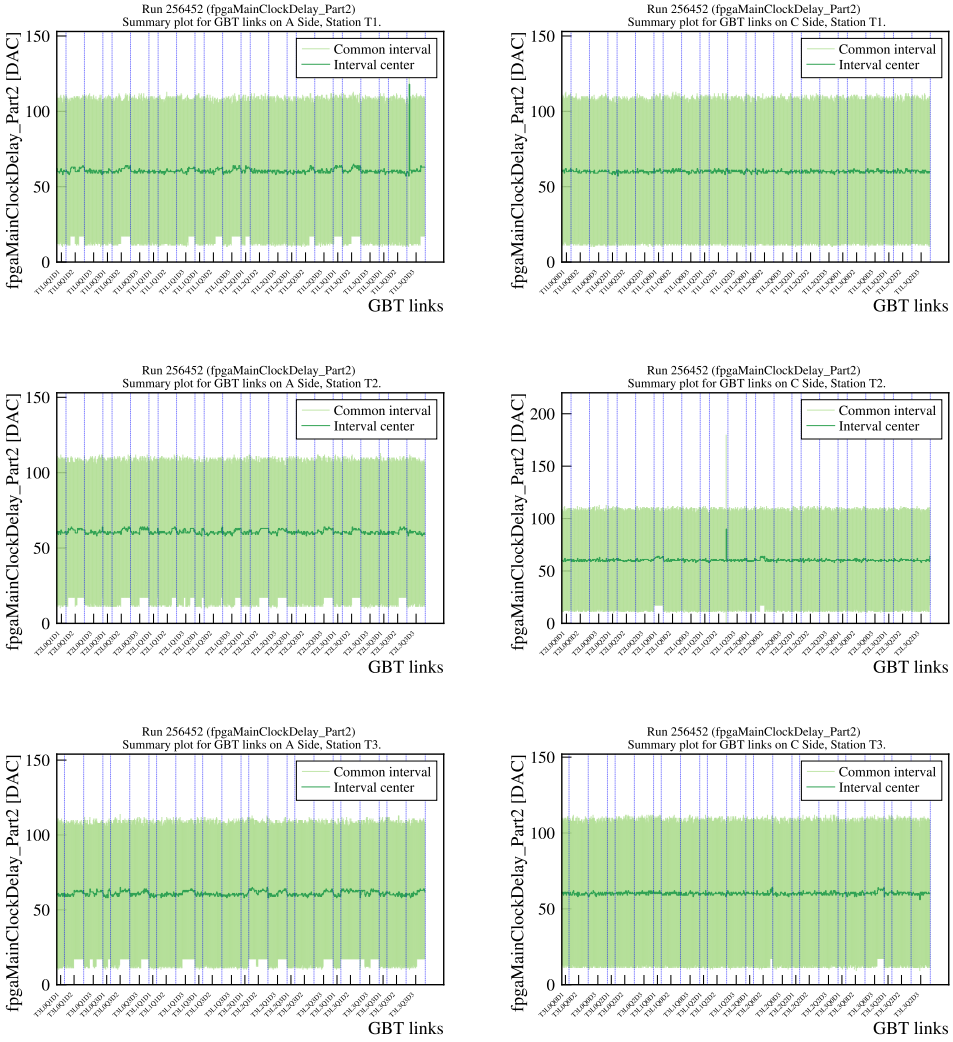

Figure 7.14: 2D overview histograms for the full SciFi detector showing the error-free region in DAC values per link for the FPGA Main clock scan. Each plot shows the result for a given station (top to bottom) and detector side (left and right) where the dotted blue lines indicate the TELL40 boundaries. A similar interval center is visible throughout the whole detector.

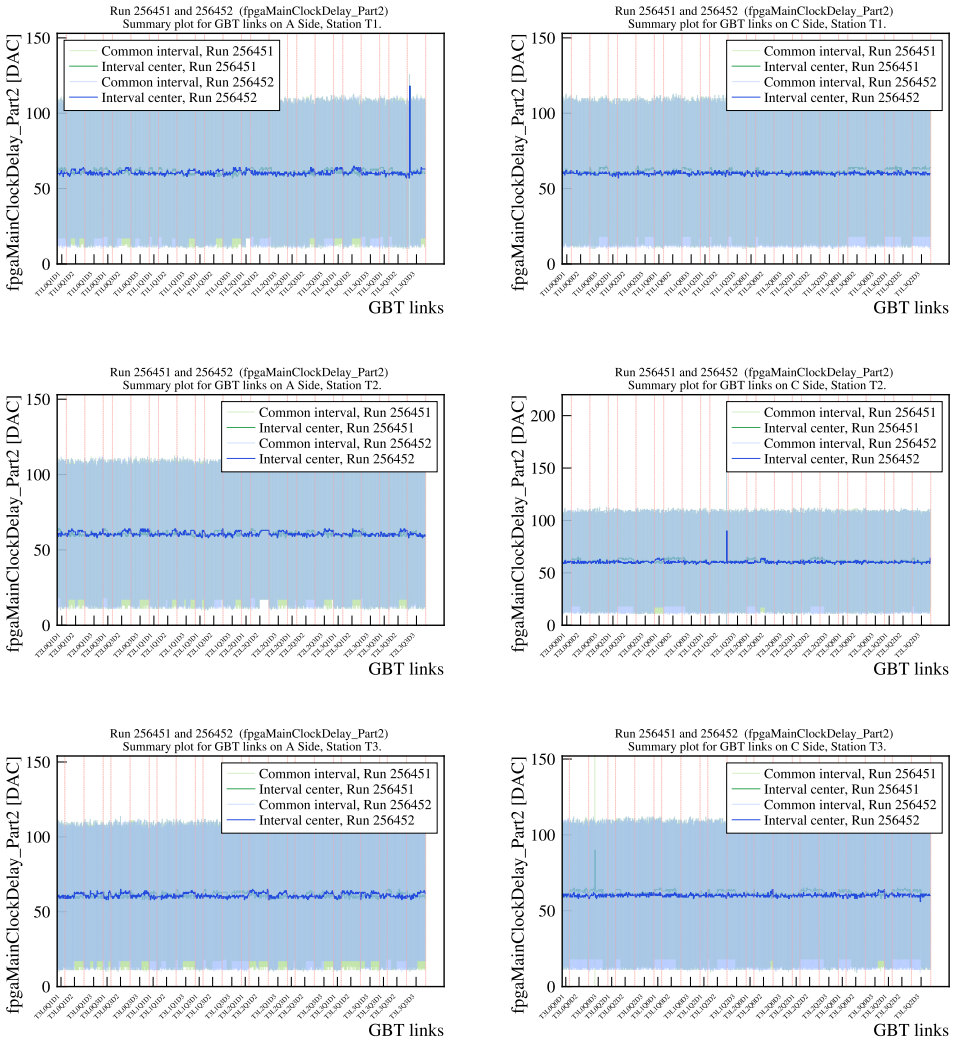

Figure 7.15: 2D comparison graphs between two FPGA main clock scan runs, showing the error-free region and centers in blue and green. The error-free regions for each link overlap for all links, although outliers are visible.

PACIFIC clock scan

The PACIFIC clock delay setting is scanned while fixing the FPGA IO and FPGA main clock to their best values of 135 and 60 DAC, respectively. Fig. 7.16 illustrates the 1D and 2D BER plots for a single link and a single TELL40 for different PACIFIC clock settings. Comparing the resulting error-free regions and centers to the FPGA clock scans, it can be seen that the PACIFIC clock varies more between links and channels within a TELL40. There are also sets of 32 channels that appear to have a shifted best PACIFIC clock settings, e.g. around channel 2100 in Fig. 7.16. The observed shift for the group of 32 channels is unexpected, as the lowest level ASICs on the PACIFIC boards receive input from 64 channels (see Fig. 7.5). It would therefore be expected in case of issues with an ASIC that a set of 64 channels would be shifted, rather than for a set of 32. Further investigation is needed to determine what is causing the sets of 32 channels to be outside of the common error-free region. For data taking, having a set of 32 channels outside of the common error-free region is not a problem, as this will hardly be noticed in the final cluster data.

Fig. 7.17 shows the PACIFIC clock scan results for the full detector. The best setting per channel indeed fluctuates more than for the FPGA clocks, although an overall stable trend can be seen. The resulting best setting for the full detector is found to be 87 ± 5 DAC, or 4246 ± 244 ps, although this setting would not be error-free for all channels. Individual settings per link could be considered as an alternative solution, but it was decided to first fix the PACIFIC clock to the best setting for the whole detector, and then perform a PACIFIC SyncPulse scan to see if an single optimal setting for the whole detector is possible.

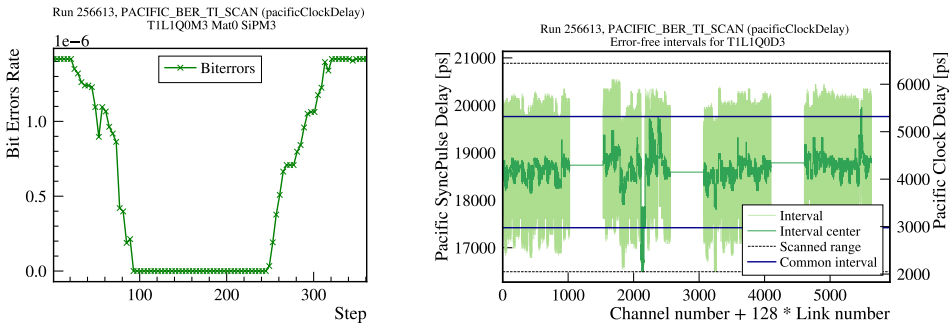

Figure 7.16: 1D histogram of the averaged BER over all words for a single link (left) and 2D BER overview plot for a single TELL40 (right) for the PACIFIC clock scan with CDC setting 0. The dark green line shows the error-free interval center, while the light green bars indicate the full error-free region per word. The blue lines indicate the common error-free region for the whole TELL40, excluding the set of 32 channels falling out of this region.

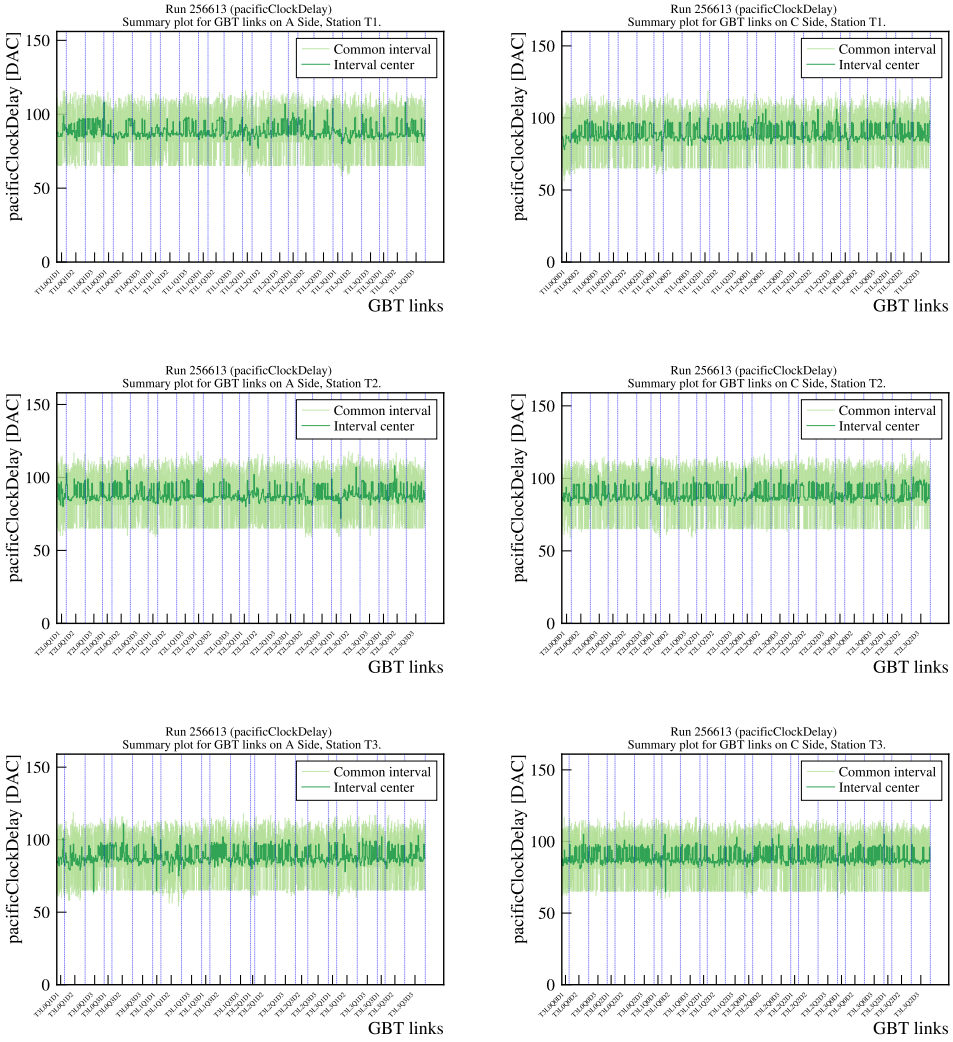

Figure 7.17: 2D overview histograms for the full SciFi detector showing the error-free region in DAC values per link for the PACIFIC clock scan split by side and T station, where the dotted blue lines indicate the TELL40 boundaries. A smaller error-free region with a higher variation in central value can be seen compared to the FPGA clock scans.

PACIFIC SyncPulse

Finally, the PACIFIC SyncPulse is scanned while fixing both FPGA clocks and the PACIFIC main clock to their best values of 135, 61, and 87 DAC, respectively. Example 1D and 2D BER plots for a single link and a single TELL40 are shown in Fig. 7.18.

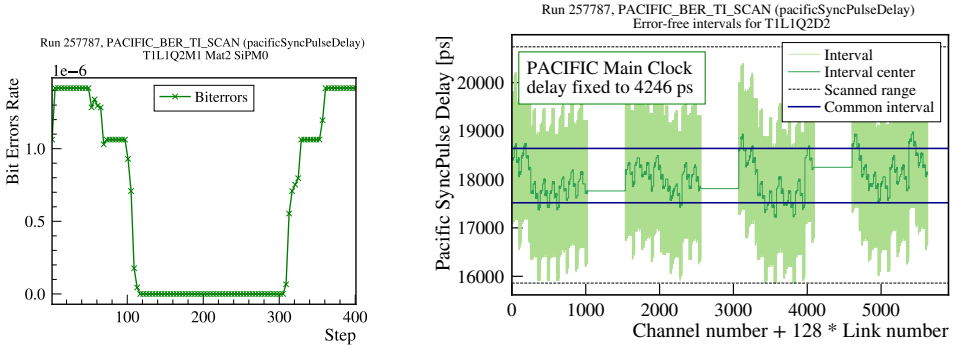

Figure 7.18: 1D histogram of the averaged BER over all words for a single link (left) and 2D BER overview plot for a single TELL40 (right) for the PACIFIC SyncPulse scan with CDC setting 0. The dark green line shows the error-free interval center, while the light green bars indicate the full error-free region per word. The blue lines indicate the common error-free region for the whole TELL40.

Fig. 7.18 shows a fluctuating center of the error-free region throughout the TELL40, however a common error-free region is still present. It also shows a "zig-zag" pattern for the error-free region in sets of 64 channels, all having a slightly different center and width. An explanation for this behavior is currently unknown, however the 64-channel pattern is likely due to the 64-channel granularity of the PACIFIC readout in the ASICs.

Fig. 7.19 shows the PACIFIC clock scan results for the full detector, split by side and T station. Compared to the PACIFIC main clock scan, the error-free region is more stable and has a smaller variability. The obtained best value for the whole detector is 367 ± 6 DAC, corresponding to 17911 ± 292 ps. This setting in combination with the previously obtained FPGA main clock, FPGA IO clock, and the PACIFIC main clock settings are found as the best timing settings for the full SciFi detector electronics. All the best settings are summarized in Table 7.3.

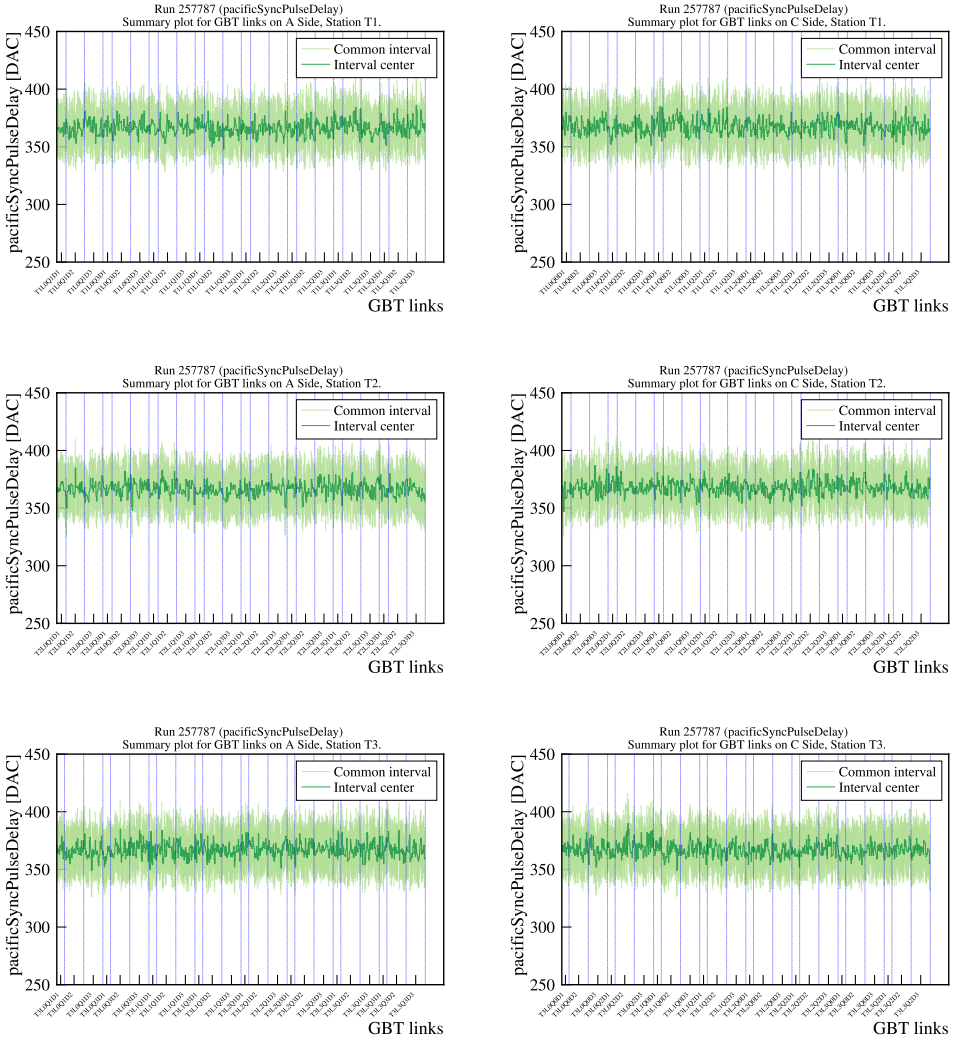

Figure 7.19: 2D overview histograms for the full SciFi detector showing the error-free region in DAC values per link for the PACIFIC SyncPulse scan split by side and T station, where the dotted blue lines indicate the TELL40 boundaries. Compared to the PACIFIC main clock scan, here an error-free region for the whole detector is visible.

Table 7.3: Best values for the FPGA main clock, FPGA IO clock, PACIFIC main clock, and PACIFIC clock for the full SciFi detector.

Clock	**Best value (DAC)**
FPGA main clock	61 ± 2
FPGA IO clock	135 ± 4
PACIFIC main clock	87 ± 5
PACIFIC SyncPulse	367 ± 6

7.4.4 Updated scan results

During the June 2023 technical stop, after the writing of this thesis chapter, the timing scans were repeated due to an update in the FE firmware. This update potentially changed the timing behavior of the FE, and therefore the timing scans were repeated to ensure that any possible changes to the clock delay settings were accounted for. The results of the updated scans are summarized in Tab. 7.4. The values for the FPGA IO clock and the PACIFIC main clock delay stayed the same within uncertainty, while the FPGA Main clock and PACIFIC SyncPulse delay shifted to higher values.

Table 7.4: Updated best values for the FPGA main clock, FPGA IO clock, PACIFIC main clock, and PACIFIC clock for the full SciFi detector as of June 2023.

Clock	**Best value (DAC)**
FPGA main clock	76 ± 2
FPGA IO clock	134 ± 4
PACIFIC main clock	86 ± 5
PACIFIC SyncPulse	393 ± 6

Further timing scans will be taken during the operation of the LHCb detector, as they can also be used to monitor possible radiation damages to the electronics. The results of these scans will be used to update the timing settings if needed.

7.5 Clustering and Decoding

As illustrated in Fig. 7.4, the SciFi detector uses SiPMs with set thresholds to convert the incoming traversing particle signal to a digital cluster signal. The clustering is performed on the FPGA boards, as the data rate of the SiPMs is

too high to directly transmit the raw threshold values to the LHCb software. Running the clustering algorithm allows the SciFi detector to reduce the data rate while suffering a negligible impact in detector resolution.

The FPGA executes the clustering algorithm using the digital SiPM signals from the PACIFIC boards. For simulation purposes and to compare the clustering using the raw NZS SiPM ADC threshold data, the same algorithm is also implemented in the LHCb software. The cluster data is then decoded in the LHCb software into cluster objects that are used to run tracking algorithms in the High Level Trigger system. The following sections describe the implementation of both the clustering and decoding algorithms of the SciFi detector.

7.5.1 Clustering

Due to bandwidth limitations in the front-end to back-end connection through the GBTX, a zero-suppressed clustering algorithm is used that only transmits clusters meeting specific threshold requirements [84].

The algorithm starts from the first digit and looks for hits in adjacent SiPM channels. If the cluster candidate consists of a single channel, the channel needs to surpass the highest photoelectron threshold t_3 to be considered a cluster. If four (the maximum allowed cluster size) or fewer adjacent channels have hits, the algorithm checks if the sum of the ADC counts of the channels is greater than or equal to the sum of the first two set thresholds, currently corresponding to $t_1 + t_2 = 1.5 + 2.5 = 4.0$ photoelectrons. The optimal detector position of the cluster is calculated through a weighted sum of the channel positions, as defined in Eq. 7.1 where w_i is the weight corresponding to its photoelectron threshold, as shown in Tab. 7.5. These weights represent the average number of photoelectrons seen in channels that crossed the corresponding thresholds, as studied during SciFi beam tests. These weights improve the resolution compared to using the raw photoelectron values. [96].

$$\text{cluster position} = \frac{\Sigma[\text{Channel position}_i \times w_i]}{\Sigma[w_i]} \tag{7.1}$$

The position is then saved in a 8-bit format, consisting of a 7-bit channel number and an interchannel position bit. The interchannel bit improves the resolution by half a SiPM channel, and specifies if the cluster was either centered on a channel or placed in between channels. The bit is defined as 0 in the interchannel range $[-0.25, 0.25]$ and 1 in the range $[0.25, 0.75]$.

Table 7.5: Clustering photoelectron thresholds and their corresponding channel weights.

Category	t_1	t_2	t_3
Photoelectron threshold	1.5	2.5	4.5
Weight	1	2	6

Clusters consisting of more than four channels are split into cluster "fragments" of maximum four channels. These large clusters originate mostly from particles traversing the detector at a large angle, delta electrons or from noise hits in the neighboring channels. To reduce the number of cluster fragments that have to be transmitted via the TELL40 boards, only the first and last cluster fragments are sent, and a special large cluster flag bit is used to mark them, being the 9th bit in the 9-bit cluster objects. During the decoding, the missing cluster fragments are reconstructed using the median position of the two edge clusters and the defined maximum cluster size. A schematic drawing of the different cluster types within the clustering algorithm is shown in Fig. 7.20.

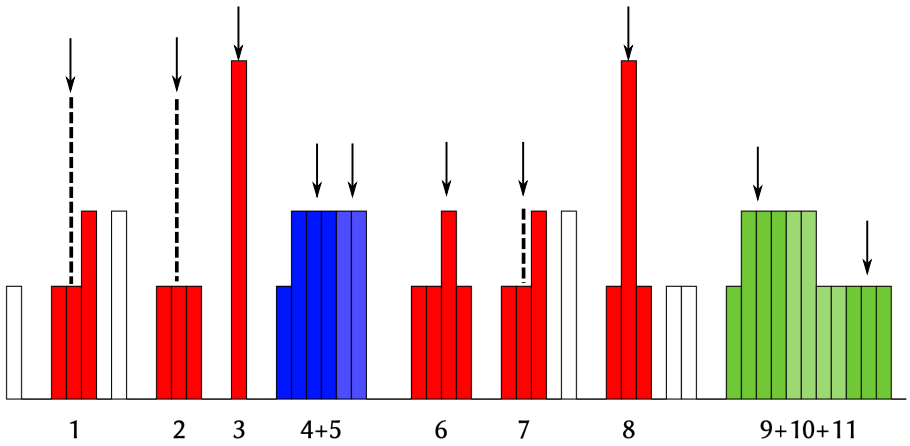

Figure 7.20: Schematic drawing of the SciFi clustering algorithm, where the height of the bar indicates which photoelectron threshold the channels have reached [84]. White channels are not part of a cluster, as they do not meet the set threshold requirements. Red clusters are saved with a weighted position, blue clusters are fragmented into two and are flagged as large clusters, green clusters are fragmented but only the dark green clusters are transmitted. The arrows indicate the cluster position.

7.5.2 Decoding

The decoder[1] loads all the raw banks, which are then reordered, because the banks do not arrive in order of geographical detector location. The decoder reads the so-called SourceID, which contains information about the detector location of the TELL40 that produced the bank [97], and sorts the banks in increasing order of SourceID.

Subsequently, checks are performed on the incoming banks, to ensure that the bank is not empty, that the bank indeed has a SourceID that is known as a connected TELL40, and that the bank does not contain an unphysical number of headers. Once the bank is validated, the 32-bit Local Header, as shown in Fig. 7.7, is currently skipped, and the possible padded zeroes that are appended to the end of the bank by the TELL40 are removed. The clusters in the bank are then read with 16 bits at the time (except in the case of large-flagged clusters where 32-bits are used to load two clusters at the same time). For large-flagged clusters, the distance between the two cluster channel positions is calculated, and cluster objects are created to fill the gap between them if needed.

As there is the possibility of swapped TELL40 links, either by design or by accident, the decoding cannot assume that the banks from the links arrive in order of their detector location. Since such ordering is a requirement from the tracking algorithms, and the decoder therefore has to account for this by reordering the clusters. This is done using the link index within the current bank in combination with the channel of each to-be-decoded cluster, to find the corresponding SiPM detector location of the cluster. [2] The readout map contains a list of TELL40 SourceIDs together with the corresponding detector location. Together with the channel number, the cluster is then assigned to its correct location inside the detector.

Subsequently the resulting software cluster representation[3] is stored in an array. This process is repeated until all the clusters in the bank are decoded. The ordered clusters are then saved and passed on to the LHCb reconstruction software, where they are used to reconstruct charged-particle tracks.

[1] The 16-bit clusters that originate from the TELL40s are decoded by the `FTRawBankDecoder` software algorithm into `FTCluster` objects usable within the LHCb reconstruction software.

[2] This is done using the so-called `FTReadoutMap` [98].

[3] The `FTCluster` object

7.6 Data monitoring using first SciFi data

During the second half of 2022, the first SciFi data was collected during the LHCb commissioning run. The SciFi detector was able to record clusters, and the detector was time-aligned with the LHC bunch-crossing ID, as shown in Fig. 7.21. The cluster occupancy shows, as expected, an exponentially decreasing distribution with increasing distance from the beampipe. While most SiPM data links show the correct bunch-crossing ID, it should be noted that the data was collected without the best electronic timing settings resulting from the timing scans described in Sec. 7.4, potentially explaining why some of the links show a shift.

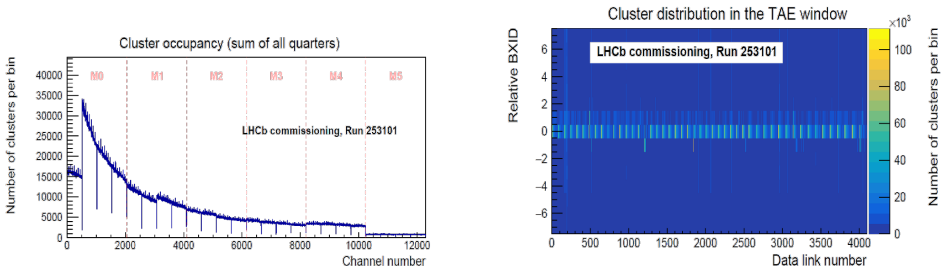

Figure 7.21: First SciFi clusters from the data collected during the 2022 commissioning run with the channels ordered in increasing x coordinate [99]. Left: number of clusters per channel for the full SciFi detector. Right: relative bunch-crossing ID distribution for all SciFi data links after time alignment, showing a distribution centered around 0.

The new HLT1 and (preliminary) HLT2 reconstruction algorithms were run over the obtained VELO and SciFi clusters, to reconstruct the first long tracks. The reconstructed long tracks for a part of the acquired data are shown in Fig. 7.22, where the distributions of the transverse momentum, pseudorapidity, number of SciFi hits, and χ^2 per degree of freedom are shown. By using the resulting reconstructed particle tracks from the preliminary HLT2 reconstruction, the first invariant-mass distributions were obtained, see Fig. 7.23. The top figure shows reconstructed $\Xi^- \to \Lambda\pi^-$ decays, while the bottom figure shows $J/\psi \to \mu^+\mu^-$ candidates using the `IsMuon` selection on the tracks. These distributions illustrate the first Λ and J/ψ particles reconstructed in the upgraded LHCb detector, marking an important milestone for the LHCb commissioning, and the first step towards future Run 3 analyses on rare $\Lambda_b^0 \to \Lambda\ell^+\ell^-$ decays.

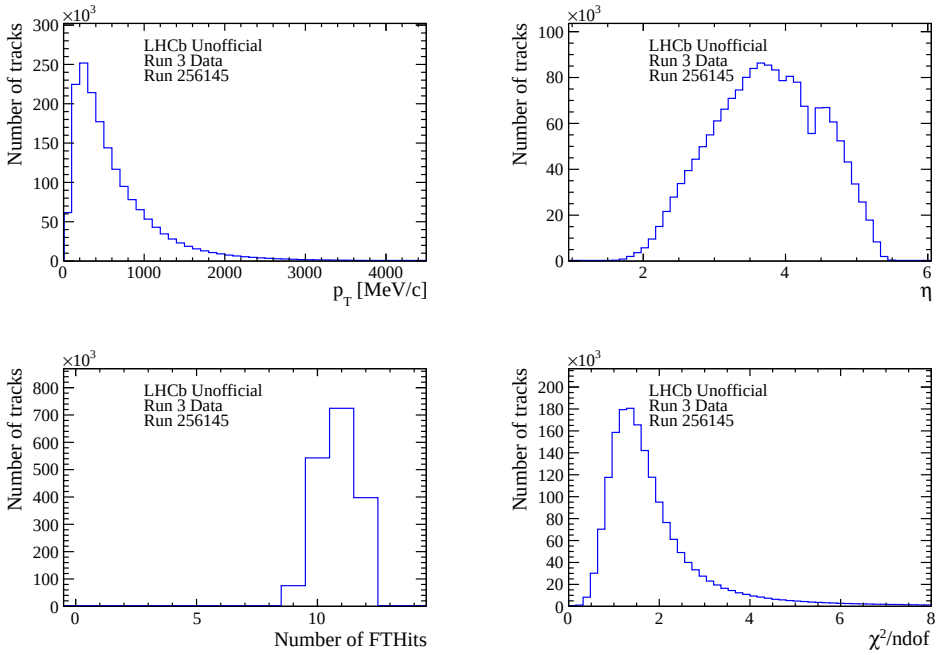

Figure 7.22: Reconstructed long track distributions using part of the 2022 commissioning data. From top left to bottom right: track transverse momentum, pseudorapidity, number of SciFi hits per track, and χ^2 per degree of freedom.

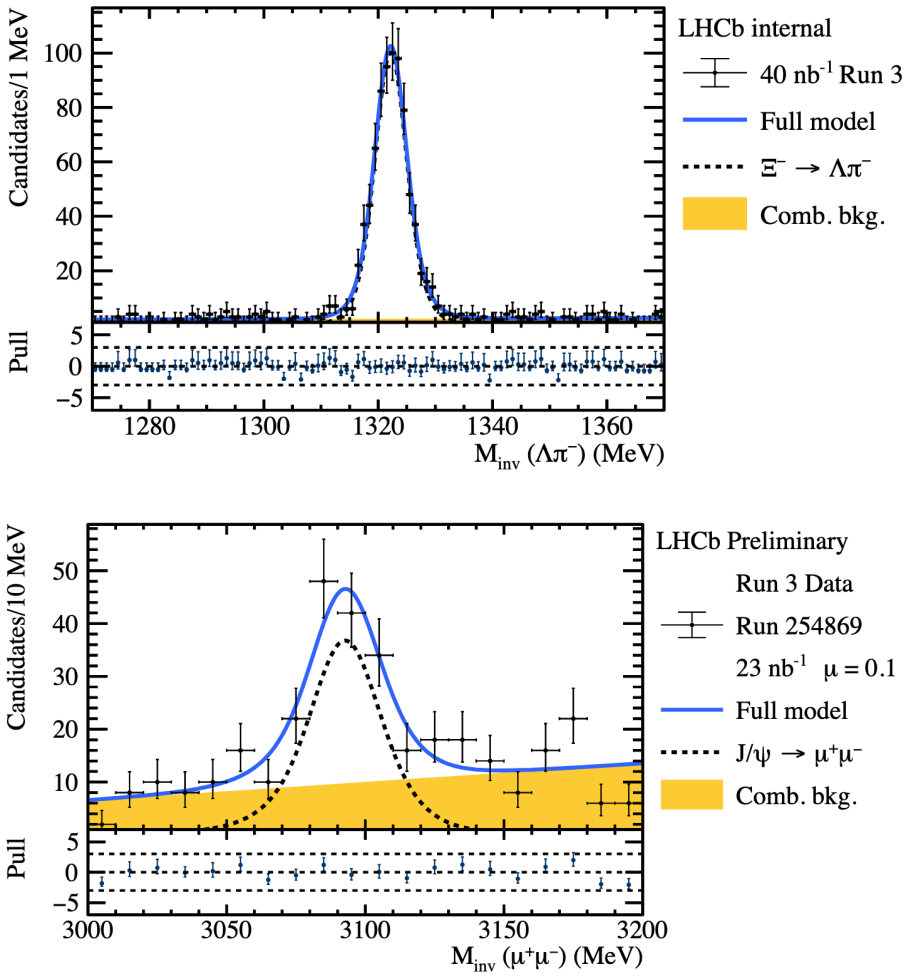

Figure 7.23: Reconstructed $\Xi^- \to \Lambda\pi^-$ (top) and $J/\psi \to \mu^+\mu^-$ (bottom) invariant mass distributions using long tracks from the 2022 commissioning data [100].

8 Conclusion and outlook

This thesis presents the measurement of the $\Lambda_b^0 \to J/\psi\,\Lambda$ branching fraction and the path towards measuring the lepton flavour universality ratio R_Λ using $\Lambda_b^0 \to \Lambda\ell^+\ell^-$ decays. The $\Lambda_b^0 \to J/\psi\,\Lambda$ branching fraction is measured to be $(3.08 \pm 0.26 \pm 0.12) \cdot 10^{-4}$, which is in agreement with theoretical predictions and previous measurements. The obtained value provides a factor three improvement in precision compared to the previous most accurate measurement by the D0 collaboration [48]. The $\Lambda_b^0 \to J/\psi\,\Lambda$ decays, as well as $\Lambda_b^0 \to \psi(2S)\Lambda$ decays, are used as a control mode for the R_Λ analysis, using the ratio of electron and muon modes to check the understanding of the absolute selection efficiencies. Whereas a downward shift in the single ratios $r^{-1}_{J/\psi}$ and $r^{-1}_{\psi(2S)}$ is observed, the double ratio $R^{-1}_{\psi(2S)}$ agrees with the expected value of 1. This shows, on the one hand, the power of the double ratio to cancel out systematic uncertainties, while on the other hand it exposes the need for further understanding the single ratio measurements.

Looking ahead, the upgraded LHCb experiment has started recording data in 2022 and 2023, and will continue to do so until the end of Run 3 and Run 4, with a total expected integrated luminosity of $50\,\text{fb}^{-1}$ [80]. The SciFi detector tracking stations, replacing the previous IT and OT system, are currently in the process of being commissioned, and the first Λ and J/ψ candidates have been recorded. The electronics timing scans presented in this thesis provide a crucial input for the time alignment of the detector. In the future, as LHCb continues to operate, the timing scans will have to be repeated to monitor the stability of the detector and account for possible ageing effects.

The upgraded detector system, combined with the replacement of the hardware trigger by a full software based system, will provide a significant

increase in the amount of data recorded by LHCb. The larger dataset will benefit the rare decay analyses presented in this thesis, especially for the statistically limited electron channel $\Lambda_b^0 \to \Lambda e^+ e^-$. The total Run 1 and Run 2 dataset combined corresponds to an integrated luminosity of $9\,\text{fb}^{-1}$, while the expected integrated luminosity for Run 3 and Run 4 is $50\,\text{fb}^{-1}$, leading to a factor 6 increase of the total dataset. In addition, the replacement of the L0 hardware trigger by a more elaborate software system allows to lower the requirement on the transverse energy of the electron, thus further increasing the event yield. The statistical uncertainty on the R_Λ measurement is dominated by the uncertainty on the number of $\Lambda_b^0 \to \Lambda e^+ e^-$ candidates, which will be reduced by at least a factor $\sqrt{6} \approx 2.4$, leading to a comparably accurate measurement to the current latest LHCb R_K and R_{K^*} mesonic LFU tests [44, 45]. In addition, the new trigger allows to lower the requirement on the transverse energy of the electron, thus further increasing the event yield. With an increase in integrated luminosity, it also becomes possible to accurately measure the angular observables in the $\Lambda_b^0 \to \Lambda \mu^+ \mu^-$ decays and for the first time in the $\Lambda_b^0 \to \Lambda e^+ e^-$ decays, further testing the SM predictions and flavour anomalies. The search for $\Lambda_b^0 \to \Lambda e^\pm \mu^\mp$ decays will also benefit from the increased dataset, allowing for a possible observation of these forbidden decays or a more stringent upper limit on the branching fraction.

To conclude, there are many exciting prospects in the study of the flavour anomalies using rare baryonic decays. The $\Lambda_b^0 \to \Lambda \ell^+ \ell^-$ analyses are promising and provide an independent crosscheck to the mesonic b-mesons to test lepton flavour universality and lepton flavour conservation. This will only be extended in the future, when the SciFi detector is fully commissioned and the LHCb experiment continues to record more data.

A L0 trigger TCK alignment

The following tables show the E_T, p_T, and $p_T^1 \cdot p_T^2$ thresholds used during the different data taking years. The values are given in DAQ ADC units. Furthermore, a requirement is placed on the (offline) E_T of the electron that fired the `L0Electron` trigger, which is tighter than the L0Electron requirement. The used requirements are $E_T > 3000\,\text{MeV}$ for Run 1, $E_T > 2700\,\text{MeV}$ for R2p1, $E_T > 2955\,\text{MeV}$ in 2017, and $E_T > 3150\,\text{MeV}$ in 2018. This selection removes electrons that have an E_T lower than the `L0Electron` threshold, but were still considered signal due to calorimeter noise.

TCK hex	$E_T^{L0}(e)$	$p_T^{L0}(\mu)$	$p_T^{L0}(\mu_1) \cdot p_T^{L0}(\mu_2)$	% lumi MU	% lumi MD
0x40760037 (MC)	125	37	1050	-	-
0x360032	125	37	1050	0.00	0.56
0x5A0032	125	37	1050	7.99	4.73
0x5D0033	125	20	1050	0.47	0.00
0x6D0032	125	37	1050	0.00	16.69
0x730035	125	37	1050	27.66	10.28
0x760037	125	37	1050	22.16	31.87
0x790037	125	37	1050	8.34	0.00
0x790038	125	37	1050	31.86	34.83

Table A.1: L0 threshold values for the 2011 TCKs.

TCK hex	$E_T^{L0}(e)$	$p_T^{L0}(\mu)$	$p_T^{L0}(\mu_1) \cdot p_T^{L0}(\mu_2)$	% lumi MU	% lumi MD
0x409F0045 (MC)	148	44	1600	-	-
0x7F0040	125	37	1050	0.00	0.06
0x860040	125	37	1050	0.00	0.49
0x8C0040	125	37	1050	0.00	5.76
0x94003D	136	44	1600	16.24	10.14
0x97003D	136	44	1600	11.91	14.54
0x990042	136	44	1600	37.25	22.73
0x990044	148	44	1600	2.99	10.57
0x9A0042	136	44	1600	0.00	0.00
0x9F0045	148	44	1600	2.72	0.00
0xA10044	148	44	1600	2.52	0.00
0xA10045	148	44	1600	6.93	0.00
0xA20044	148	44	1600	0.16	0.00
0xA30044	148	44	1600	16.25	13.34
0xA30046	143	44	1600	1.91	1.05
0xA90046	143	44	1600	0.00	5.92
0xAB0046	143	44	1600	0.00	4.80
0xAC0046	143	44	1600	0.83	9.74

Table A.2: L0 threshold values for the 2012 TCKs.

TCK hex	$E_T^{L0}(e)$	$p_T^{L0}(\mu)$	$p_T^{L0}(\mu_1) \cdot p_T^{L0}(\mu_2)$	% lumi MU	% lumi MD
0x411400A2 (MC)	112	56	676	-	-
0x10600A2	112	56	676	0.00	50.16
0x10600A3	95	48	676	0.00	31.68
0x10600A6	70	36	480	0.00	0.03
0x10600A7	58	30	460	0.00	0.53
0x10700A1	75	38	570	0.00	3.33
0x10800A2	112	56	676	36.14	5.95
0x11400A8	112	56	676	54.05	0.00

Table A.3: L0 threshold values for the 2015 TCKs.

TCK hex	$E_T^{L0}(e)$	$p_T^{L0}(\mu)$	$p_T^{L0}(\mu_1) \cdot p_T^{L0}(\mu_2)$	% lumi MU	% lumi MD
0x5138160F (MC)	100	36	900	-	-
0x11291603	88	22	400	0.00	3.97
0x11291604	94	26	576	0.00	2.89
0x11291605	108	30	676	0.00	9.13
0x11371609	98	26	676	0.00	8.38
0x1137160E	108	30	676	0.00	2.65
0x11381609	98	26	676	0.00	0.80
0x1138160E	108	30	676	0.00	3.69
0x1138160F	100	36	900	0.00	67.01
0x11321609	98	26	676	13.46	0.00
0x11341609	98	26	676	14.85	0.00
0x11351609	98	26	676	2.80	0.00
0x11361609	98	26	676	52.02	0.00
0x11381611	109	30	784	5.55	0.00
0x11381612	109	32	900	11.29	0.00

Table A.4: L0 threshold values for the 2016 TCKs.

TCK hex	$E_T^{L0}(e)$	$p_T^{L0}(\mu)$	$p_T^{L0}(\mu_1) \cdot p_T^{L0}(\mu_2)$	% lumi MU	% lumi MD
0x51611709 (MC)	88	28	676	-	-
0x11541707	96	34	1296	0.00	11.04
0x115417A7	96	34	1296	0.00	0.07
0x11561707	96	34	1296	17.22	29.00
0x11611707	96	34	1296	0.00	15.63
0x11611708	88	22	400	0.00	16.23
0x11611709	88	28	676	0.00	27.91
0x11601708	88	22	400	19.11	0.00
0x11601707	96	34	1296	23.76	0.00
0x11501705	108	30	676	23.60	0.00
0x11501704	94	26	576	4.80	0.00
0x11501706	112	38	1296	5.27	0.00
0x11501703	88	22	400	4.28	0.00
0x114E1702	78	14	324	1.39	0.00
0x114E1703	88	22	400	0.44	0.00

Table A.5: L0 threshold values for the 2017 TCKs.

TCK hex	$E_T^{L0}(e)$	$p_T^{L0}(\mu)$	$p_T^{L0}(\mu_1) \cdot p_T^{L0}(\mu_2)$	% lumi MU	% lumi MD
0x517A18A4 (MC)	99	35	1296	-	-
0x11771801	99	35	1296	17.43	1.54
0x11751801	99	35	1296	0.00	27.77
0x117A18A4	99	35	1296	24.94	9.39
0x11741801	99	35	1296	16.71	9.09
0x117A18A2	99	35	1296	28.03	51.99
0x11711801	99	35	1296	0.54	0.00
0x117718A1	99	35	1296	0.04	0.00
0x11671801	99	35	1296	0.53	0.20
0x11731801	99	35	1296	11.78	0.00

Table A.6: L0 threshold values for the 2018 TCKs.

B Selections

The following section contains tables for the stripping selection and the preselection for the three described analyses. The full selection is applied to both the data and the MC simulation.

Table B.1: Requirements of the `Bu2LLK_mmLine`, `Bu2LLK_eeLine2`, and `Bu2LLK_meLine` stripping lines. When a selection is different for muons or downstream V^0 candidates, the selection is reported in parentheses. Note that on the used Monte Carlo simulation, the $p_T > 250\,\text{MeV}/c$ selection on long tracks has been removed to allow the use of `PIDCalib` for PID efficiency calibration.

Particle	**Requirement**
$e(\mu)$	$p_\text{T} > 350\,\text{MeV}/c$ $\chi^2_{IP} > 9$ DLL$e > 0$ (`isMuon`)
$e^+e^-(\mu^+\mu^-)$	$p_\text{T} > 200(0)\,\text{MeV}/c$ $m < 5000(5500)\,\text{MeV}/c^2$ $\chi^2_{vtx} < 9$ $\chi^2_{FD} > 16$ $\chi^2_\text{IP} > 0$
π	$p > 2\,\text{GeV}/c$ $p_\text{T} > 250\,\text{MeV}/c$ $\chi^2_{IP} > 9(4)$
p	$p > 2\,\text{GeV}/c$ $p_\text{T} > 250\,\text{MeV}/c$ $\chi^2_{IP} > 9(4)$
Λ/K^0_S	$\lvert m - m_{PDG}\rvert < 35(64)\,\text{MeV}/c$ $\chi^2_{vtx} < 30(25)$ $p_\text{T} > 400\,\text{MeV}/c$ $\chi^2_{FD} > 4(0)$
Λ^0_b/B^0	$\chi^2_{vtx} < 9$ $\chi^2_{IP} < 25$ DIRA > 0.9995 $\chi^2_{FD} > 100$

Description	Requirement (DD)	Requirement (LL)
$p_T^{L0}(\mu)$	—	> 36 MeV/c^2
J/ψ mass	< 50 MeV/c^2	$[3030, 3150]$ MeV/c^2
Λ mass	< 10 MeV/c^2	$[1105, 1125]$ MeV/c^2
K_S^0 mass	< 15 MeV/c^2	$[460, 530]$ MeV/c^2
Λ_b^0 mass	$[5360, 5860]$ MeV/c^2	
B^0 mass	$[5180, 5660]$ MeV/c^2	
Λ (K_S^0) τ	$[0.0005, 2]$ ns	$[0.002, 2]$ ns
Λ (K_S^0) DIRA	> 0	—
Λ (K_S^0) flight distance χ^2	> 0	> 0
Λ (K_S^0) end vertex z	$[0, 2250]$ mm	$[0, 400]$ mm
Λ_b^0 (B^0) p_T	$[4, 20]$ GeV/c^2	
Λ_b^0 (B^0) η	$[2, 5]$	
μ p	> 500 MeV/c	> 800 MeV/c
μ p_T	> 3000 MeV/c	—
DTF status	Remove candidates failing fit	

Table B.2: Preselection requirements for the $\mathcal{B}(\Lambda_b^0 \to J/\psi\,\Lambda)$ analysis. All requirements are identical for the $\Lambda_b^0 \to J/\psi\,\Lambda$ and $B^0 \to J/\psi\,(\to \mu^+\mu^-)K_S^0$ modes, with the exception of mass cuts, where the K_S^0 mass window is indicated in parentheses.

Description	Requirement ($\Lambda_b^0 \to \Lambda e^+ e^-$)	Requirement ($\Lambda_b^0 \to \Lambda \mu^+ \mu^-$)
Λ_b^0 mass	$[4720, 6400]\,\mathrm{MeV}/c^2$	$[5300, 6100]\,\mathrm{MeV}/c^2$
Λ mass	$\lvert m - m_{PDG}\rvert < 10\,\mathrm{MeV}/c^2$	
Λ τ	$[0.0005, 2]$ ns	
Λ end vertex z	$[0, 2250]$ mm	
Λ DIRA	> 0	
Λ χ^2_{FD}	> 0	
$p_T(\mu/e)$	$> 500\,\mathrm{MeV}/c$	
$p(\mu/e)$	$> 3\,\mathrm{GeV}/c$	
ProbNN PID (μ/e)	> 0.2	
$p_T(\tau)$	$> 250\,\mathrm{MeV}/c$	
$p_T(p)$	$> 250\,\mathrm{MeV}/c$	
DTF status	Remove candidates failing fit	

Table B.3: Preselection requirements for the R_Λ analysis, for both the electron and muon modes.

Description	Requirement ($\Lambda_b^0 \to \Lambda e^{\pm}\mu^{\mp}$)	Requirement ($\Lambda_b^0 \to J/\psi\,\Lambda$)
J/ψ mass	$\notin \left[\sqrt{9.0} * 1000, \sqrt{10.1} * 1000\right]$ MeV/c^2	$\lvert m - m_{PDG}\rvert < 50\,\text{MeV}/c^2$
Λ mass	$\lvert m - m_{PDG}\rvert < 10\,\text{MeV}/c^2$	
Λ_b^0 mass	$[4720, 6400]\,\text{MeV}/c^2$	
HOP	$M_{HOP}(\Lambda_b^0) > 2900 + 170 \cdot log(\chi^2_{FD}\,(\Lambda_b^0))$ MeV/c^2	-
Λ τ	$[0.0005, 2]\,\text{ns}$	
Λ end vertex z	$[0, 2250]\,\text{mm}$	
Λ DIRA	> 0	
Λ χ^2_{FD}	> 0	
$p_T(\mu/e)$	$> 500\,\text{MeV}/c$	
$p(\mu/e)$	$> 3\,\text{GeV}/c$	
ProbNN PID (μ/e)	> 0.2	
DTF status	Remove candidates failing fit	

Table B.4: Preselection requirements for the $\Lambda_b^0 \to \Lambda e^{\pm}\mu^{\mp}$ analysis, for both the signal and normalization channels.

C Efficiencies

The following section contains tables for the selection efficiencies for the $\mathcal{B}(\Lambda_b^0 \to J/\psi\,\Lambda)$ and R_Λ analyses.

C.1 Control mode: $\mathcal{B}(\Lambda_b^0 \to J/\psi\,\Lambda)$ analysis

Table C.1: Efficiency of $B^0 \to J/\psi(\to \mu^+\mu^-)K_s^0$ on events in downwards polarity MC simulation using K_S^0 reconstructed using downstream tracks.

Categories	Weighted Efficiency (%)		
	2016	2017	2018
Generator	68.05 ± 0.05	68.05 ± 0.05	68.05 ± 0.05
Stripping + rec.	6.619 ± 0.010	5.783 ± 0.014	5.495 ± 0.012
PID	94.89 ± 0.06	94.83 ± 0.09	95.45 ± 0.08
L0 trigger	73.63 ± 0.07	78.11 ± 0.11	76.15 ± 0.10
HLT1 trigger	95.02 ± 0.04	95.21 ± 0.06	95.29 ± 0.06
HLT2 trigger	96.61 ± 0.04	96.53 ± 0.05	97.00 ± 0.05
Pre-Selection	83.57 ± 0.07	83.97 ± 0.11	83.74 ± 0.10
q^2 selection	94.98 ± 0.05	94.92 ± 0.07	94.91 ± 0.07
DTF converged	99.97 ± 0.00	99.98 ± 0.00	99.98 ± 0.00
Faulty TT sensor Veto	N/A	94.57 ± 0.08	94.49 ± 0.07
Total efficiency	3.369 ± 0.007	2.967 ± 0.010	2.772 ± 0.009

Table C.2: Efficiency of $B^0 \to J/\psi(\to \mu^+\mu^-)K^0_s$ on events in downwards polarity MC simulation using K^0_S reconstructed using long tracks.

Categories	Weighted Efficiency (%)		
	2016	2017	2018
Generator	68.05 ± 0.05	68.05 ± 0.05	68.05 ± 0.05
Stripping + rec.	3.266 ± 0.007	2.828 ± 0.010	2.654 ± 0.009
PID	94.72 ± 0.08	94.70 ± 0.13	95.34 ± 0.12
L0 trigger	72.93 ± 0.10	77.67 ± 0.15	75.46 ± 0.14
HLT1 trigger	94.86 ± 0.06	95.01 ± 0.09	95.16 ± 0.08
HLT2 trigger	97.37 ± 0.04	97.38 ± 0.07	97.73 ± 0.06
Pre-Selection	79.90 ± 0.11	80.27 ± 0.17	80.51 ± 0.16
q^2 selection	94.78 ± 0.07	94.61 ± 0.11	94.77 ± 0.10
DTF converged	99.89 ± 0.01	99.90 ± 0.02	99.87 ± 0.02
Total efficiency	1.576 ± 0.005	1.460 ± 0.007	1.353 ± 0.006

Table C.3: Efficiency of $\Lambda^0_b \to J/\psi(\to \mu^+\mu^-)\Lambda^0$ events in downwards polarity MC simulation using Λ reconstructed using downstream tracks.

Categories	Weighted Efficiency (%)		
	2016	2017	2018
Generator	62.79 ± 0.06	62.79 ± 0.06	62.79 ± 0.06
Stripping + rec.	3.972 ± 0.020	3.372 ± 0.016	3.179 ± 0.015
PID	94.95 ± 0.18	94.85 ± 0.17	95.47 ± 0.17
L0 trigger	68.69 ± 0.25	73.70 ± 0.22	71.27 ± 0.23
HLT1 trigger	94.36 ± 0.14	94.34 ± 0.13	94.72 ± 0.13
HLT2 trigger	94.63 ± 0.15	94.50 ± 0.14	95.37 ± 0.13
Pre-Selection	77.21 ± 0.27	78.02 ± 0.25	78.02 ± 0.25
q^2 selection	95.10 ± 0.15	94.84 ± 0.15	94.91 ± 0.15
DTF converged	99.93 ± 0.01	99.92 ± 0.02	99.92 ± 0.02
Faulty TT sensor Veto	N/A	93.70 ± 0.17	94.18 ± 0.17
Total efficiency	1.697 ± 0.012	1.456 ± 0.010	1.362 ± 0.010

Table C.4: Efficiency of $\Lambda_b^0 \to J/\psi(\to \mu^+\mu^-)\Lambda^0$ events in downwards polarity MC simulation using Λ reconstructed using long tracks.

Categories	Weighted Efficiency (%)		
	2016	2017	2018
Generator	62.79 ± 0.06	62.79 ± 0.06	62.79 ± 0.06
Stripping + rec.	2.517 ± 0.016	2.097 ± 0.013	1.923 ± 0.012
PID	94.74 ± 0.23	94.67 ± 0.23	95.31 ± 0.23
L0 trigger	64.48 ± 0.32	69.25 ± 0.30	67.11 ± 0.30
HLT1 trigger	93.48 ± 0.20	93.63 ± 0.19	94.10 ± 0.19
HLT2 trigger	95.23 ± 0.19	94.88 ± 0.18	95.50 ± 0.17
Pre-Selection	73.52 ± 0.37	73.31 ± 0.36	74.22 ± 0.36
q^2 selection	94.59 ± 0.22	94.41 ± 0.22	94.91 ± 0.21
DTF converged	99.74 ± 0.05	99.68 ± 0.05	99.64 ± 0.06
Total efficiency	0.949 ± 0.010	0.843 ± 0.008	0.776 ± 0.008

Table C.5: Efficiency of $B^0 \to J/\psi(\to \mu^+\mu^-)K_s^0$ on events in MU polarity MC simulation using K_S^0 reconstructed using downstream tracks.

Categories	Weighted Efficiency (%)		
	2016	2017	2018
Generator	68.06 ± 0.05	68.06 ± 0.05	68.06 ± 0.05
Stripping + rec.	6.541 ± 0.010	5.748 ± 0.014	5.446 ± 0.014
PID	94.90 ± 0.06	94.86 ± 0.09	95.57 ± 0.09
L0 trigger	73.67 ± 0.07	78.33 ± 0.10	76.19 ± 0.11
HLT1 trigger	94.91 ± 0.04	95.17 ± 0.06	95.29 ± 0.06
HLT2 trigger	96.59 ± 0.04	96.56 ± 0.05	97.06 ± 0.05
Pre-Selection	83.62 ± 0.07	83.89 ± 0.11	83.72 ± 0.11
q^2 selection	94.87 ± 0.05	94.96 ± 0.07	94.93 ± 0.07
DTF converged	99.98 ± 0.00	99.97 ± 0.00	99.97 ± 0.01
Faulty TT sensor Veto	N/A	94.54 ± 0.07	94.56 ± 0.08
Total efficiency	3.325 ± 0.007	2.955 ± 0.010	2.756 ± 0.010

Table C.6: Efficiency of $B^0 \to J/\psi(\to \mu^+\mu^-)K_s^0$ on events in MU polarity MC simulation using K_S^0 reconstructed using long tracks.

Categories	Weighted Efficiency (%)		
	2016	2017	2018
Generator	68.06 ± 0.05	68.06 ± 0.05	68.06 ± 0.05
Stripping + rec.	3.264 ± 0.007	2.799 ± 0.010	2.641 ± 0.010
PID	94.73 ± 0.08	94.71 ± 0.13	95.45 ± 0.13
L0 trigger	73.19 ± 0.10	77.67 ± 0.15	75.62 ± 0.16
HLT1 trigger	94.75 ± 0.06	95.04 ± 0.09	95.12 ± 0.09
HLT2 trigger	97.47 ± 0.04	97.41 ± 0.07	97.73 ± 0.07
Pre-Selection	79.15 ± 0.11	79.21 ± 0.17	79.55 ± 0.18
q^2 selection	94.72 ± 0.07	94.61 ± 0.11	94.60 ± 0.11
DTF converged	99.90 ± 0.01	99.90 ± 0.01	99.87 ± 0.02
Total efficiency	1.566 ± 0.005	1.427 ± 0.007	1.332 ± 0.007

Table C.7: Efficiency of $\Lambda_b^0 \to J/\psi(\to \mu^+\mu^-)\Lambda^0$ events in MU polarity MC simulation using Λ reconstructed using downstream tracks.

Categories	Weighted Efficiency (%)		
	2016	2017	2018
Generator	62.73 ± 0.06	62.73 ± 0.06	62.73 ± 0.06
Stripping + rec.	3.938 ± 0.020	3.354 ± 0.017	3.144 ± 0.015
PID	94.97 ± 0.18	94.91 ± 0.18	95.59 ± 0.17
L0 trigger	68.29 ± 0.25	73.58 ± 0.22	71.51 ± 0.23
HLT1 trigger	94.40 ± 0.14	94.45 ± 0.14	94.47 ± 0.13
HLT2 trigger	94.48 ± 0.15	94.76 ± 0.14	95.53 ± 0.13
Pre-Selection	77.47 ± 0.27	78.42 ± 0.25	78.38 ± 0.25
q^2 selection	94.99 ± 0.15	94.55 ± 0.15	94.83 ± 0.15
DTF converged	99.93 ± 0.01	99.92 ± 0.02	99.90 ± 0.02
Faulty TT sensor Veto	N/A	94.52 ± 0.07	94.43 ± 0.08
Total efficiency	1.675 ± 0.012	1.553 ± 0.011	1.440 ± 0.010

Table C.8: Efficiency of $\Lambda_b^0 \to J/\psi(\to \mu^+\mu^-)\Lambda^0$ events in MU polarity MC simulation using Λ reconstructed with long tracks.

Categories	Weighted Efficiency (%)		
	2016	2017	2018
Generator	62.73 ± 0.06	62.73 ± 0.06	62.73 ± 0.06
Stripping + rec.	2.532 ± 0.016	2.068 ± 0.013	1.930 ± 0.012
PID	94.74 ± 0.23	94.73 ± 0.23	95.45 ± 0.23
L0 trigger	63.99 ± 0.32	69.15 ± 0.30	67.47 ± 0.30
HLT1 trigger	93.71 ± 0.20	93.81 ± 0.19	94.07 ± 0.19
HLT2 trigger	95.13 ± 0.19	94.96 ± 0.19	95.60 ± 0.18
Pre-Selection	73.02 ± 0.38	72.85 ± 0.37	73.09 ± 0.37
q^2 selection	94.89 ± 0.21	94.60 ± 0.22	94.82 ± 0.21
DTF converged	99.70 ± 0.06	99.80 ± 0.04	99.66 ± 0.06
Total efficiency	0.945 ± 0.010	0.830 ± 0.008	0.772 ± 0.008

C.2 Rare mode: R_Λ analysis

Table C.9: Table showing the selection efficiencies for $\Lambda_b^0 \to J/\psi(\to e^+e^-)\Lambda$ decays in the J/ψ q^2 bin using long reconstructed Λ candidates for combined magnet polarity.

Categories	Weighted Efficiency (%)		
	Run 1	2015+2016	2017+2018
Generator	18.435 ± 0.038	19.748 ± 0.051	19.703 ± 0.052
Stripping + rec.	1.901 ± 0.015	1.355 ± 0.011	1.347 ± 0.009
Tracking corr.	95.025 ± 0.000	95.838 ± 0.000	96.926 ± 0.000
Pre-Selection	33.776 ± 0.430	50.290 ± 0.468	50.648 ± 0.397
Trigger	10.076 ± 0.403	25.005 ± 0.521	21.084 ± 0.415
PID	92.833 ± 0.000	81.438 ± 0.000	78.945 ± 0.000
MVA	60.431 ± 2.013	50.083 ± 1.217	49.717 ± 1.074
q^2 selection	95.957 ± 0.949	96.926 ± 0.553	96.718 ± 0.488
Total efficiency	0.00598 ± 0.00033	0.01274 ± 0.00043	0.01043 ± 0.00033

Table C.10: Table showing the selection efficiencies for $\Lambda_b^0 \to J/\psi(\to \mu^+\mu^-)\Lambda$ decays in the J/ψ q^2 bin using long reconstructed Λ candidates for combined magnet polarity.

Categories	Weighted Efficiency (%)		
	Run 1	2015+2016	2017+2018
Generator	18.576 ± 0.039	19.839 ± 0.052	19.780 ± 0.052
Stripping + rec.	2.361 ± 0.017	2.246 ± 0.014	2.231 ± 0.012
Tracking corr.	100.334 ± 0.000	96.698 ± 0.000	97.770 ± 0.000
Pre-Selection	52.947 ± 0.404	56.744 ± 0.361	56.940 ± 0.304
Trigger	40.364 ± 0.537	52.376 ± 0.475	59.702 ± 0.406
PID	95.021 ± 0.000	93.729 ± 0.000	94.594 ± 0.000
MVA	41.680 ± 0.821	44.486 ± 0.652	36.579 ± 0.484
q^2 selection	96.731 ± 0.423	96.344 ± 0.344	96.365 ± 0.293
Total efficiency	0.03593 ± 0.00097	0.05120 ± 0.00102	0.04890 ± 0.00087

Table C.11: Table showing the selection efficiencies for $\Lambda_b^0 \to \psi(2S)(\to e^+e^-)\Lambda$ decays in the $\psi(2S)$ q^2 bin using long reconstructed Λ candidates for combined magnet polarity.

Categories	Weighted Efficiency (%)		
	Run 1	2015+2016	2017+2018
Generator	18.179 ± 0.040	19.432 ± 0.051	19.442 ± 0.052
Stripping + rec.	2.209 ± 0.016	1.669 ± 0.012	1.661 ± 0.010
Tracking corr.	95.202 ± 0.000	96.277 ± 0.000	97.088 ± 0.000
Pre-Selection	31.725 ± 0.359	46.048 ± 0.385	46.626 ± 0.325
Trigger	12.227 ± 0.387	27.962 ± 0.461	24.160 ± 0.372
PID	92.700 ± 0.000	81.005 ± 0.000	78.114 ± 0.000
MVA	59.715 ± 1.617	49.776 ± 0.966	48.266 ± 0.851
q^2 selection	88.471 ± 1.301	89.710 ± 0.793	90.520 ± 0.673
Total efficiency	0.00716 ± 0.00033	0.01454 ± 0.00041	0.01207 ± 0.00032

Table C.12: Table showing the selection efficiencies for $\Lambda_b^0 \to \psi(2S)(\to \mu^+\mu^-)\Lambda$ decays in the $\psi(2S)$ q^2 bin using long reconstructed Λ candidates for combined magnet polarity.

Categories	Weighted Efficiency (%)		
	Run 1	2015+2016	2017+2018
Generator	18.285 ± 0.039	19.512 ± 0.051	19.578 ± 0.052
Stripping + rec.	2.758 ± 0.018	2.635 ± 0.015	2.626 ± 0.013
Tracking corr.	100.084 ± 0.000	97.214 ± 0.000	98.067 ± 0.000
Pre-Selection	51.906 ± 0.350	55.051 ± 0.310	55.404 ± 0.261
Trigger	50.950 ± 0.475	57.071 ± 0.406	63.896 ± 0.341
PID	95.131 ± 0.000	93.719 ± 0.000	94.635 ± 0.000
MVA	44.678 ± 0.643	49.455 ± 0.531	41.961 ± 0.410
q^2 selection	95.756 ± 0.373	95.448 ± 0.299	95.579 ± 0.251
Total efficiency	0.05424 ± 0.00114	0.06931 ± 0.00110	0.06774 ± 0.00096

Table C.13: Table showing the selection efficiencies for $\Lambda_b^0 \to \psi(2S)(\to e^+e^-)\Lambda$ decays in the $\psi(2S)$ q^2 bin using downstream reconstructed Λ candidates for combined magnet polarity.

Categories	Weighted Efficiency (%)		
	Run 1	2015+2016	2017+2018
Generator	18.179 ± 0.040	19.432 ± 0.051	19.442 ± 0.052
Stripping + rec.	2.622 ± 0.018	2.348 ± 0.014	2.401 ± 0.012
Tracking corr.	96.311 ± 0.020	97.621 ± 0.020	98.326 ± 0.020
Pre-Selection	53.149 ± 0.365	60.524 ± 0.326	61.636 ± 0.271
Trigger	12.634 ± 0.280	28.708 ± 0.346	25.378 ± 0.278
PID	92.957 ± 0.020	81.669 ± 0.020	79.021 ± 0.020
MVA	48.906 ± 1.142	42.955 ± 0.700	41.370 ± 0.589
q^2 selection	91.917 ± 0.833	91.833 ± 0.544	91.510 ± 0.481
Total efficiency	0.01292 ± 0.00044	0.02478 ± 0.00054	0.02149 ± 0.00043

Table C.14: Table showing the selection efficiencies for $\Lambda_b^0 \to \psi(2S)(\to \mu^+\mu^-)\Lambda$ decays in the $\psi(2S)$ q^2 bin using downstream reconstructed Λ candidates for combined magnet polarity.

Categories	Weighted Efficiency (%)		
	Run 1	2015+2016	2017+2018
Generator	18.285 ± 0.039	19.512 ± 0.051	19.578 ± 0.052
Stripping + rec.	4.214 ± 0.023	3.974 ± 0.019	4.053 ± 0.016
Tracking corr.	100.874 ± 0.020	98.368 ± 0.020	98.878 ± 0.020
Pre-Selection	65.111 ± 0.275	64.870 ± 0.247	66.087 ± 0.204
Trigger	50.480 ± 0.348	56.426 ± 0.312	62.648 ± 0.259
PID	95.393 ± 0.020	94.067 ± 0.020	94.824 ± 0.020
MVA	46.317 ± 0.474	52.140 ± 0.405	49.051 ± 0.312
q^2 selection	95.826 ± 0.263	95.425 ± 0.220	95.350 ± 0.177
Total efficiency	0.10805 ± 0.00165	0.13012 ± 0.00157	0.14407 ± 0.00147

D Invariant mass fit shapes

D.1 Double-sided Crystal Ball

The double-sided Crystal Ball function [66] consists of a Gaussian core connected with an exponential tail on each side:

$$N \begin{cases} \left(\frac{n_l}{\alpha_l}\right)^{n_l} \exp\left[-\frac{\alpha_l^2}{2}\right] \left(-\frac{m-\mu}{\sigma} + \frac{n_l}{\alpha_l} - \alpha_l\right)^{-n_l}, & \text{if } \frac{m-\mu}{\sigma} < -\alpha_l \\ \left(\frac{n_r}{\alpha_r}\right)^{n_r} \exp\left[-\frac{\alpha_r^2}{2}\right] \left(\frac{m-\mu}{\sigma} + \frac{n_r}{\alpha_r} - \alpha_r\right)^{-n_r}, & \text{if } \frac{m-\mu}{\sigma} > \alpha_r \\ \exp\left[-\frac{(m-\mu)^2}{2\sigma^2}\right], & \text{otherwise,} \end{cases} \tag{D.1}$$

where μ and σ are the mean and resolution of the Gaussian core; α_r and α_l describe the starting points of tails, and n_r and n_l describe the slopes of the tails.

D.2 Hypatia

The Hypatia function [73] based on the double-sided Crystall Ball, but takes into account the per-event mass uncertainties:

$$f \begin{cases} \frac{G(\mu-\alpha_l\sigma;\mu,\sigma,\lambda,\zeta,\beta)}{\left(1-m/\left(n\frac{G(\mu-\alpha_l\sigma;\mu,\sigma,\lambda,\zeta,\beta)}{G'(\mu-\alpha_l\sigma;\mu,\sigma,\lambda,\zeta,\beta)}-\alpha_l\sigma\right)\right)^{n_l}}, & \text{if } \frac{m-\mu}{\sigma} \leq -\alpha_l \\ \frac{G(\mu-\alpha_r\sigma;\mu,\sigma,\lambda,\zeta,\beta)}{\left(1-m/\left(n\frac{G(\mu-\alpha_r\sigma;\mu,\sigma,\lambda,\zeta,\beta)}{G'(\mu-\alpha_r\sigma;\mu,\sigma,\lambda,\zeta,\beta)}-\alpha_r\sigma\right)\right)^{n_r}}, & \text{if } \frac{m-\mu}{\sigma} \geq \alpha_r \\ G(m;\mu,\sigma,\lambda,\zeta,\beta), & \text{otherwise,} \end{cases} \tag{D.2}$$

where α_r (α_l), and n_r and n_l describe the exponential tails, G' is the derivative of G with respect to m, which is the hyperbolic core, given by

$$G \propto \left[(m-\mu)^2 + A_\lambda^2(\zeta)\sigma^2\right]^{\frac{1}{2}\lambda-\frac{1}{4}} e^{\beta(m-\mu)} \times K_{\lambda-\frac{1}{2}}\left(\zeta\sqrt{1+\left(\frac{m-\mu}{A_\lambda(\zeta)\sigma}\right)^2}\right) \tag{D.3}$$

where K_λ are special Bessel functions of the third kind and $A_\lambda^2 = \frac{\zeta K_\lambda(\zeta)}{K_{\lambda+1}(\zeta)}$.

D.3 Johnson S_U

The Johnson S_U function [67] is a four-parameter distribution that is defined as

$$f(m;\gamma,\delta,\xi,\lambda) \propto \frac{\delta}{\sqrt{2\pi}}\frac{1}{m(1-m)}\exp\left[-\frac{1}{2}\left(\gamma+\delta\sinh^{-1}\left(\frac{m-\xi}{\lambda}\right)\right)^2\right] \tag{D.4}$$

where γ and δ are the location and scale parameters, ξ is the shape parameter, and λ is the shape parameter.

E Invariant mass fits

The following section contains all the invariant mass likelihood fits for the $\mathcal{B}(\Lambda_b^0 \to J/\psi\,\Lambda)$ and R_Λ analyses.

E.1 Control mode: $\mathcal{B}(\Lambda_b^0 \to J/\psi\,\Lambda)$ analysis

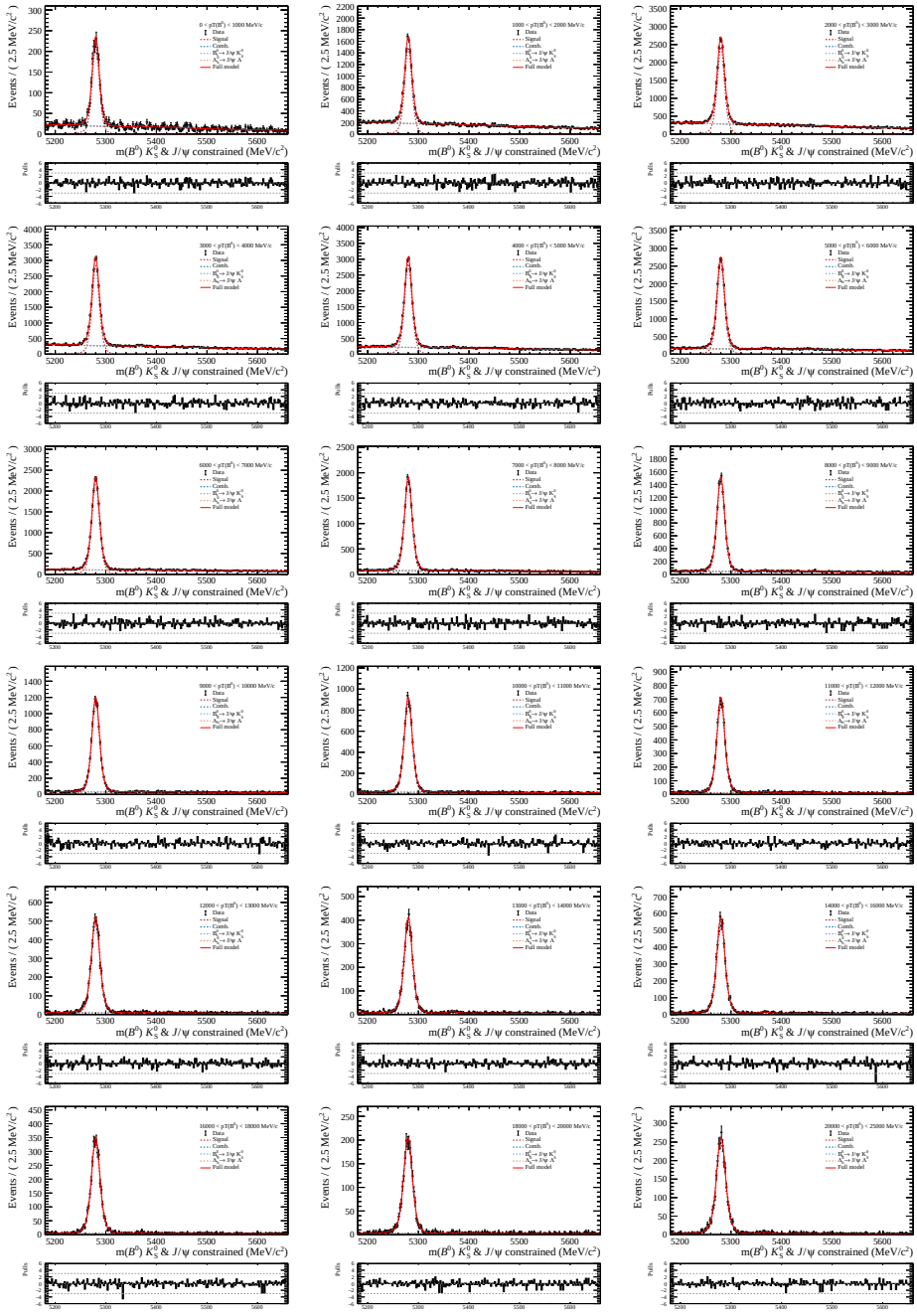

Figure E.1: Invariant mass fits for $B^0 \to J/\psi(\to \mu^+\mu^-)K^0_S$ decays in bins of the b-hadron p_T for downstream reconstructed K^0_S candidates.

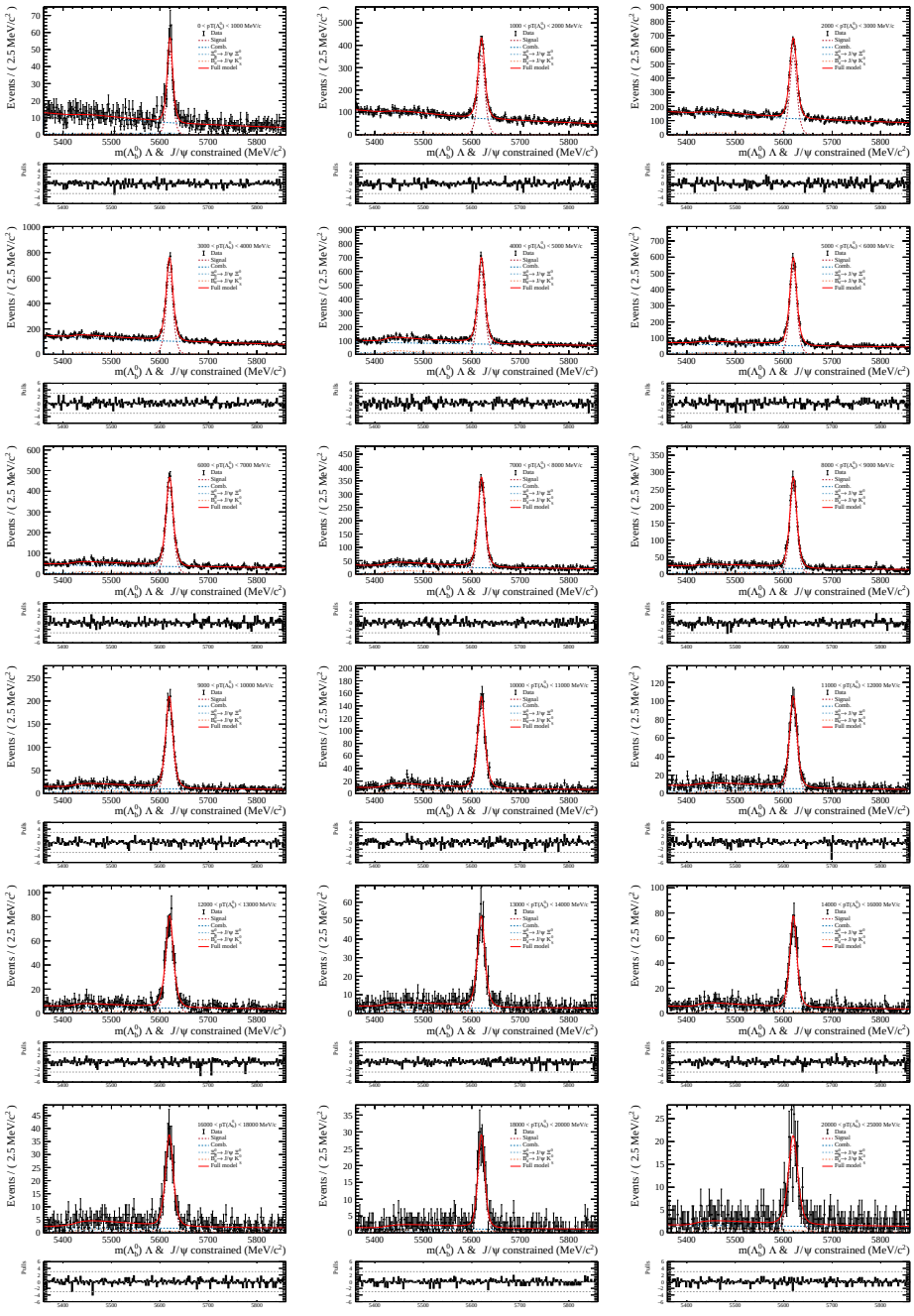

Figure E.2: Invariant mass fits for $\Lambda_b^0 \to J/\psi(\to \mu^+\mu^-)\Lambda$ decays in bins of the b-hadron p_T for downstream reconstructed Λ hadrons.

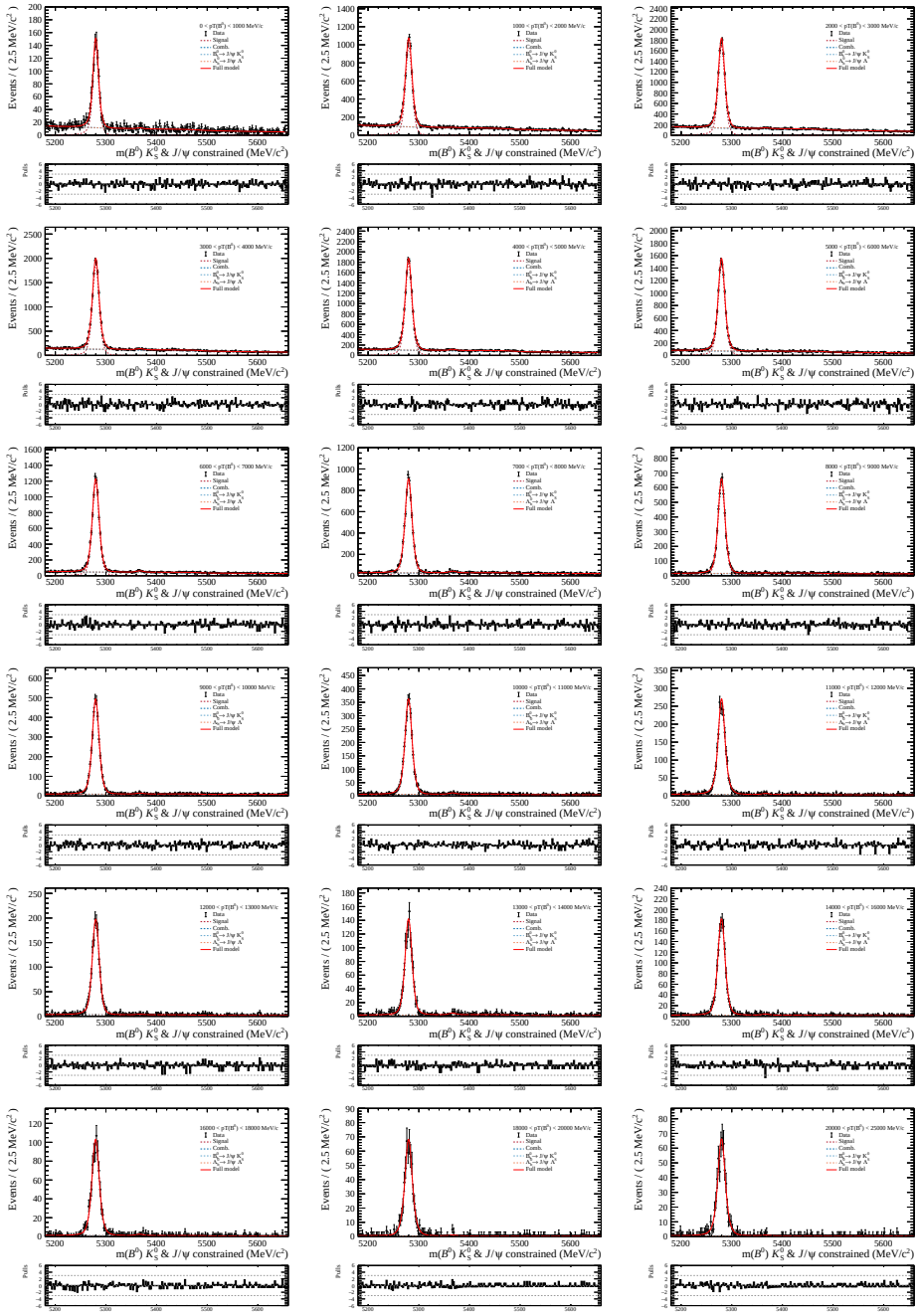

Figure E.3: Invariant mass fits for $B^0 \to J/\psi(\to \mu^+\mu^-)K^0_S$ decays in bins of the b-hadron p_T for long track reconstructed K^0_S candidates.

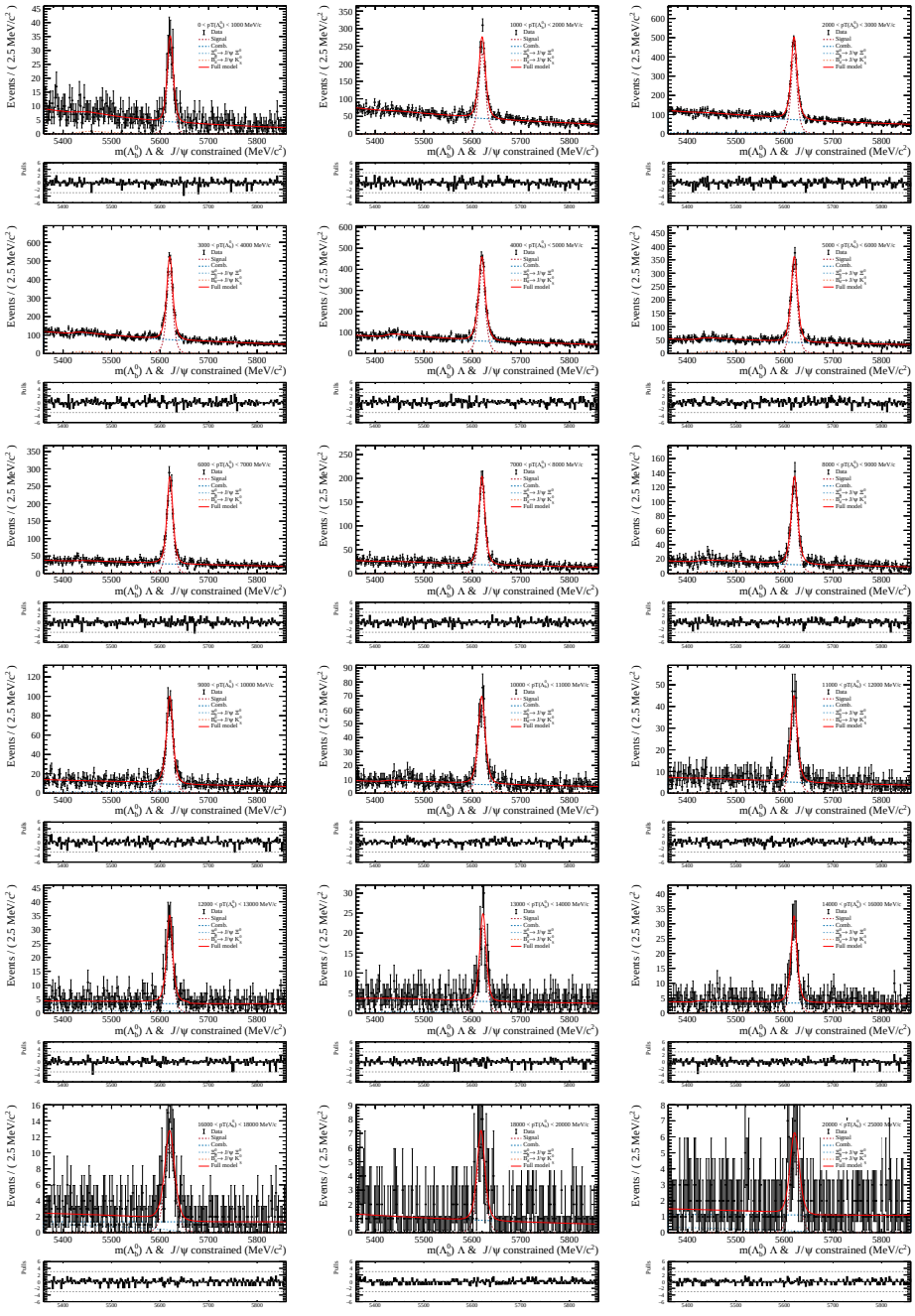

Figure E.4: Invariant mass fits for $\Lambda_b^0 \to J/\psi(\to \mu^+\mu^-)\Lambda$ decays in bins of the b-hadron p_T for long track reconstructed Λ hadrons.

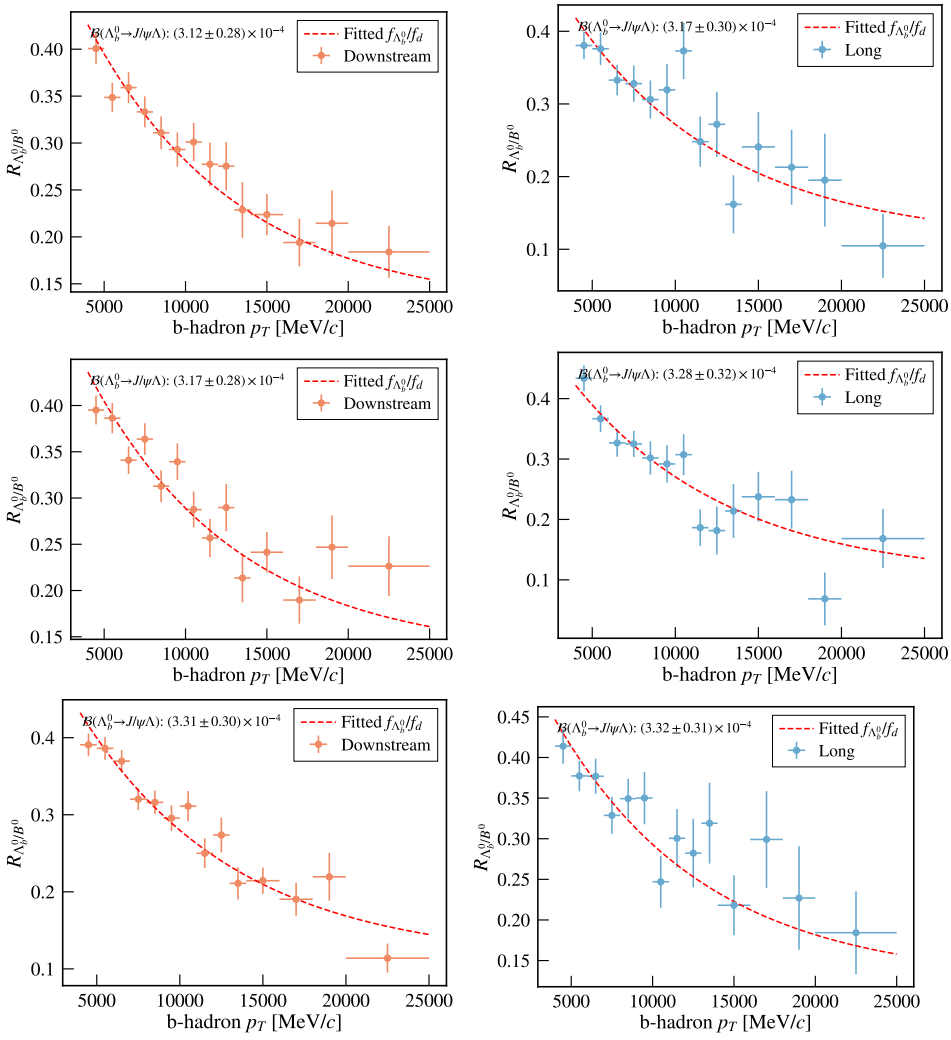

Figure E.5: The measured $\Lambda_b^0 \to J/\psi(\to \mu^+\mu^-)\Lambda$/ $B^0 \to J/\psi(\to \mu^+\mu^-)K_S^0$ efficiency corrected yield ratio in bins of b-hadron p_T for the 2016, 2017 and 2018 datasets using downstream (left) and long (right) reconstructed K_S^0 and Λ candidates.

E.2 Rare mode: R_Λ analysis

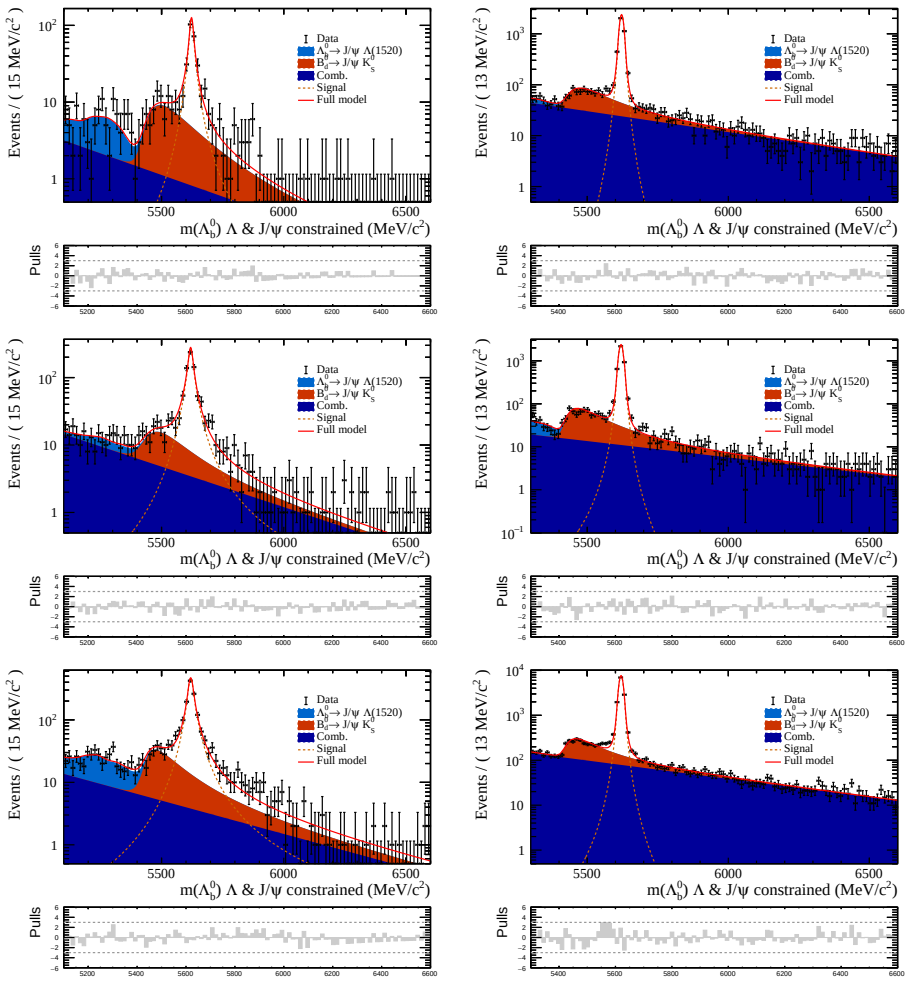

Figure E.6: Maximum likelihood invariant mass fits for the $\Lambda_b^0 \to J/\psi(\to e^+e^-)\Lambda$ (left) and $\Lambda_b^0 \to J/\psi(\to \mu^+\mu^-)\Lambda$ (right) candidates using downstream reconstructed Λ candidates using the Run 1 (top), 2015+2016 (middle), and 2017+2018 (bottom) data samples. The red line shows the total fit model, the orange dotted line the fitted signal, the dark blue filled area the combinatorial background, the red filled area the mis-identified background, and the light blue filled area the partially reconstructed background.

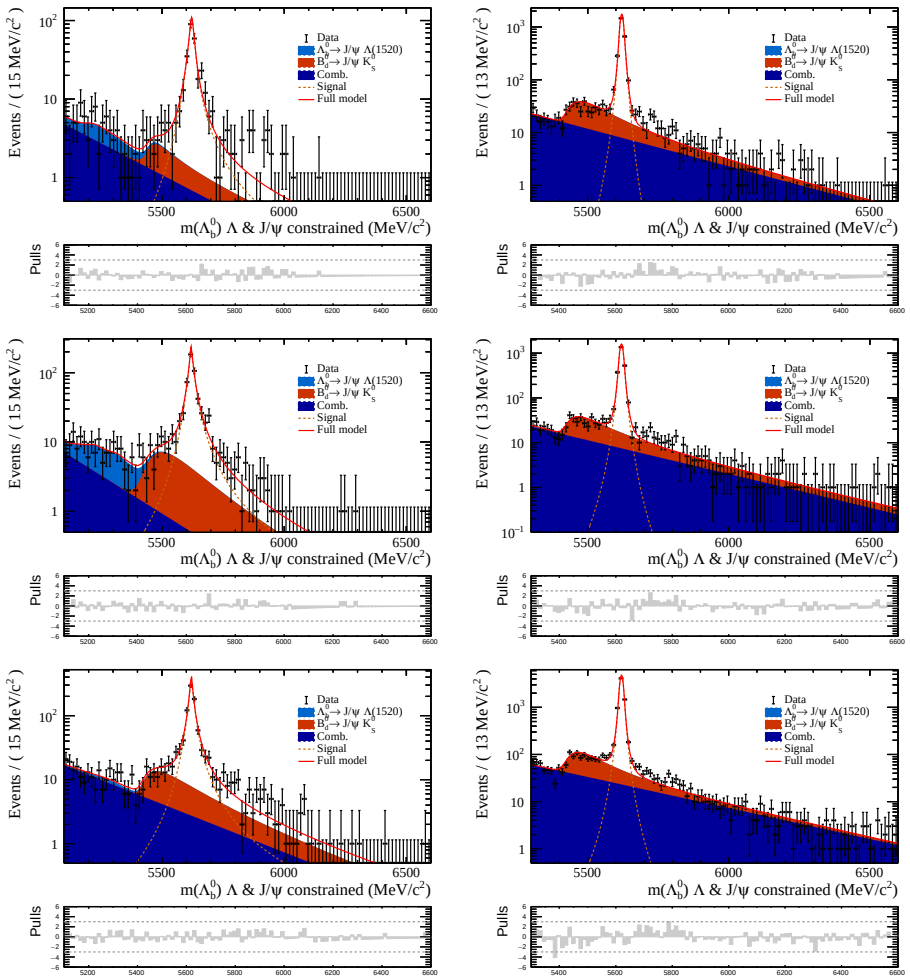

Figure E.7: Maximum likelihood invariant mass fits for the $\Lambda_b^0 \to J/\psi(\to e^+e^-)\Lambda$ (left) and $\Lambda_b^0 \to J/\psi(\to \mu^+\mu^-)\Lambda$ (right) candidates using long reconstructed Λ candidates using the Run 1 (top), 2015+2016 (middle), and 2017+2018 (bottom) data samples. The red line shows the total fit model, the orange dotted line the fitted signal, the dark blue filled area the combinatorial background, the red filled area the mis-identified background, and the light blue filled area the partially reconstructed background.

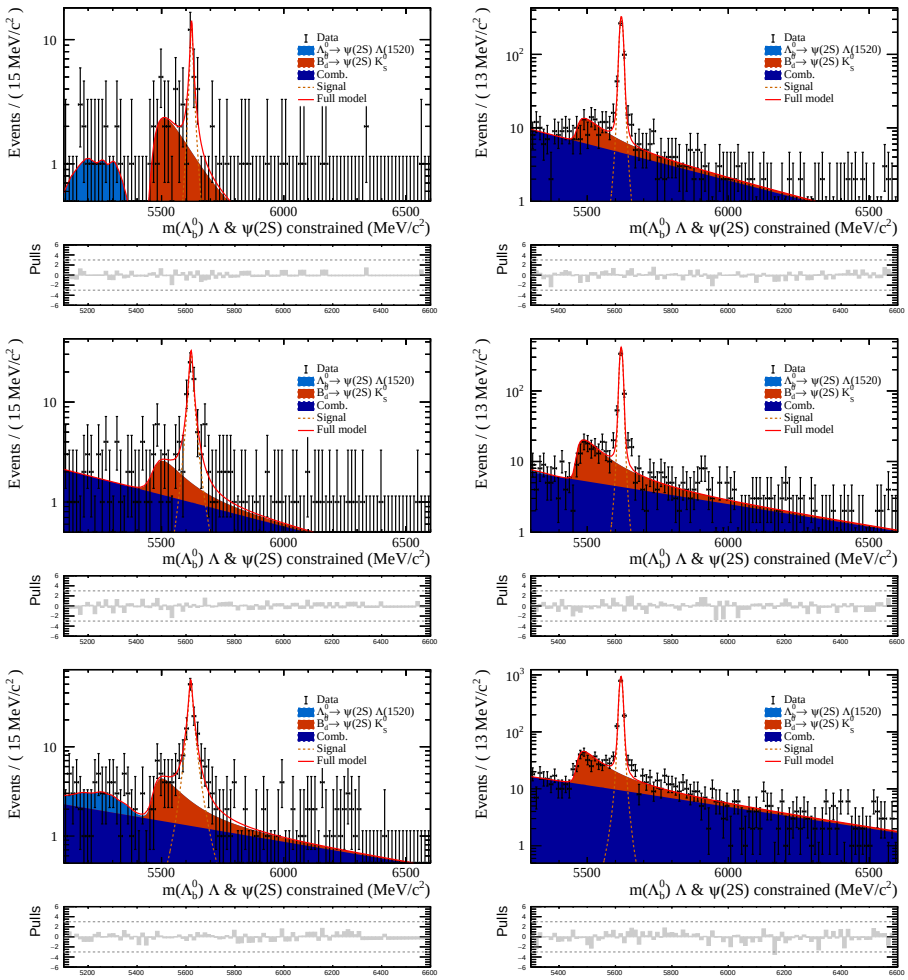

Figure E.8: Maximum likelihood invariant mass fits for the $\Lambda_b^0 \to \psi(2S)(\to e^+e^-)\Lambda$ (left) and $\Lambda_b^0 \to \psi(2S)(\to \mu^+\mu^-)\Lambda$ (right) candidates using downstream reconstructed Λ candidates using the Run 1 (top), 2015+2016 (middle), and 2017+2018 (bottom) data samples.. The red line shows the total fit model, the orange dotted line the fitted signal, the dark blue filled area the combinatorial background, the red filled area the mis-identified background, and the light blue filled area the partially reconstructed background.

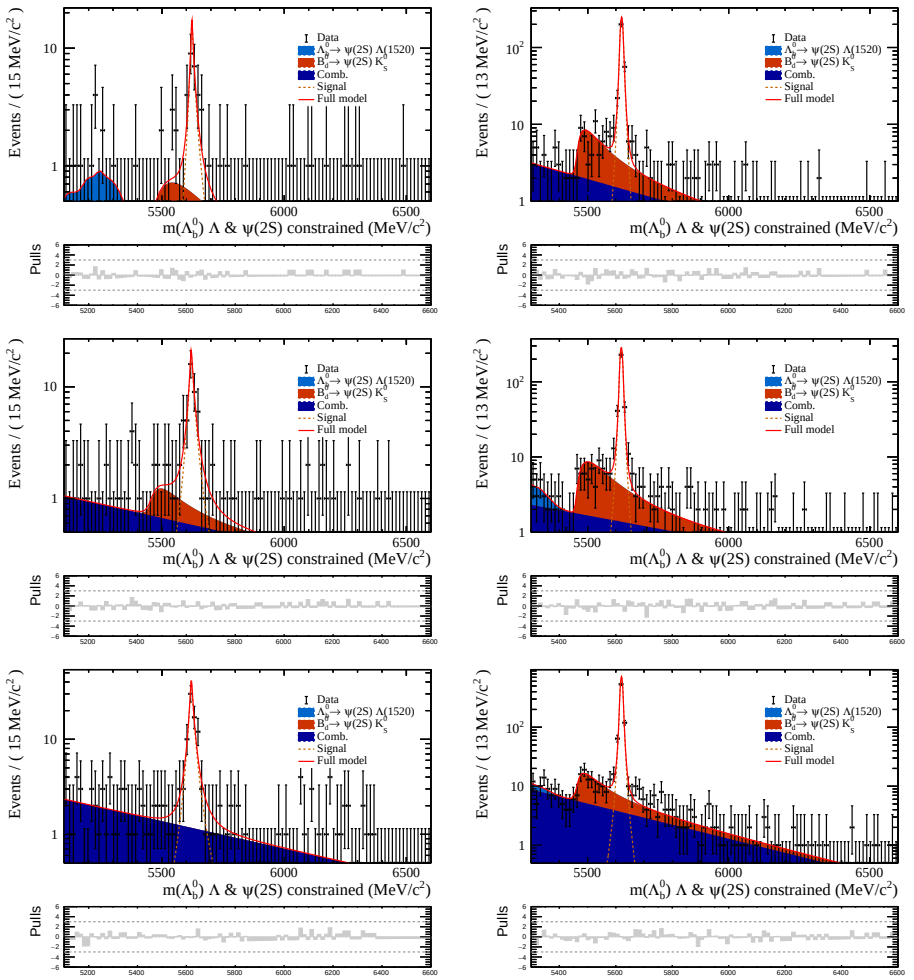

Figure E.9: Maximum likelihood invariant mass fits for the $\Lambda_b^0 \to \psi(2S)(\to e^+e^-)\Lambda$ (left) and $\Lambda_b^0 \to \psi(2S)(\to \mu^+\mu^-)\Lambda$ (right) candidates using long reconstructed Λ candidates using the Run 1 (top), 2015+2016 (middle), and 2017+2018 (bottom) data samples.. The red line shows the total fit model, the orange dotted line the fitted signal, the dark blue filled area the combinatorial background, the red filled area the mis-identified background, and the light blue filled area the partially reconstructed background.

Period	DD	LL
Run 1	278 ± 21	269 ± 21
15+16	704 ± 33	488 ± 28
17+18	1350 ± 43	786 ± 36

Table E.1: Signal yields for the $\Lambda_b^0 \to J/\psi(\to e^+e^-)\Lambda$ invariant mass fits.

Period	DD	LL
Run 1	2481 ± 51	1775 ± 43
15+16	3883 ± 64	2345 ± 50
17+18	8554 ± 95	4223 ± 67

Table E.2: Signal yields for the $\Lambda_b^0 \to J/\psi(\to \mu^+\mu^-)\Lambda$ invariant mass fits.

Period	DD	LL
Run 1	20 ± 5	21 ± 6
15+16	48 ± 9	38 ± 7
17+18	118 ± 12	76 ± 11

Table E.3: Signal yields for the $\Lambda_b^0 \to \psi(2S)(\to e^+e^-)\Lambda$ invariant mass fits.

Period	DD	LL
Run 1	270 ± 17	183 ± 14
15+16	331 ± 19	245 ± 16
17+18	795 ± 29	484 ± 22

Table E.4: Signal yields for the $\Lambda_b^0 \to \psi(2S)(\to \mu^+\mu^-)\Lambda$ invariant mass fits.

Bibliography

[1] S. L. Glashow, *Partial-symmetries of weak interactions*, Nuclear Physics **22** (1961) 579.

[2] S. Weinberg, *A model of leptons*, Phys. Rev. Lett. **19** (1967) 1264.

[3] A. Salam, *Weak and Electromagnetic Interactions*, Conf. Proc. C **680519** (1968) 367.

[4] V. Trimble, *Existence and nature of dark matter in the universe*, Annual Review of Astronomy and Astrophysics **25** (1987) 425, arXiv:https://doi.org/10.1146/annurev.aa.25.090187.002233.

[5] P. W. Higgs, *Broken symmetries and the masses of gauge bosons*, Phys. Rev. Lett. **13** (1964) 508.

[6] N. Cabibbo, *Unitary symmetry and leptonic decays*, Phys. Rev. Lett. **10** (1963) 531.

[7] M. Kobayashi and T. Maskawa, *CP-Violation in the Renormalizable Theory of Weak Interaction*, Progress of Theoretical Physics **49** (1973) 652.

[8] W. Detmold and S. Meinel, $\Lambda_b \to \Lambda \ell^+ \ell^-$ *form factors, differential branching fraction, and angular observables from lattice qcd with relativistic b quarks*, Phys. Rev. D **93** (2016) 074501.

[9] C. D. Froggatt and H. B. Nielsen, *Hierarchy of quark masses, cabibbo angles and cp violation*, Nuclear Physics B **147** (1979) 277.

[10] D. Bečirević, S. Fajfer, N. Košnik, and O. Sumensari, *Leptoquark model to explain the b-physics anomalies, R_K and R_D*, Phys. Rev. D **94** (2016) 115021.

[11] M. Bordone, M. Rahimi, and K. K. Vos, *Lepton flavour violation in rare Λ_b^0 decays*, The European Physical Journal C **81** (2021) .

[12] T. Blake and M. Kreps, *Angular distribution of polarised Λ_b^0 baryons decaying to $\Lambda\ell^+\ell^-$*, Journal of High Energy Physics **2017** (2017) .

[13] A. Snoch. Personal communication, 2023.

[14] G. Buchalla, A. J. Buras, and M. E. Lautenbacher, *Weak decays beyond leading logarithms*, Reviews of Modern Physics **68** (1996) 1125.

[15] T. Feldmann, *Introduction to operator product expansion*, 2008. Talk at Neckarzimmern Workshop.

[16] M. Algueró *et al.*, *To (b)e or not to (b)e: no electrons at LHCb*, The European Physical Journal C **83** (2023) .

[17] B. Capdevila, *Status of the global $b \to s\ell\ell$ fits*, 21st Conference on Flavour Physics and CP Violation, 2023.

[18] L. Evans and P. Bryant, *LHC Machine*, JINST **3** (2008) S08001.

[19] J. Haffner, *The CERN accelerator complex. Complexe des accélérateurs du CERN* OPEN-PHO-ACCEL-2013-056, 2013. General Photo.

[20] LHCb collaboration, *LHCb reoptimized detector design and performance: Technical Design Report*, CERN-LHCC-2003-030, 2003.

[21] LHCb collaboration, R. Aaij *et al.*, *Measurement of the track reconstruction efficiency at LHCb*, Journal of Instrumentation **10** (2015) P02007.

[22] LHCb collaboration, R. Aaij *et al.*, *Performance of the LHCb Vertex Locator*, JINST **9** (2014) P09007 LHCB-DP-2014-001.

[23] LHCb collaboration, A. Affolder *et al.*, *Radiation damage in the LHCb vertex locator*, Journal of Instrumentation **8** (2013) P08002.

[24] LHCb collaboration, G. A. Cowan, *Performance of the LHCb silicon tracker*, Nucl. Instrum. Meth. **A699** (2013) 156.

[25] D. van Eijk *et al.*, *Radiation hardness of the LHCb Outer Tracker*, Nuclear Instruments and Methods in Physics Research Section A: Accelerators, Spectrometers, Detectors and Associated Equipment **685** (2012) 62.

[26] LHCb collaboration, *LHCb detector performance*, International Journal of Modern Physics A **30** (2015) 1530022.

[27] LHCb collaboration, M. Adinolfi *et al.*, *Performance of the LHCb RICH detector at the LHC*, Eur. Phys. J. **C73** (2013) 2431 LHCb-DP-2012-003.

[28] M. Mulder, *The essence of rare beauty*, PhD thesis, Rijksuniversiteit Groningen, 2020, Presented 15 Jan 2021.

[29] LHCb collaboration, R. Aaij *et al.*, *The LHCb trigger and its performance in 2011*, JINST **8** (2013) P04022 LHCb-DP-2012-004.

[30] LHCb collaboration, R. Aaij *et al.*, *Performance of the LHCb trigger and full real-time reconstruction in Run 2 of the LHC*, JINST **14** (2019) P04013.

[31] T. Sjöstrand, S. Mrenna, and P. Skands, *A brief introduction to PYTHIA 8.1*, Comput. Phys. Commun. **178** (2008) 852.

[32] T. Sjöstrand, S. Mrenna, and P. Skands, *PYTHIA 6.4 physics and manual*, JHEP **05** (2006) 026.

[33] I. Belyaev *et al.*, *Handling of the generation of primary events in Gauss, the LHCb simulation framework*, J. Phys. Conf. Ser. **331** (2011) 032047.

[34] D. J. Lange, *The EvtGen particle decay simulation package*, Nucl. Instrum. Meth. **A462** (2001) 152.

[35] P. Golonka and Z. Was, *PHOTOS Monte Carlo: A precision tool for QED corrections in Z and W decays*, Eur. Phys. J. **C45** (2006) 97.

[36] Geant4 collaboration, J. Allison *et al.*, *Geant4 developments and applications*, IEEE Trans. Nucl. Sci. **53** (2006) 270.

[37] Geant4 collaboration, S. Agostinelli *et al.*, *Geant4: A simulation toolkit*, Nucl. Instrum. Meth. **A506** (2003) 250.

[38] M. Clemencic *et al.*, *The LHCb simulation application, Gauss: Design, evolution and experience*, J. Phys. Conf. Ser. **331** (2011) 032023.

[39] LHCb collaboration, R. Aaij *et al.*, *Differential branching fractions and isospin asymmetries of* $B \to K^{(*)}\mu^+\mu^-$ *decays*, JHEP **06** (2014) 133.

[40] LHCb collaboration, R. Aaij et al. , *Branching Fraction Measurements of the Rare $B_s^0 \to \phi\mu^+\mu^-$ and $B_s^0 \to f_2'(1525)\mu^+\mu^-$ Decays*, Phys. Rev. Lett. **127** (2021) 151801.

[41] LHCb collaboration, R. Aaij et al. , *Angular Analysis of the $B^+ \to K^{*+}\mu^+\mu^-$ Decay*, Phys. Rev. Lett. **126** (2021) 161802.

[42] LHCb collaboration, R. Aaij et al. , *Angular analysis of the rare decay $B_s^0 \to \phi\mu^+\mu^-$*, Journal of High Energy Physics **2021** (2021) .

[43] LHCb collaboration, R. Aaij et al. , *Tests of Lepton Universality Using $B^0 \to K_S^0\ell^+\ell^-$ and $B^+ \to K^{*+}\ell^+\ell^-$ Decays*, Phys. Rev. Lett. **128** (2022) 191802.

[44] LHCb collaboration, R. Aaij et al. , *Measurement of lepton universality parameters in $B^+ \to K^+\ell^+\ell^-$ and $B^0 \to K^{*0}\ell^+\ell^-$ decays*, Phys. Rev. D **108** (2023) 032002.

[45] LHCb collaboration, R. Aaij et al. , *Test of lepton universality in $b \to s\ell^+\ell^-$ decays*, Phys. Rev. Lett. **131** (2023) 051803, `arXiv:2212.09152`.

[46] LHCb collaboration, R. Aaij *et al.*, *Test of lepton universality using $\Lambda_b^0 \to pK^-\ell^+\ell^-$ decays*, JHEP **05** (2020) 040 LHCb-PAPER-2019-040 CERN-EP-2019-272.

[47] LHCb collaboration, R. Aaij *et al.*, *Differential branching fraction and angular analysis of $\Lambda_b^0 \to \Lambda\mu^+\mu^-$ decays*, JHEP **06** (2015) 115, Erratum ibid. **09** (2018) 145.

[48] D0 collaboration, V. M. Abazov *et al.*, *Measurement of the production fraction times branching fraction $f(b \to \Lambda_b) \cdot \mathcal{B}(\Lambda_b \to J/\psi\Lambda)$*, Phys. Rev. D **84** (2011) 031102.

[49] P. N. Swallow, *Searching for Charged Lepton Flavour Violation at LHCb and Long-Lived Particles with CODEX-b*, PhD thesis, University of Birmingham, 2023.

[50] LHCb collaboration, R. Aaij *et al.*, *Measurement of b-hadron fractions in 13 TeV pp collisions*, Phys. Rev. **D100** (2019) 031102(R).

[51] Particle Data Group, R. L. Workman and Others, *Review of Particle Physics*, PTEP **2022** (2022) 083C01.

[52] A. L. Read, *Presentation of search results: the cls technique*, Journal of Physics G: Nuclear and Particle Physics **28** (2002) 2693.

[53] LHCb collaboration, R. Aaij *et al.*, *Search for the lepton-flavour violating decays* $B^0_{(s)} \to e^\pm \mu^\mp$, JHEP **03** (2018) 078.

[54] LHCb collaboration, R. Aaij *et al.*, *Search for the lepton-flavour violating decays* $B^+ \to K^+ \mu^\pm e^\mp$, Phys. Rev. Lett. **123** (2019) 231802.

[55] LHCb collaboration, R. Aaij *et al.*, *Search for the lepton-flavour violating decays* $B^0 \to K^{*0} \mu^\pm e^\mp$ *and* $B^0_s \to \phi \mu^\pm e^\mp$, JHEP **06** (2023) 073.

[56] LHCb collaboration, R. Antunes-Nobrega *et al.*, *LHCb reoptimized detector design and performance: Technical Design Report*, Technical design report. LHCb, CERN, Geneva, 2003.

[57] LHCb collaboration, R. Aaij *et al.*, *Angular moments of the decay* $\Lambda^0_b \to \Lambda \mu^+ \mu^-$ *at low hadronic recoil*, JHEP **09** (2018) 146.

[58] L. Anderlini *et al.*, *The PIDCalib package* , CERN, Geneva, 2016.

[59] F. Archilli *et al.*, *Search for the* $B^0 \to \mu^+ \mu^-$ *decay and measurement of the* $B^0_s \to \mu^+ \mu^-$ *branching fraction and effective lifetime*, LHCb-ANA-2016-038, CERN, Geneva, 2016.

[60] LHCb collaboration, R. Aaij *et al.*, *Measurement of the track reconstruction efficiency at LHCb*, JINST **10** (2015) P02007, `arXiv:1408.1251`.

[61] LHCb collaboration, R. Aaij *et al.*, *Measurement of the electron reconstruction efficiency at lhcb*, Journal of Instrumentation **14** (2019) P11023.

[62] S. Tolk, J. Albrecht, F. Dettori, and A. Pellegrino, *Data driven trigger efficiency determination at LHCb*, LHCb-PUB-2014-039, 2014.

[63] S. Ferreres Solé, *The beauty of the rare*, PhD thesis, Maastricht University, 2022, doi: 10.26481/dis.20221219ss.

[64] A. Rogozhnikov, *Reweighting algorithms*, `https://arogozhnikov.github.io/hep_ml/reweight.html`, 2020. Accessed: 12-03-2023.

[65] M. Pivk and F. R. Le Diberder, *sPlot: A statistical tool to unfold data distributions*, Nucl. Instrum. Meth. **A555** (2005) 356.

[66] T. Skwarnicki, *A study of the radiative cascade transitions between the Upsilon-prime and Upsilon resonances*, PhD thesis, Institute of Nuclear Physics, Krakow, 1986, DESY-F31-86-02.

[67] N. L. Johnson, *Systems of frequency curves generated by methods of translation*, Biometrika **36** (1949) 149.

[68] J. H. Friedman, *Greedy function approximation: A gradient boosting machine.*, The Annals of Statistics **29** (2001) 1189 .

[69] D. Y. Ignatov and A. D. Ignatov, *Decision stream: Cultivating deep decision trees*, CoRR **abs/1704.07657** (2017) `arXiv:1704.07657`.

[70] P. Refaeilzadeh, L. Tang, and H. Liu, in *Cross-Validation*, L. LIU and M. T. ÖZSU, eds., pp. 532–538, Springer US, Boston, MA, 2009.

[71] G. Punzi, *Sensitivity of searches for new signals and its optimization*, eConf **C030908** (2003) MODT002, `arXiv:physics/0308063`.

[72] B. Storaci and P. Rennee Pais, *ST News (LHCb internal)*, Talk at LHCb week `https://indico.cern.ch/event/684379/contributions/2805734/attachments/1569321/2474729/ST_news_04dec17.pdf`, 2017.

[73] D. M. Santos and F. Dupertuis, *Mass distributions marginalized over per-event errors*, Nuclear Instruments and Methods in Physics Research Section A: Accelerators, Spectrometers, Detectors and Associated Equipment **764** (2014) 150.

[74] L. M. Garcia, L. Henry, B. Kishor, and A. Oyanguren, *Tracking performance for long-lived particles at LHCb*, Journal of Physics: Conference Series **1525** (2020) 012095.

[75] LHCb collaboration, M. Alexander *et al.*, *Mapping the material in the LHCb vertex locator using secondary hadronic interactions*, JINST **13** (2018) P06008.

[76] C.-H. Chou, H.-H. Shih, S.-C. Lee, and H.-n. Li, $\Lambda_b \to \Lambda J/\psi$ *decay in perturbative QCD*, Phys. Rev. D **65** (2002) 074030.

[77] Z.-T. Wei, H.-W. Ke, and X.-Q. Li, *Evaluating decay rates and asymmetries of* Λ_b *into light baryons in the light-front quark model*, Phys. Rev. D **80** (2009) 094016.

[78] T. Blake, S. Meinel, and D. van Dyk, *Bayesian Analysis of $b \to s\mu^+\mu^-$ Wilson Coefficients using the Full Angular Distribution of $\Lambda_b \to \Lambda(\to p\pi^-)\mu^+\mu^-$ Decays*, Phys. Rev. D **101** (2020) 035023, arXiv:1912.05811.

[79] K. Cranmer, *Kernel estimation in high-energy physics*, Computer Physics Communications **136** (2001) 198.

[80] LHCb collaboration, *Framework TDR for the LHCb Upgrade: Technical Design Report*, CERN-LHCC-2012-007, 2012.

[81] LHCb collaboration, *LHCb Tracker Upgrade Technical Design Report*, CERN-LHCC-2014-001, 2014.

[82] J. Van Tilburg, *SciFi readout numbering scheme*, LHCb-INT-2016-044, CERN, Geneva, 2016.

[83] R. Lindner, *Definition of the coordinate system*, LHCB-C-EN-0001, CERN, Geneva, 2003.

[84] S. Esen *et al.*, *Clustering and rawbank decoding for the SciFi detector*, LHCb-INT-2018-024, CERN, Geneva, 2018.

[85] J. Muller, *The LHCb SciFi Tracker: studies on scintillating fibres and development of quality assurance procedures for the SciFi serial production*, PhD thesis, TU Dortmund, 2018, Presented 02 May 2018.

[86] W. M. Zabołotny *et al.*, *GBTX emulator for development and special versions of GBT-based readout chains*, Journal of Instrumentation **16** (2021) C12022.

[87] P. Moreira *et al.*, *The GBT Project*, Proceedings of the Topical Workshop on Electronics for Particle Physics (2009) P342.

[88] D. A. Berninghoff, *Commissioning of the Front-End Electronics of the LHCb Scintillating Fibre Tracker*, PhD thesis, Ruperto Carola University of Heidelberg, 2022, Presented 25 May 2022.

[89] W. E. W. Vink *et al.*, *LHCb scintillating fiber detector front end electronics design and quality assurance*, Journal of Instrumentation **12** (2017) C03053.

[90] J. P. Cachemiche *et al.*, *The PCIe-based readout system for the LHCb experiment*, Journal of Instrumentation **11** (2016) P02013.

[91] G. Vouters *et al.*, *Front-End and Back-End Data Format of the LHCb Upgrade*, LHCb-INT-2014-011, CERN, Geneva, 2014.

[92] L. Del Buono, O. Le Dortz, A. Pellegrino, and W. Vink, *SciFi Tracker TELL40 Data Processing*, 1904563 v5.8, CERN, Geneva, 2022.

[93] H. Verkooijen and W. Vink, *Master Board, technical manual*, EDMS:2154019, Nikhef, Amsterdam, 2022.

[94] LHCb collaboration, *Fibre Database*, `https://lbfiberdb.cern.ch/fiberdb`, 2022.

[95] L. M. Greeven and E. Gabriel, *lhcb-scifi-timingscans*, `https://gitlab.cern.ch/lhcb-scifi/lhcb-scifi-timingscans`, 2022.

[96] The LHCb Scintillating Fibre Tracker Collaboration, *LHCb Scintillating Fibre Tracker: Preliminary Report for the CERN-SPS July 2018 test beam* , CERN, Geneva, 2022.

[97] F. Alessio *et al.* , *LHCb Run3 Raw-data format and ODIN Bank*, EDMS 2100937.v1, CERN, Geneva, 2019.

[98] LHCb collaboration, *FTReadoutMap*, `https://gitlab.cern.ch/lhcb-conddb/SIMCOND/-/blob/upgrade/master/Conditions/FT/ReadoutConf/ReadoutMap.xml`, 2022.

[99] LHCb collaboration, *Coarse Time Alignment of the SciFi - Run253101 - LHCb Commissioning* , LHCB-FIGURE-2022-017 (2022).

[100] LHCb collaboration, *Mass plots with early Run 3 data*, LHCb-FIGURE-2022-034 (2022).

Summary

Imagine a tiny particle flying in a circle with almost the speed of light. Now imagine this with billions of particles. And, suddenly, these particles see another group of particles approaching at them at almost the speed of light from the opposite direction. A head-on collision occurs, and the particles are smashed into each other, producing many different particles. Luckily, we don't have to imagine this, as this is what happens in the Large Hadron Collider (LHC) at CERN. But why would we want to do this? The answer is simple yet complicated: to understand the fundamental building blocks of our universe, and the laws of nature that govern them.

Everything around us consists of atoms, which in turn consist of electrons, protons, and neutrons. Protons and neutrons are made even smaller particles, called quarks. The quarks, together with the leptons (electrons, muons, taus, and neutrino particles) are the fundamental building blocks of our universe. These particles interact with each other through the three fundamental interactions: electromagnetism, the weak force, and the strong force. The interactions are mediated by the force carriers, so-called bosons. Finally, there is the Higgs boson, which is responsible for giving mass to the particles. All of this is described by the Standard Model (SM) of particle physics.

The Standard Model is a very successful theory, and it has been tested to a very high precision. However, it is not a complete theory, as it does not describe gravity, it does not explain why there is more matter than antimatter in the universe, and has no explanation for dark matter. Therefore, physicists are looking for new physics beyond the Standard Model. One way to do this is to study the decays of particles containing a "beauty" quark, so-called b-hadrons. Some decays of these particles are very rare in the Standard Model, and a contribution from possible new physics could have a sizable effect. One possible decay of interest are the $b \to s\ell\ell$ decays, where a beauty quark decays into a "strange" quark and two leptons, either electrons or their heavier version called muons. Another interesting aspect of these decays is the same rate for muons and electrons, which is called lepton flavour

universality (LFU). Experimentally, this can be tested by measuring the ratio of these decays to their electron and muon decay modes.

The measuring of these decays is done at the LHCb experiment at the LHC. The research carried out in this thesis focuses on the decays of the so-called Λ_b^0 baryon, consisting of a b-quark and two "light" quarks. By measuring the decays of the Λ_b^0 baryon, we can test the above-mentioned aspects of the Standard Model. Experimentally, it is beneficial to study the decays relative to other, well-known, decays. For these rare Λ_b^0 decays, a so-called resonant decay is used, where the electrons or muons originate from an intermediate particle. This thesis presents the measurement of the branching fraction of the resonant decay $\Lambda_b^0 \to J/\psi\,\Lambda$. The measured value is in agreement with theory predictions and previous measurements, and the uncertainty is reduced by a factor of three. The result is an important input in the study of the rare Λ_b^0 decays, and other b-particle decays at the LHCb detector.

The rare Λ_b^0 decays are studied to test for lepton flavour universality. To check the used analysis methods, ratios of the resonant Λ_b^0 decays are measured, as these decays are known to be lepton flavour universal. The ratios are expected to be equal to 1 in the Standard Model, however not all of them are in agreement. This indicates that there is potentially an issue in the analysis that needs to be addressed, and this thesis proposes possible solutions. The results are, however, promising and will lead to the first measurement of lepton flavour universality using the rare Λ_b^0 decays.

During the second long shutdown of the LHC, the LHCb detector has been upgraded to handle a higher data rate and collision rate. A large part of the detector was replaced, including the tracking stations. This thesis describes the working of the newly-installed SciFi detector, including the dataflow and data acquisition, the decoding of data, and the timing scans of the electronics. The timing scans are an essential part of the commissioning of the detector, as they are needed for a stable operation of the detector. Four clocks are scanned to find the optimal settings for the full detector, and the results are presented in this thesis. The SciFi detector is currently almost fully operational and data taking with the upgraded LHCb experiment is ongoing. The LHCb experiment is expected to collect a dataset of 50 fb^{-1} by the end of Run 4, which will allow for more accurate measurements of the rare $\Lambda_b^0 \to \Lambda\ell^+\ell^-$ decays.

Samenvatting

Stel je een klein deeltje voor dat met bijna de snelheid van het licht in een cirkel vliegt. Stel je dit nu voor met miljarden deeltjes. En plotseling zien deze deeltjes een andere groep deeltjes op hen afkomen vanuit de tegenovergestelde richting, met ook bijna de lichtsnelheid. Er vindt een frontale botsing plaats, waardoor de deeltjes uit elkaar spatten en verschillende nieuwe deeltjes ontstaan. Maar het hoeft niet bij voorstellen te blijven, want dit is wat er gebeurt in de Large Hadron Collider (LHC) bij CERN. Maar waarom doen we dit? Het antwoord is eenvoudig, maar ook ingewikkeld: om de fundamentele bouwstenen en natuurwetten van ons universum te begrijpen.

Alles om ons heen bestaat uit atomen, die op hun beurt weer bestaan uit elektronen, protonen en neutronen. Protonen en neutronen bestaan uit nog kleinere deeltjes, zogenaamde quarks. De quarks zijn samen met de leptonen (elektronen, muonen, taus en neutrino's) de fundamentele bouwstenen van ons universum. Deze deeltjes staan met elkaar in wisselwerking via de drie fundamentele wisselwerkingen: elektromagnetisme, de zwakke kracht en de sterke kracht. De interacties worden bemiddeld door de krachtdragers, zogenaamde bosonen. Tot slot is er het Higgs-boson, dat verantwoordelijk is voor de massa van de deeltjes. Dit alles wordt beschreven door het Standaard Model (SM) van de deeltjesfysica.

Het Standaard Model is een zeer succesvolle theorie die tot in precisie is getest. Het is echter geen complete theorie, omdat het model de zwaartekracht niet beschrijft, niet verklaart waarom er meer materie dan antimaterie in het heelal is en geen verklaring heeft voor donkere materie. Daarom zijn natuurkundigen op zoek naar nieuwe fysica die verder gaat dan het Standaard Model. Eén manier om dit te doen is door het verval te bestuderen van deeltjes die een "beauty" quark bevatten, zogenaamde b-hadronen. Sommige vervallen van deze deeltjes zijn erg zeldzaam in het Standaard Model en een bijdrage van mogelijke nieuwe fysica zou daarom een aanzienlijk effect kunnen hebben op deze vervallen. Mogelijk interessante vervallen zijn de $b \to s\ell\ell$-vervallen, waarbij een b-hadron vervalt in een

s-hadron en twee geladen leptonen: twee elektronen of twee muonen. Een ander interessant aspect van deze vervallen is dat ze even vaak voorkomen voor muonen en elektronen, wat lepton-smaak universaliteit (LFU) wordt genoemd. Experimenteel kan dit getest worden door de verhouding te meten tussen de vervallen met elektronen en muonen.

Het meten van deze vervallen wordt gedaan bij het LHCb experiment bij de LHC. Het onderzoek in dit proefschrift richt zich op de vervaldata van het zogenaamde Λ_b^0 baryon, dat bestaat uit een b-quark en twee "lichte" quarks. Door het verval van het Λ_b^0 baryon te meten, kunnen we de bovengenoemde aspecten van het Standaard Model testen. Experimenteel is het gunstig om het verval te meten in een ratio van andere, meer bestudeerde, vervallen. Voor deze zeldzame Λ_b^0 baryon vervallen wordt een ander, zogenaamd resonant verval gebruikt, waarbij de elektronen of muonen afkomstig zijn van een "tussendeeltje". Dit proefschrift presenteert de meting van de vertakkingsfractie van het resonante verval $\Lambda_b^0 \to J/\psi\,\Lambda$. De gemeten waarden komen overeen met theoretische voorspellingen en eerdere metingen, en de onzekerheid is met een factor drie gereduceerd. Het resultaat is een belangrijke bijdrage aan de studie van de zeldzame Λ_b^0 vervallen, en metingen van andere b-deeltjes bij de LHCb detector.

De zeldzame Λ_b^0-vervallen worden bestudeerd om te testen op lepton-smaak universaliteit. Om de gebruikte analysemethoden te controleren, worden de verhoudingen van de resonante Λ_b^0-vervallen gemeten, omdat van deze vervallen bekend is dat ze lepton-smaak universeel zijn. Er wordt verwacht dat de verhoudingen gelijk zijn aan 1 in het Standaard Model, maar de gemeten waarden komen niet allemaal overeen met 1. Dit geeft aan dat er mogelijk een probleem is in de analyse dat moet worden aangepakt en dit proefschrift geeft mogelijke oplossingen hiervoor. De met deze oplossingen bereikte resultaten zijn veelbelovend en de verwachting is dat deze zullen leiden tot de eerste meting van lepton-smaak universaliteit met behulp van de zeldzame Λ_b^0-vervallen.

Tijdens de tweede lange shutdown van de LHC is de detector geüpgraded om een hogere datasnelheid en botsingsfrequentie aan te kunnen. Een groot deel van de detector werd vervangen, inclusief de spoorvind-detectors. Dit proefschrift beschrijft de werking van de nieuw geïnstalleerde SciFi detector, inclusief de dataflow en data-acquisitie, het decoderen van data en de timing scans van de elektronica. De timingscans zijn een essentieel onderdeel van de inbedrijfstelling van de detector, omdat ze nodig zijn voor een stabiele werking. Er zijn vier klokken gescand om de optimale instellingen voor de volledige detector te vinden en de resultaten hiervan worden in dit proefschrift gepresenteerd. De SciFi detector is momenteel bijna volledig operationeel en

het verzamelen van gegevens met het verbeterde LHCb experiment is aan de gang. De verwachting is dat aan het eind van Run 4 het LHCb experiment een dataset van 50 fb^{-1} zal verzamelen, waardoor nauwkeuriger metingen van de zeldzame $\Lambda_b^0 \to \Lambda \ell^+ \ell^-$ vervallen mogelijk worden.

Scientific summary

The Standard Model is a very successful theory, and it has been tested to a very high precision. However, it is not a complete theory, as it does not describe gravity, it does not explain why there is more matter than antimatter in the universe, and has no explanation for dark matter. Therefore, physicists are looking for new physics beyond the Standard Model. One way to do this is to study the decays of particles containing a beauty quark, so-called b-hadrons. Some decays of these particles are very rare in the Standard Model, and a contribution from possible new physics could have a sizable effect. One possible decay of interest are the $b \to s\ell\ell$ decays, where a b-hadron decays into a s-hadron and two charged leptons. This process can only happen through suppressed loop diagrams in the SM, and is therefore very rare. The SM also predicts that the $b \to s\ell\ell$ decays at exactly the same rate for muons and electrons, which is called lepton flavour universality (LFU). Experimentally, this can be tested by measuring the ratio of the branching fractions of the electron and muon decay modes. The LHCb experiment at the LHC is designed to study these decays, and is the topic of this thesis.

The research carried out in this thesis focuses on the decays of the Λ_b^0 b-hadron into a Λ and two charged leptons. More specifically, the resonant $\Lambda_b^0 \to J/\psi\,\Lambda$ decays and the rare $\Lambda_b^0 \to \Lambda\ell^+\ell^-$ decays are studied. The branching fraction of the $\Lambda_b^0 \to J/\psi\,\Lambda$ decay is measured, as it is an important input in the study of the rare $\Lambda_b^0 \to \Lambda\ell^+\ell^-$ decays and other b-baryon decays at the LHCb detector. The $\Lambda_b^0 \to \Lambda\ell^+\ell^-$ decays are studied to test lepton flavour universality in the $b \to s\ell\ell$ transitions, using the R_Λ ratio of the branching fractions of the $\Lambda_b^0 \to \Lambda\mu^+\mu^-$ and $\Lambda_b^0 \to \Lambda e^+e^-$ decays. The $\Lambda_b^0 \to \Lambda\ell^+\ell^-$ decays are also used to search for new physics in the form of lepton flavour violating (LFV) decays, where the $\Lambda_b^0 \to \Lambda\ell^+\ell^-$ decays are studied for the presence of $\Lambda_b^0 \to \Lambda e^\pm\mu^\mp$ decays.

The $\Lambda_b^0 \to J/\psi\,\Lambda$ decay is measured using data collected by the LHCb experiment in 2016, 2017, and 2018. To measure the branching fraction, the number of $\Lambda_b^0 \to J/\psi\,\Lambda$ decays is compared to the number of $B^0 \to$

$J/\psi(\to \mu^+\mu^-)K^0_S$ decays, which has a well-known branching fraction and is therefore used as a normalisation channel. This requires the use of the production fraction of Λ_b^0 baryons relative to B^0 mesons, $f_{\Lambda_b^0}/f_d$, which has been measured in bins of the transverse momentum of the b-hadrons. Therefore, the branching fraction is measured by fitting the $\Lambda_b^0 \to J/\psi\,\Lambda$ and $B^0 \to J/\psi(\to \mu^+\mu^-)K^0_S$ invariant mass distributions in bins of the b-hadron transverse momentum. The accuracy of the $f_{\Lambda_b^0}/f_d$ measurement is also the leading systematic uncertainty of the analysis. Another important aspect is the correction of the used simulation samples, as some aspects of the decay and detector response are not well modelled. Corrections are applied for the trigger efficiency, tracking efficiency, particle identification selection, and the angular and kinematic distributions of the simulated decays. The $\Lambda_b^0 \to J/\psi\,\Lambda$ branching fraction is preliminary measured to be

$$\mathcal{B}(\Lambda_b^0 \to J/\psi\,\Lambda) = (3.08 \pm 0.26 \pm 0.12) \cdot 10^{-4}, \tag{E.1}$$

with the first uncertainty from available statistics, from the input branching fractions and the $f_{\Lambda_b^0}/f_d$ shape and normalisation, and the second uncertainty coming from other systematic uncertainties. The result is in agreement with theory predictions and the current world average, and the uncertainty is reduced by a factor of three.

The rare $\Lambda_b^0 \to \Lambda\ell^+\ell^-$ decays are studied using all collected data by the LHCb experiment during Run 1 and Run 1 between 2011 and 2018. Machine learning techniques are used to select the signal decays from the large amount of background events. The ratio of the branching fractions of the $\Lambda_b^0 \to \Lambda\mu^+\mu^-$ and $\Lambda_b^0 \to \Lambda e^+e^-$ decays is measured relative to their $\Lambda_b^0 \to J/\psi(\to \mu^+\mu^-)\Lambda$ and $\Lambda_b^0 \to J/\psi(\to e^+e^-)\Lambda$ counterparts, which are known to be lepton flavour universal. Furthermore, the R_Λ analysis will also include the first observation of the $\Lambda_b^0 \to \Lambda e^+e^-$ decays. The resonant $\Lambda_b^0 \to J/\psi\,\Lambda$ and $\Lambda_b^0 \to \psi(2S)\Lambda$ decays are used to crosscheck the analysis and to validate the selection efficiencies. This is done through measuring the ratio of the resonant mode decays, called $r_{J/\psi}$ and $r_{\psi(2S)}$, together with the double ratio of both resonant modes, $R_{\psi(2S)}$. All ratios should be equal to 1 in the SM, therefore a deviation indicates a potential issue in the analysis that needs to be addressed. The $r^{-1}_{J/\psi}$, $r^{-1}_{\psi(2S)}$, and $R^{-1}_{\psi(2S)}$ ratios are shown in Fig. E.10. The single ratios are below the expected value of 1, while the double ratio agrees with 1. The double ratio shows the power of the method, where the systematic uncertainties cancel out. The presented work shows that the analysis is promising and likely leads to the first observation of the $\Lambda_b^0 \to \Lambda e^+e^-$ decay and the first measurement of R_Λ.

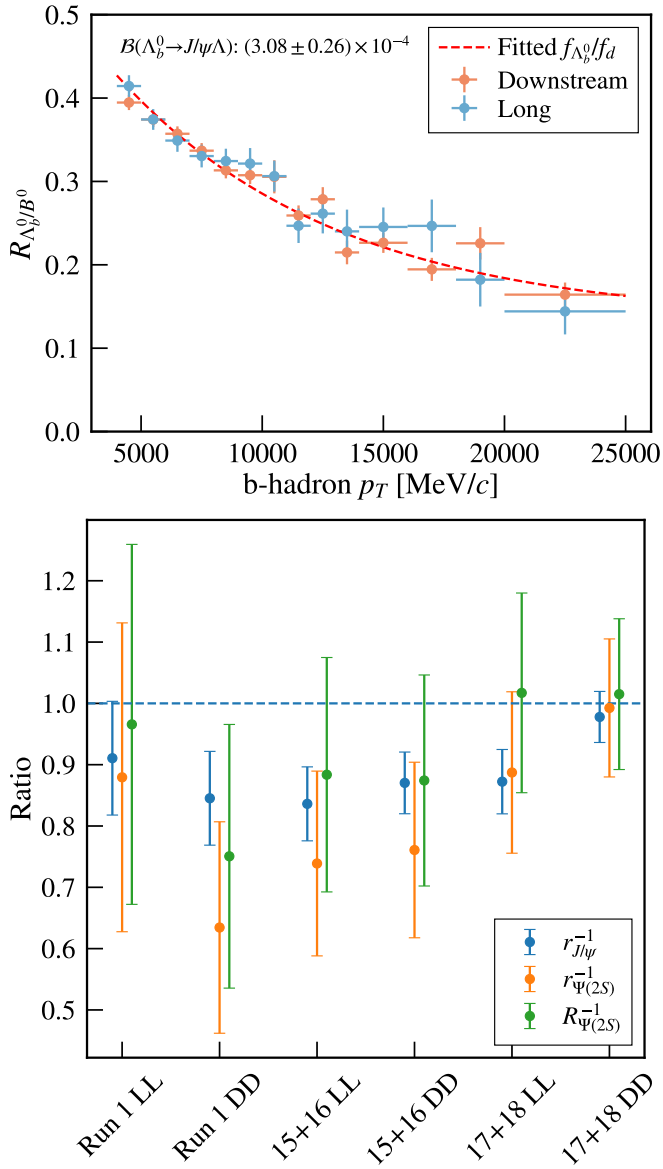

Figure E.10: Top: the measured $\Lambda_b^0 \to J/\psi(\to \mu^+\mu^-)\Lambda$/ $B^0 \to J/\psi(\to \mu^+\mu^-)K_S^0$ efficiency corrected yield ratio in bins of b-hadron p_T for the combined 2016, 2017 and 2018 dataset using downstream (red) and long (blue) reconstructed K_S^0 and Λ candidates. Bottom: the inverse $r_{J/\psi}$, $r_{\psi(2S)}$ and $R_{\psi(2S)}$ ratios for the different data categories. The single ratios are below the expected value, while the double ratio agrees with 1.

During the second long shutdown of the LHC, the LHCb detector has been upgraded to handle a higher luminosity and data rate. The upgrade replaced the previous IT and OT tracking detectors with the new scintillating fibre (SciFi) tracker. This thesis describes the working of the SciFi detector, the dataflow and data acquisition, the decoding of cluster data, and the timing scans of the electronics. The timing scans are an essential part of the commissioning of the detector, as they are needed for a stable operation of the detector. Two clocks are scanned for the clustering FPGA boards, as well as two clocks for the PACIFIC analog to digital converter boards. An optimal clock setting is obtained per link, and a common setting is found for the full detector. Two example scan results are shown in Fig. E.11, and the obtained best clock delay settings are shown in Tab. E.5.

Table E.5: Best values for the FPGA main clock, FPGA IO clock, PACIFIC main clock, and PACIFIC clock for the full SciFi detector.

Clock	**Best value (DAC)**
FPGA main clock	61 ± 2
FPGA IO clock	135 ± 4
PACIFIC main clock	87 ± 5
PACIFIC SyncPulse	367 ± 6

The SciFi detector is currently almost fully commissioned and data taking with the upgraded LHCb experiment is ongoing. The LHCb experiment is expected to collect a dataset of 50 fb^{-1} by the end of Run 4, which will allow for more accurate measurements of the rare $\Lambda_b^0 \to \Lambda \ell^+ \ell^-$ decays.

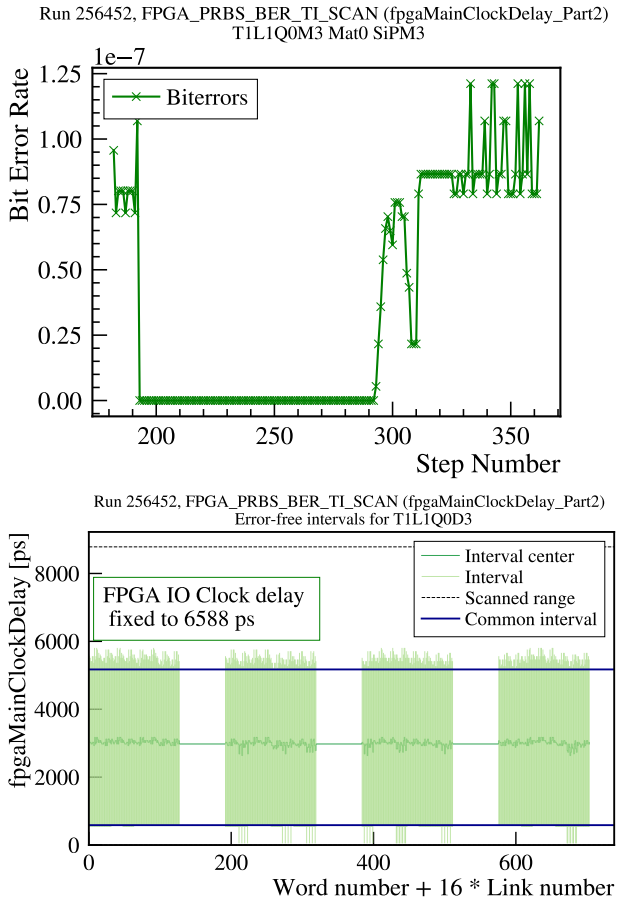

Figure E.11: 1D histogram of the averaged BER over all words for a single link (top) and 2D BER overview plot for a single TELL40 (bottom) for the FPGA Main clock scan. The dark green line shows the error-free interval center, while the light green bars indicate the full error-free region per word. The blue lines indicate the common error-free region for the whole TELL40.

Impact paragraph

In the realm of particle physics, there's an ongoing effort to uncover the mysteries of the universe's fundamental particles and forces. At the heart of this endeavor lies the Large Hadron Collider at CERN, the world's largest particle accelerator. The LHCb experiment, located at the LHC, has made significant progress in understanding rare decays in the subatomic world, specifically focusing on the beauty quark. The work presented in this thesis delves into the investigation of rare decays using the LHCb detector, a task demanding precision, innovation, and perseverance.

But why rare decays? These infrequent processes hold the key to uncovering deviations from the Standard Model of particle physics, our current framework for understanding particle physics. Such deviations could point to new, undiscovered physics that might reshape our knowledge of the fundamental processes in the universe. The analyses presented in this thesis focus on decays of the beauty quark baryons, which have been studied less than their meson counterparts. As the branching fraction of the $\Lambda_b^0 \to J/\psi\, \Lambda$ decay is an input for other analyses, the improved measurement in this thesis allows for more precise measurements of other b-baryon decays. The $\Lambda_b^0 \to \Lambda \ell^+ \ell^-$ decays are used to test lepton flavour universality, a fundamental property of the Standard Model. The work presented in this thesis provides a path towards the measurement of the lepton flavour universality ratio R_Λ, which will all be the first observation of the $\Lambda_b^0 \to \Lambda e^+ e^-$ decay. The LHCb detector has recently been upgraded, including the use of scintillating fibre technology for the new SciFi tracking stations, enhancing its ability to track particles accurately and measure their properties. The upgrade provides an opportunity to study the beauty quark with high precision, and gives an increased sensitivity for measuring rare decays.

From a scientific perspective, the research performed at LHCb is significant. The analyses presented in this thesis contribute to a growing number of tests of the so-called flavour anomalies, potentially hinting at new physics beyond the Standard Model. Beyond CERN, the work has

broader implications. Particle physics research often leads to technological innovations with real-world applications. New detector technologies, such as the SciFi detector, for example, have potential uses in medical imaging and material sciences. An example of this is the use of particle detectors in the development of the Positron Emission Tomography (PET) scanner, a medical imaging device used to detect cancer. Additionally, experiments like LHCb promote international cooperation and knowledge sharing, contributing to global scientific progress.

In conclusion, the work presented in this thesis focused on rare decays at the LHCb experiment and discussed the SciFi detector upgrade. The work provides an additional piece in the large puzzle of particle physics, contributing to the ongoing effort to understand the fundamental building blocks of the universe. From uncovering the mysteries of matter to driving practical technological advancements, fundamental particle physics research has far-reaching impacts on both the scientific community and society as a whole.

Acknowledgements

After four years, this PhD journey comes to an end, and it would definitely not have been possible without the help and support of many people.

First and foremost I want to thank my supervisor and promoter, Niels and Marcel. **Niels**, we've come a long way since the Skype call "to remember what your face looks like" while I was still doing my master's thesis in Bonn. I'm very grateful for the opportunity you gave me to do my PhD here at Nikhef. Who would have known that the SciFi work you suggested, which started out as a side project, would turn into my favorite part of the PhD! Despite the distance between Amsterdam and Geneva, we made the best out of it, although maybe not always enough for you to distinguish the CP-violation between Jordy and myself. **Marcel**, I still remember the first time I met you, giving a colloquium in Maastricht. It must have been a good talk, because after that I ended up doing my bachelor thesis in the Nikhef LHCb group. Even though I didn't do my master thesis in Amsterdam, I'm glad I could come back for my PhD. It has been a pleasure, thank you for always bringing positive energy to the group, having me as a tutor in your courses, and always making time for people when its needed. There aren't as many people that are so genuine and caring about their students as you are.

Next, I would like to thank my two, no three(!) paranymphs, Mick, Silvia, and Aleksandra. **Mick**, as my daily supervisor you were an essential part of my PhD. Your infinite analysis wisdom and patience to explain everything to me helped me along these four years, and this thesis would not have been possible without you. Also outside of work, I really enjoyed our lunches and watching F1 with you and Nayelli. Until the next season! **Silvia**, where do I even begin? I still remember my first day as a PhD, at the BND in Spa, where you were one of the first people I met. You welcomed me into the group from the start, and became one of my closest friends. Thank you for always being there for me during the highs and lows, for the many lunches and dinners, coffees, walks in the park during Covid times, for the many hours of talking about work, relationships, and life, and for always

being so positive and supportive. As you have shown to me, I know I can always count on you to have my back, and I hope you know I will always have yours. **Aleksandra**, my hiking buddy, "office bestie" and paranymph on-call. From hiking through Kennermerland, the Jura or the Austrian Alps, or just personal life stories, we have had many adventures together. Thank you for all the support, advice, whatsapp conversations, helping me pick the right outfits, and being there for me when I needed it. I'm glad we could share our PhD and life experiences, now the Swiss Alps are up next?

There are many more people in the Bfys group that I would like to thank. **Jordy**, my always cheerful office mate. I'm glad we could share this PhD journey together, as academic "brothers" under the same supervisor. From the many beers at Polder to Halloween parties with matching costumes, it was always a good time. Since you left for your postdoc, I haven't been called Jordy anymore, let's see if they manage at the defence. **Jacco**, already from my bachelor thesis onwards you have been a close friend. It was great fun tutoring Quantum Theory, and figuring out how to do everything in a lockdown world. Slowly you have turned from a PhD into a wise old senior staff member, and I knew I could always come to you for advice. Thank you for always being there for me. **Kazu**, you came to my rescue when I was a lost baby PhD student in the world of SciFi. Somehow after many terrible jokes, I still really enjoyed our times in the control room, working on all "this nonsense", clicking "engage" many times. **Jan**, my fellow SciFi PhD. Hanging out with you at CERN, commuting together in the Panda, watching Top Gear and bad action movies, it all made my long-stay much more fun. **Igor**, thank you for many interesting discussions about varied topics, from being a PhD student in HEP to politics and everything inbetween. The summerschool in Split was one of the highlights of my PhD, and I'm glad we could share it together. **Brían**, yes you are listed under the Bfys group. I think we slowly turned into Statler and Waldorf while finishing the thesis, but we both managed in the end. We seemed to be the last two Bfys boulderers standing, don't break your wrist again, okay? **Daniel M.** (Doaniel), one of our latest additions to the PhDs. You quickly conquered our hearts, must be all that Swedish charm. Here is to much more bouldering and Cineville movies together! **Mark**, our food and wine connoisseur. Thank you for the many Prévessin dinners, coffee breaks at CERN, and our shared love for memes. **Maarten**, thank you for the many coffee break discussions, the trip to France, and for always being available for physics advice. **Lera**, we started our PhD almost at the same time, and we shared this journey together. Thank you for always being enthusiastic and saying what you think, Bfys wouldn't be the same without you. I would also

like to express my thanks to **Alice** for being my CERN office mate, **Anna**, **Andrea**, **Andrej**, **Andrii**, **Antonio** for his many inputs on my SciFi work, **Carolina**, **Chris** for supporting me since MSP, **Cristina**, **Davide**, **Daniel C.**, **Daniel H.** for being just as big of a gossiper as me, **Efrén** for being the third N352 musketeer, **Emmy** for being my SciFi timing scan buddy, **Evridiki**, **Ganrong**, **Gerhard** for his computing wisdom, **Katya**, **Keri**, **Kristoff**, **Mara**, **Maurice** for helping me bring bouldering to the group, **MD**, **Melika**, **Michele** for being my virtual office mate, **Miriam** for being my Maastricht buddy, **Maxime**, **Olaf**, **Patrick**, **Robbert**, **Roel**, **Roman** for his life-wisdom, **Sander**, **Sevda**, **Suzanne**, **Wilco** for teaching me almost everything I know about SciFi electronics and timing scans, and **Wouter**.

I want to say a special thank you to the students I supervised during my PhD, **Vlad**, **Sietske**, and **Ali**. It was a real pleasure working with you, and I hope you learned as much from me as I did from you. It makes me really happy seeing you all continuing your academic career, inside and outside of LHCb.

Outside of Nikhef, there are also many people to thank. From the $\Lambda_b^0 \to \Lambda \ell^+ \ell^-$ analysis team I would like to thank **Paul**, **Chishuai**, **Niladri**, **Flavio**, **Nigel**, and **Luismi**. It has been a pleasure working with you during the last four years, and I can be confident I'm the leaving the analyses in good hands. From the SciFi group I would like to thank **Louis** for adopting me when I was without supervision. I learned a lot from you and knew I could always count on you for help and advice. I still sometimes have nightmares about decoding v7, but then I remember it was happily merged after 300+ days. **Lukas**, **Preema**, **Elisabeth**, and **Maria**: thank you for our shared time in the control room, one of the lunch places around Point 8, and Totem for bouldering. Working on SciFi and being at CERN was one of the highlights of my PhD, and you all made me feel very welcomed. Also a special thanks to **Svenja**, **Srijan**, and **Georgios** for making my time during my master in Bonn so enjoyable. Many of the skills I used during my PhD, I learned during my master thesis in the Belle II group, for which I have to thank **Stephan**, **Peter**, and **Jochen**.

Luckily there is also a world outside of physics, where there are also many people to thank. First of all, the "lads" **Connor**, **Dhruva**, and **Sam**. Going back as long as we do, we have shared it all. Thank you for all the fun times: the many dinners and bar visits during our bachelor in Maastricht and later in Amsterdam, hiking in Switzerland, and the hours of playing (board)games together. You were always there to listen to my many rants throughout the years, and to lighten the mood with memes. **Annabel** en

Pim, ondanks dat we na MSP nooit meer op dezelfde plek gewoond hebben, spreken we gelukkig nog vaak af! Na bijna 10 jaar is het nog steeds elke keer gezelliger dan de vorige en ik hoop dan ook dat we dit nog lang kunnen blijven doen. Dankjewel voor jullie steun en vriendschap door de jaren heen. I would also like to thank the rest of the Maastricht (et al.) crew for our lasting friendship over the years: **Lizzy**, **Virginie**, **Signý**, **Veerle**, **Mischa**, **Phil**, **Floor**, and **Jesko**. **Matt**, **Amy**, and little **Theo**, thank you for all the great times in Bonn. Though you are far away, you are always close. **Michelle**, even though things didn't work out in the end, this thesis wouldn't have been possible without you. Thank you for all the support throughout the years, and I wish you all the best wherever life takes you. **Valentina**, thank you for becoming a part of the family and for sharing the PhD pain. Soon we can greet eachother with "Dr." every day.

Last maar zeker not least wil ik mijn familie bedanken. **Mama**, **Papa** en **Caspar**, bedankt voor alle hulp en liefde door de jaren heen. Van kleins af aan hebben jullie bij mij de interesse in wetenschap (en misschien ook wel natuurkunde) aangewakkerd. Het is een lange reis van bijna 10 jaar geweest van Maastricht via Bonn naar Amsterdam, dat was allemaal alleen maar mogelijk door jullie steun. Ik houd ontzettend veel van jullie en deze PhD is voor jullie.

About the author

Lex Greeven was born in 1996 in Maastricht, the Netherlands. He completed his secondary school in 2014. From 2014 to 2017, he attended Maastricht University studying at the Maastricht Science Programme, where he obtained a cum laude Bachelor's degree in Liberal Arts and Sciences. Afterwards, from 2017 to 2019 he enrolled at the University of Bonn and obtained his Master's degree in Physics. His master thesis focussed on studying rare b-meson decays at the Belle II experiment in Japan.

In 2019, he started his PhD in experimental particle physics at the LHCb group at Nikhef, associated with Maastricht University. As part of his PhD, he presented his work at multiple national and international particle physics conferences, including LHCP 2023, and won the public vote for best poster at Physics@Veldhoven 2022. He also took tutor roles in several courses at Maastricht University and supervised multiple bachelor and master student projects.